AN ABSTRACT OF THE THESIS OF

Robin Tokmakian for the degree of Master of Science in

Oceanography presented on December 8, 1989 .

Title: Sea Surface Velocity Determination Using Satellite Imagery:

Validation and An Application

Redacted for Privacy

Abstract approved: _____

P. Ted Strub

In this thesis, the method of estimating sea surface velocities from sequences of satellite Advanced Very High Resolution Radiometer (AVHRR) and Coastal Zone Color Scanner (CZCS) images using the objective maximum cross-correlation (MCC) technique is examined. Two main focuses are discussed. The first is to validate the MCC method and the second is to apply the method to the coastal ocean off Cape Blanco, Oregon.

A set of synthetic images is created by advecting an AVHRR - temperature field with a QG model velocity field. The MCC method of determining the sea surface velocities is then applied to the synthetic images. RMS differences between the model's velocity field and the field produced by the MCC method are calculated. In addition, real AVHRR and CZCS images are used to find the RMS difference between the satellite-derived velocity fields and *in situ* ADCP and hydrographic data. The tests show that AVHRR imagery yields the best results

when images are separated by as short a period as possible. RMS errors at 6-hour separation are on the order of 0.14 $m \cdot s^{-1}$, growing to ≥ 0.25 $m \cdot s^{-1}$ at separations of more than 18 hours. CZCS images are always separated by 24 or more, but images with well defined features result in RMS differences less than those produced by AVHRR images separated by 12 and 24 hours and greater correlations to ADCP velocities. Specific examples show some of the reasons for incorrect vectors calculated by the method.

The second focus describes the circulation patterns seen off Cape Blanco, Oregon during 1987 and 1988. The AVHRR image set resulted in two main conclusions. First, the mid-July sequence shows a strong jet that is clearly visible in the images from that time period. This sequence of images is an ideal sequence which has 1) a persistent wind associated with it; 2) strong, visible features; 3) images which are separated by less than 18 hours; and 4) several pairs that allow averaging to be done. The procedure that was conducted to produce the well-defined flow visible in the first complex EOF was to first remove the vectors with a maximum correlation coefficient less than 0.7 and then, if the field still contained vectors inconsistent with the rest of the field, apply the vector consistency check. The second conclusion, is that the spring/summer view of the circulation pattern is of a meandering jet, flowing strongly offshore north of the capes with a weaker, onshore flow south of Cape Blanco.

Sea Surface Velocity Determination Using Satellite Imagery: Validation and An Application

by

Robin Tokmakian

A THESIS

submitted to

Oregon State University

in partial fulfillment of
the requirements for the
degree of

Master of Science

Completed December 8, 1989

Commencement June 1990

APPROVED:

Redacted for Privacy

Assistant Professor of Oceanography in charge of major

Redacted for Privacy

Dean of College of Oceanography

Redacted for Privacy

Dean of Graduate School

Date thesis is presented: December 8, 1989

Acknowledgements

I would first like to acknowledge the help and encouragement provided to me by my major professor, Dr. Ted Strub. I learned a great deal by the guidance he provided to me, allowing me to make mistakes and nudging me in the right direction. Additionally, I would like to thank Dr. Mark Abbott and Dr. Enrique Thomann for the help and data they provided me in their respective fields.

Dr. Corinne James and Dr. Andy Thomas are thanked for the various programs which they provided to me, free of charge. This saved a great deal of time and allowed my research to continue smoothly. Dr. William Emery provided the original program for the MCC method, which I was greatful to have. Dr. Jane Huyer, Dr. Mike Kosro, and Dr. Leonard Walstad provided me with data for this research project.

I would like also to thank all my fellow students for the moral support and encouragement that was sometimes needed.

A NASA grant, NAGW-1251, supported me and my research throughout my stay.

Last, I would like to thank my family, especially my father and mother who have given to me unconditional love and support throughout my life and have always encouraged me to dream.

TABLE OF CONTENTS

List of Figures

List of Tables

Sea Surface Velocity Determination Using Satellite Imagery: Validation and An Application

1. Introduction

Coastal ocean circulation affects a wide range of biological, chemical, and physical processes. A knowledge of coastal circulation and its variability is fundamental to understanding fisheries, coastal water pollution propagation, sediment transport and other problems. The feasibility of conducting large oceanographical ship surveys to study coastal circulation is expensive and difficult to facilitate. Additionally, the time it takes to cover large areas of the ocean results in a non-synoptic data set and aliases temporal changes into the spatial variability. Thus, there is a need to study coastal circulation patterns over large regions in short time periods which can not be covered by ship surveys to produce a temporally coherent picture of the coastal ocean.

Satellite data sets have been increasingly used to examine oceanographic characteristics. In the future, an even greater amount of satellite data will be available. Techniques need to be developed now to efficiently use the enormous amount of satellite data which will become available in the future. Satellites measure many different quantities of the ocean, from the amount of chlorophyll in the top layer of the ocean to internal wave fields. The two types of satellite data used in this thesis reflect the amount of chlorophyll in the ocean surface layer and the temperature of the sea surface. The data form images showing intricate patterns of the two characteristics partially caused by the currents flowing in the ocean surface layer.

A technique, referred to as the maximum cross-correlation (MCC) technique, has been experimentally applied in recent years as a method that is capable of deriving a sea surface velocity field from a sequence of satellite images. Although many papers have been written which state that the method works qualitatively, systematical research has not been conducted to quantify the accuracy of the velocity fields produced by the MCC method. This thesis will attempt to quantify the accuracy of the MCC fields. In addition, the MCC method will be applied to images gathered over two years off Cape Blanco, Oregon, where relatively little is known about the coastal circulation patterns. The goal is to understand the surface circulation patterns over a monthly and annual basis.

The thesis, organized in two major parts, covers the validation of the MCC method and discusses the circulation patterns produced by the MCC method in the Cape Blanco region. The validation of the MCC consists of evaluating the MCC velocity fields to determine when they can be considered representative of the actual surface flow fields. First, the history of the MCC method is reviewed section two, followed by a description of the methods and of the data used in section three. Section four covers the validation of the MCC technique, first using synthetic images and a model velocity field and then using real images and *in situ* data. The fifth section discusses the results and problems encountered in applying the method to a specific area, namely Cape Blanco, Oregon. Section six summarizes the successes and failures of the technique and the possibilities of using the method with future satellite data.

2. Background

Since the late 1970's satellite imagery has been used to observe mesoscale features in the ocean surface waters. Many scientists have used the infrared images from the NOAA series of satellites to observe temperature patterns in the surface ocean and the Coastal Zone Color Scanner (CZCS) images from the Nimbus-7 satellite to observe similar patterns in the visible range of the spectrum, reflecting chlorophyll pigment and sediment. *La Violette* (1984) used CZCS and the Advanced Very High Resolution Radiometer (AVHRR) aboard the NOAA-7 satellite to describe surface patterns in the Alboran Sea. *Arnone and La Violette* (1986) used the CZCS instrument along with the AVHRR instrument on NOAA satellites to make qualitative observations about the African Current. They determined that the ocean color images sometimes define the flow better than do the temperature fields represented in the AVHRR images. *Vastano and Bernstein* (1984) used infrared imagery to observe the eddies in the Oyashio Front of the Kuroshio Current.

The patterns observed in the surface ocean deform relatively slowly in time, allowing a feature, such as a patch of cold water, to be tracked visually from one image to another in a sequence of images. The method which attempts to track features visually is referred to as the subjective method. The method involves determining the displacement of features by having a person visually locate a unique feature in one image and then find its location in the next image of a sequence.

Vastano and Borders (1984) used the subjective method to estimate the surface velocity field of the Oyashio Front from AVHRR satellite data. They compared the results to ship data and concluded that a reasonable velocity field could be determined. In a continuation of the study of the Oyashio Front, *Vastano and Reid* (1985) used the surface velocity field determined by the subjective method as input to a least-squares regression analysis to calculate the coefficients of a streamfunction. From the streamfunction, the mesoscale sea surface topography was computed. They concluded that the flow field described the individual mesoscale features quite well using images separated by 12 hours.

Svejkovsky (1988) used AVHRR and CZCS to subjectively determine the sea surface velocity field off the coast of California in two areas, near Point Arena and Point Conception. He compared his surface velocity vectors with drifter buoy data from the Coastal Dynamics Experiment (CODE) and the Organization of Persistent Upwelling Structures (OPUS) experiments. The dates of the images were coincident with the time of the experiments. He found an RMS difference between the buoy data and the satellite derived surface field of 0.06 $m \cdot s^{-1}$. His measurements tended to underestimate the field in regions of strong currents and along sharp frontal boundaries. The velocity fields derived from CZCS imagery was almost identical to the fields derived from the AVHRR images.

The subjective method of determining a surface velocity field from sequential satellite images is a time consuming process. An objective method, known as the maximum cross-correlation (MCC) method, has been advanced as a way to

automate the process of determining the sea surface velocity field (*Emery et al.*, 1986). The method, described in section three, was originally used in meteorology to track clouds observed in the geosynchronous satellite images from the Applications Technology Satellite (ATS-I). *Leese, et al.* (1971) developed the method using sequential images 24 minutes apart. They concluded that 82 percent of the displacements were correct to within 30°. It was also determined that the calculation of the correlation matrix was computationally faster when it was computed in the frequency domain ($3N \log_2 N$ computations, where N = number of samples) rather than in the spatial domain (N^2 computations). When the coefficients are computed in this way on a Microvax computer, the time for computing a velocity field over a 500 km x 500 km area is long, about 48 hours.

The MCC method has been used successfully to track ice flows. *Fily and Rothrock* (1986,1987) applied the method to synthetic aperture radar (SAR) data collected with the Seasat satellite to track ice movements. They modified the algorithm by first using a large grid to make a coarse estimate of the displacement. The coarse displacement defined a reduced search area for a finer grid definition. Fragmentation of the ice block added to the error of their displacement fields. *Vesecky, et al.* (1987) investigated the effects of rotation of an ice field on the results of the MCC velocity calculation. When an ice field rotated more than 15°, the translational MCC method failed to pick the correct displacement of the ice field from one image to the next. A similar conclusion was reached by *Collins and Emery* (1988).

Emery, et al. (1986) applied the MCC method to AVHRR images off the coast of Vancouver Island, British Columbia from the summer of 1985. The gradient of sequential images, 22 x 22 km in size, were used in the correlation. A qualitative comparison was made between the MCC velocity field and a geostrophic field determined from conductivity, temperature and depth (CTD) data and buoy data. Although the MCC velocity fields are qualitatively similar to the field data, *Emery, et al.* state that the method fails to estimate motion accurately in areas of local upwelling and surface heating. The best results were from images separated by 5 hours rather than from the image pairs separated by 24 hours.

The MCC method has also been applied to images of the English Channel by *Garcia and Robinson* (1989), using CZCS images instead of AVHRR images. Coherent velocity fields, obtained from the images separated by 24 hours, appeared qualitatively correct. No quantitative estimates of the errors were made.

Initial investigations into understanding the contributions to the error in the MCC derived velocity fields have been made by *Wahl and Simpson* (1989). They developed idealized models to test the degradation of the MCC method due to physical processes. The processes investigated included advection, diffusion, and surface heat exchange. Knowledge of the dominant local processes can help in determining the best feature size and the optimal separation in time of the images.

In this thesis, an attempt will be made to quantify the error in the sea surface velocity field estimated by the MCC method. A time series of synthetic images is generated using surface velocities from a high resolution quasi-geostrophic nu-

merical model. The synthetic imagery demonstrates the effects of rotation and distortion by geostrophic currents on features in the imagery. These effects are examined as the time separation between image pairs increases. In a separate comparison, the differences between the velocity fields obtained from ship surveys and the fields produced by applying the MCC method to real CZCS and AVHRR imagery are also examined. Since infrared imagery is an expression of sea surface temperature (SST) in the upper 15 μm of the ocean and the CZCS images, using visible wavelengths, represent the upper 5 to 15 m of the ocean, it might be expected that CZCS imagery will be more successful in determining the sea surface velocity. However, the 24 hour time separation of the CZCS images is a disadvantage. Most investigators feel that this is the upper time limit over which sea surface temperature or color patterns remain coherent enough to trace features from one image to the next. Thus, it is important to determine the relation between the temporal separation of the images used in the MCC calculation and the RMS error expected in the fields. Section four attempts to identify the optimal time separation between images.

3. Methods and Data

This section describes the MCC method and discusses the adjustable parameters associated with the method. Also described are the processing procedures which can be applied to the resulting MCC velocity fields to produce smoother velocity fields.

3.1 MCC Method Description

A feature's movement from one image to a subsequent image is determined by correlating a subimage of the first image to similar subimages in a subsequent image. The smaller subimage from the first in the sequence is cross-correlated with all similar-sized subimages in the larger search area of the second image. The search area is determined by the distance a parcel of water can advect in the time period between the images. The point where the correlation coefficient is a maximum is assumed to be the displacement of the translated feature in the second image. Figure 3.1a shows a typical color pattern from a CZCS image. The gradients and a feature's shape uniquely defines the feature. Figure 3.1b is the pattern in a subsequent image. The eye can identify the displacement of the feature represented by the arrow.

Because of a feature's shape and coloring (the field of temperature or pigment within the feature), components of the velocity in both the normal and the tangential directions (relative to the strong gradient) can be determined to give the total velocity of the subimage. Several simple cartoons help to explain this last statement. Figure 3.2a shows an image containing a straight line at time =

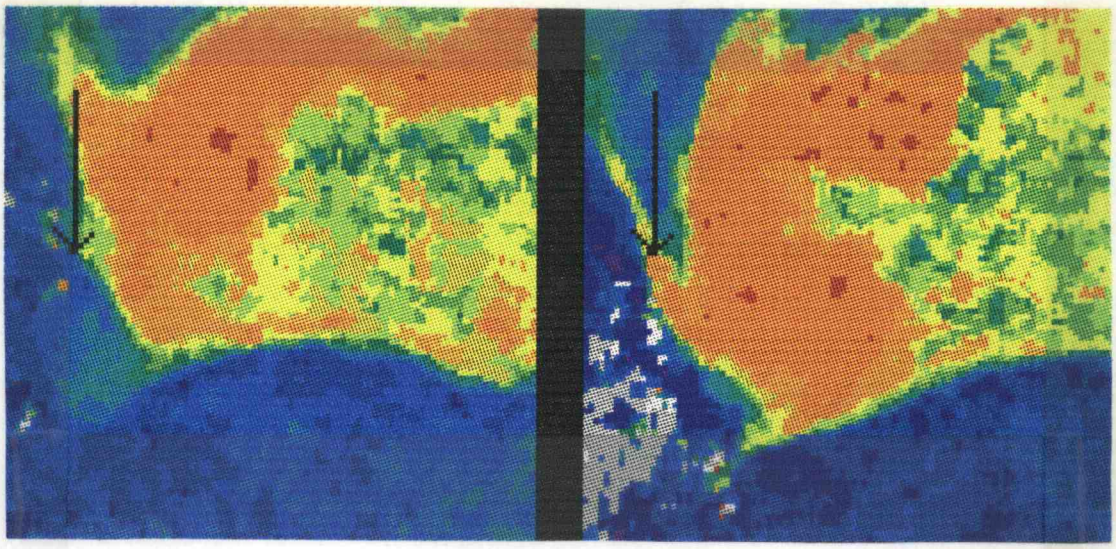

Figure 3.1 Blowup of a CZCS feature. a) July 7, 1981 b) July 8, 1981

t_0. The small interior box represents a subimage. Figure 3.2b shows that the line at time=t_1 has moved to the right. The dotted boxes in the Figure 3.2b show that the initial box may have moved to any of them, since there is no information in the second image to say if the line has moved up or down in addition to moving horizontally. In this case, only the component normal to the gradient can be determined. More information about the movement of the center box is gained if the line contains additional structure as demonstrated by Figures 3.2c and d. The possible final locations are reduced to two places in the second image of the pair shown by the dotted lines. Now, instead of a line, structure (in terms of color) is added to the background. This color represents the horizontal temperature structure in AVHRR images. Enough information has been added

now to the images to uniquely track the feature, identified by the solid box, from Figure 3.2e to 3.2f. In real imagery, if an isotherm (in the case of AVHRR images) is fairly straight and there does not seem to be small scale structure within the subimage, the resulting vectors may seem to follow isotherms, calculating only the normal component to the front and not the tangential component. If this is the case over the whole image, the resulting vector field will be random because the maximum correlation coefficient will be determined by the small scale randomness in the subimage. Thus, the total velocity can only be determined when small scale features are tracked coherently along with the larger feature. The resulting vector field will be fairly smooth. The internal consistency of the final vector field is one test of the method's success and can be used, as described below, to improve the final field when a few vectors are in error.

Cross-correlations can be calculated in the spatial domain or using fast fourier transforms (FFT). If larger subregions are cross-correlated, the use of the FFT increases the efficiency of the calculation. The mathematics for a cross-correlation in space is described by equations 3.1-3.2. The covariance of the subimage is

$$\hat{R}_{12} = < x1 \cdot x2 > - \mu 1 \cdot \mu 2 \tag{3.1}$$

where $< x1 \cdot x2 >= \left[\sum_i \sum_j (x1_{ij} \cdot x2_{ij})\right] / N$. The means are defined as $\mu 1 = \left[\sum_i \sum_j x1_{ij}\right] / N$, and $\mu 2 = \left[\sum_i \sum_j x2_{ij}\right] / N$, $x1$ is a point from the subimage from the first image and $x2$ is a point in the second, search subimage, and N is the number of points contained in the subimage.

Normalizing the covariance by the autocorrelations of the two subimages pro-

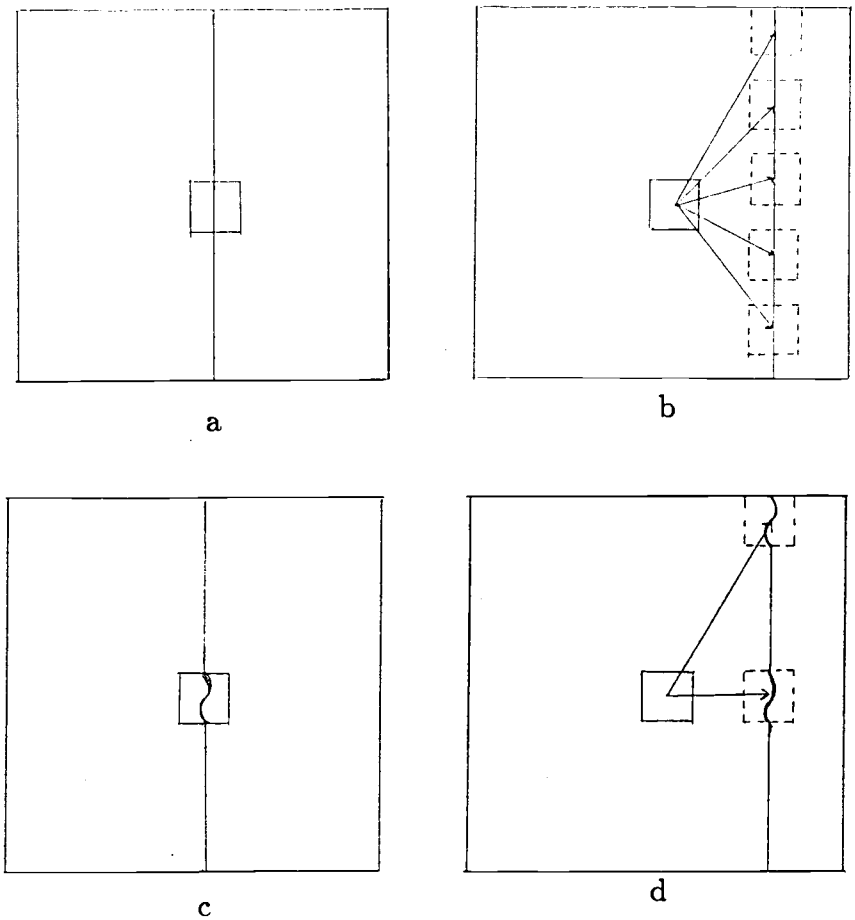

Figure 3.2 Sketches of MCC method a) straight line t=t_0 b) straight line t=t_1 c) curved line t=t_0 d) curved line t=t_1

duces the cross-correlation.

$$\hat{\rho}_{12} = \frac{\hat{R}_{12}}{\hat{R}_{11}^{1/2} \cdot \hat{R}_{22}^{1/2}} \tag{3.2}$$

A cross-correlation value is calculated for every spatial lag of the first subimage against the second, larger search subimage resulting in an array of $(M+1)\times(M+1)$ correlations, where $M/2$ is the number of points lagged on a side.

Equations 3.3-3.5 (*Press, et al.*, 1986) describe the two dimensional cross-correlation using FFTs. A two dimensional FFT is applied to each of the subim-

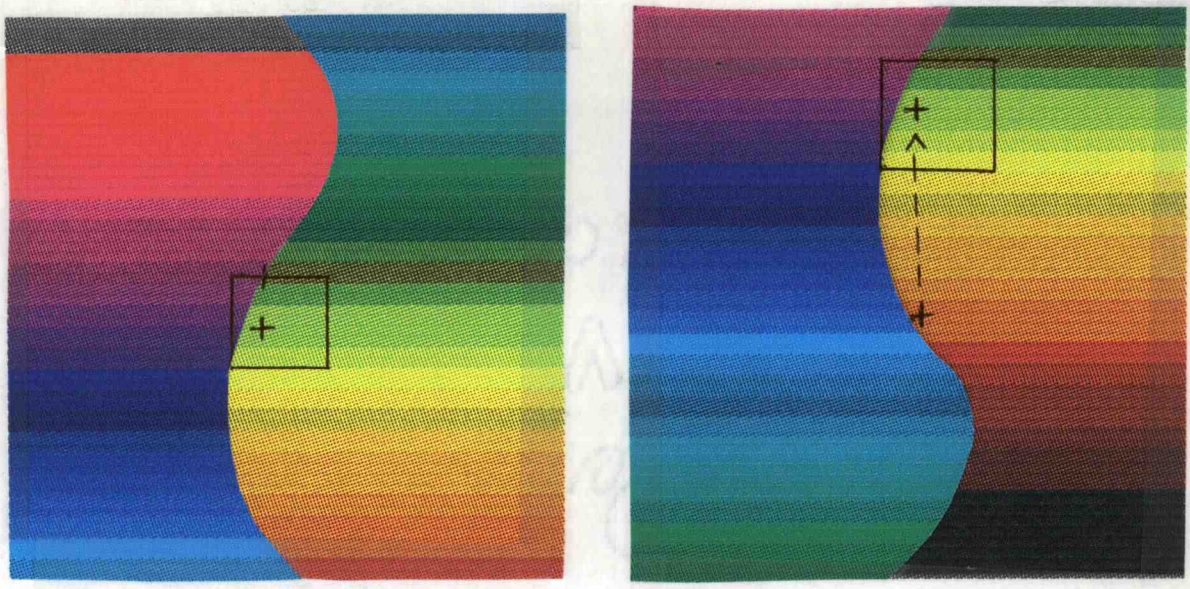

e f

Figure 3.2 (continued) Sketches of MCC method e) curved line with color added t=t_0 f) curved line with color added t=t_1

ages, expressed as:

$$H_x(k_1,k_2) = \sum_{n_2=0}^{N_2-1}\sum_{n_1=0}^{N_1-1} exp\left(\frac{-i2\pi k_2 n_2}{N_2}\right) exp\left(\frac{-i2\pi k_1 n_1}{N_1}\right) h_x(n_1,n_2), \quad (3.3)$$

where H_x is either H_1 for image 1 or H_2 for image 2, k_1 and k_2 are wavenumbers, N_1 and N_2 are the number of points, n_1 and n_2 are the spatial coordinates. The cross-spectral density is computed for the 2 images as

$$\hat{S}_{12}(k_1,k_2) = \frac{1}{N}\left[H_1^*(k_1,k_2)H_2(k_1,k_2)\right], \quad (3.4)$$

where $N = N_1 = N_2$ and H_1^* is the complex conjugate of H_1. An inverse FFT is applied to $\hat{S}$ to produce $\hat{R}(n_1,n_2)$. The two dimensional correlation array $\rho(n_1,n_2)$ is found by normalizing $\hat{R}$ by the product of the zero lag autocorrelation of the

e f

Figure 3.2 (continued) Sketches of MCC method e) curved line with color added t=t_0 f) curved line with color added t=t_1

ages, expressed as:

$$H_x(k_1,k_2) = \sum_{n_2=0}^{N_2-1}\sum_{n_1=0}^{N_1-1} exp\left(\frac{-i2\pi k_2 n_2}{N_2}\right) exp\left(\frac{-i2\pi k_1 n_1}{N_1}\right) h_x(n_1,n_2), \quad (3.3)$$

where H_x is either H_1 for image 1 or H_2 for image 2, k_1 and k_2 are wavenumbers, N_1 and N_2 are the number of points, n_1 and n_2 are the spatial coordinates. The cross-spectral density is computed for the 2 images as

$$\hat{S}_{12}(k_1,k_2) = \frac{1}{N}\left[H_1^*(k_1,k_2)H_2(k_1,k_2)\right], \quad (3.4)$$

where $N = N_1 = N_2$ and H_1^* is the complex conjugate of H_1. An inverse FFT is applied to $\hat{S}$ to produce $\hat{R}(n_1,n_2)$. The two dimensional correlation array $\rho(n_1,n_2)$ is found by normalizing $\hat{R}$ by the product of the zero lag autocorrelation of the

subimages.

$$\hat{\rho}_{12}(n_1, n_2) = \frac{\hat{R}_{12}(n_1, n_2)}{\hat{R}_{11}^{1/2} \hat{R}_{22}^{1/2}}, \tag{3.5}$$

The normalized correlation array is searched to find the maximum positive correlation value. The location of the maximum correlation value corresponds to the displacement of the first subimage in the second subimage. The velocity field is calculated from the displacements and the time separation between the pair of images. The procedure is repeated for specified points over the image pair. It can be done on a regular grid or at specific points for direct comparison to *in situ* data.

The significance of the correlation values associated with each vector can be determined by applying the method to two images which are uncorrelated in time and location. The resulting array of maximum correlation values will contain random correlation values which, when ordered, will give the value of the 95 percentile correlation number. Figure 3.3 shows the distribution of correlation coefficients between two uncorrelated CZCS images. The 95 percentile value is 0.59 for this image pair. The significant correlation coefficient is used to remove insignificant vectors from the vector field produced by the MCC method.

3.2 Determination of Window Sizes

To understand the results of the MCC method in defining a sea surface velocity field, an examination will be made of the parameters that can be adjusted when applying the method to a pair of images reflecting a characteristic, either temperature or pigment color, of the ocean surface. The ramifications of the different

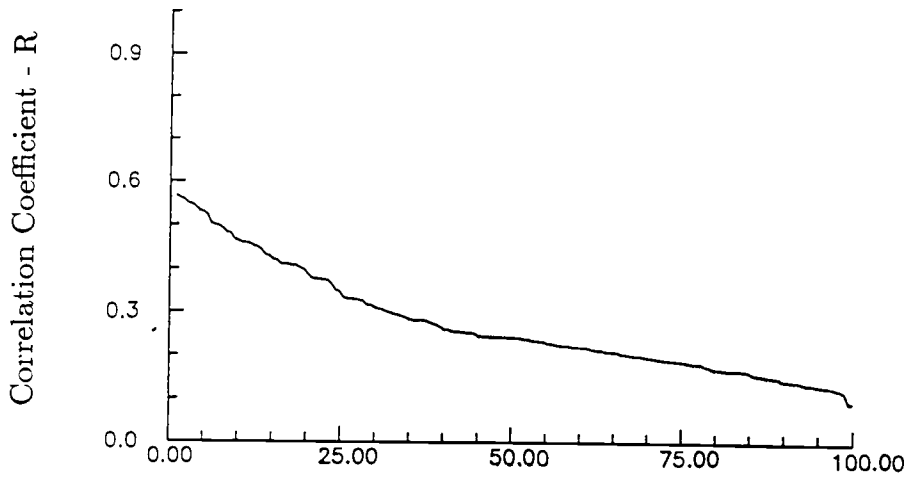

Figure 3.3 Percentage of correlation coefficients found at each correlation value.

subimage sizes will be reviewed.

The size of the subimage causes the MCC method to resolve different fields of displacements. By examining the results of the MCC method when using the same center point but with different subimage sizes, the change in the displacement vectors can easily be seen. Figures 3.4a-d show the contour plots of the two dimensional correlation fields (associated with subimage sizes from 10 x 10 km up to 50 x 50 km) with the initial subimage centered at 125.24° W and 38.63° N in the CZCS image pair of July 7 and 8, 1981 (Figures 4.1a,b). The subimage sizes span the range from approximately 10 x 10 km to 50 x 50 km. A search area extending outwards 50 km is used for all the tests, since it is assumed that the maximum speed of a parcel of water for this region is 0.5 $m \cdot s^{-1}$. The contour plot for a 10 x 10 km subimage (Figure 3.4a) shows that the correlation matrix is fairly random. The random nature of the vectors is explained by not having enough structure (color,gradients) in the small 10 km square area to uniquely

describe the feature; alternately, the coloring is random, so the subimage has similar correlation coefficients with many areas. The 20 x 20 km and 30 x 30 km plots (Figures 3.4b,c) have two or more areas of high correlation, a nearby area where, subjectively, the correct displacement should be, and more distant areas. When the subimage size reaches 50 x 50 km (Figure 3.4d), the area of highest correlation is well defined. Large scale geostropy will include the advection of smaller, ageostrophic features. These small scale changes are the structures which uniquely define the large mesoscale features.

The size of the second subimage, the search window, is strictly defined as the size of the first subimage plus the maximum distance in each direction that a feature could move depending on the time between the images and the maximum expected velocity.

3.3 Vector Field Processing

The MCC method produces a field of displacement vectors. The field will, in most cases, contain incorrect vectors that oppose the field in the immediate area surrounding them (Figure 3.5). Some of the reasons for incorrect and inconsistent displacements were described in section 3.1. Other reasons are further explored in section 4.3.4. Several steps can be applied to eliminate spurious vectors and adjust the field to make it smoother and more coherent.

Any vector that has a correlation value below the level of significance (section 3.1) is removed initially. This removes vectors whose correlation coefficients are not greater than those of random fields. In addition, any vector which has an

Figure 3.4 Contour plots of all correlation coefficients calculated by the MCC method for one subimage. The figures show the effect of varying the subimage size. a) Subimage size of 10 x 10 km b) Subimage size of 20 x 20 c) Subimage size of 30 x 30 d) Subimage size of 50 x 50.

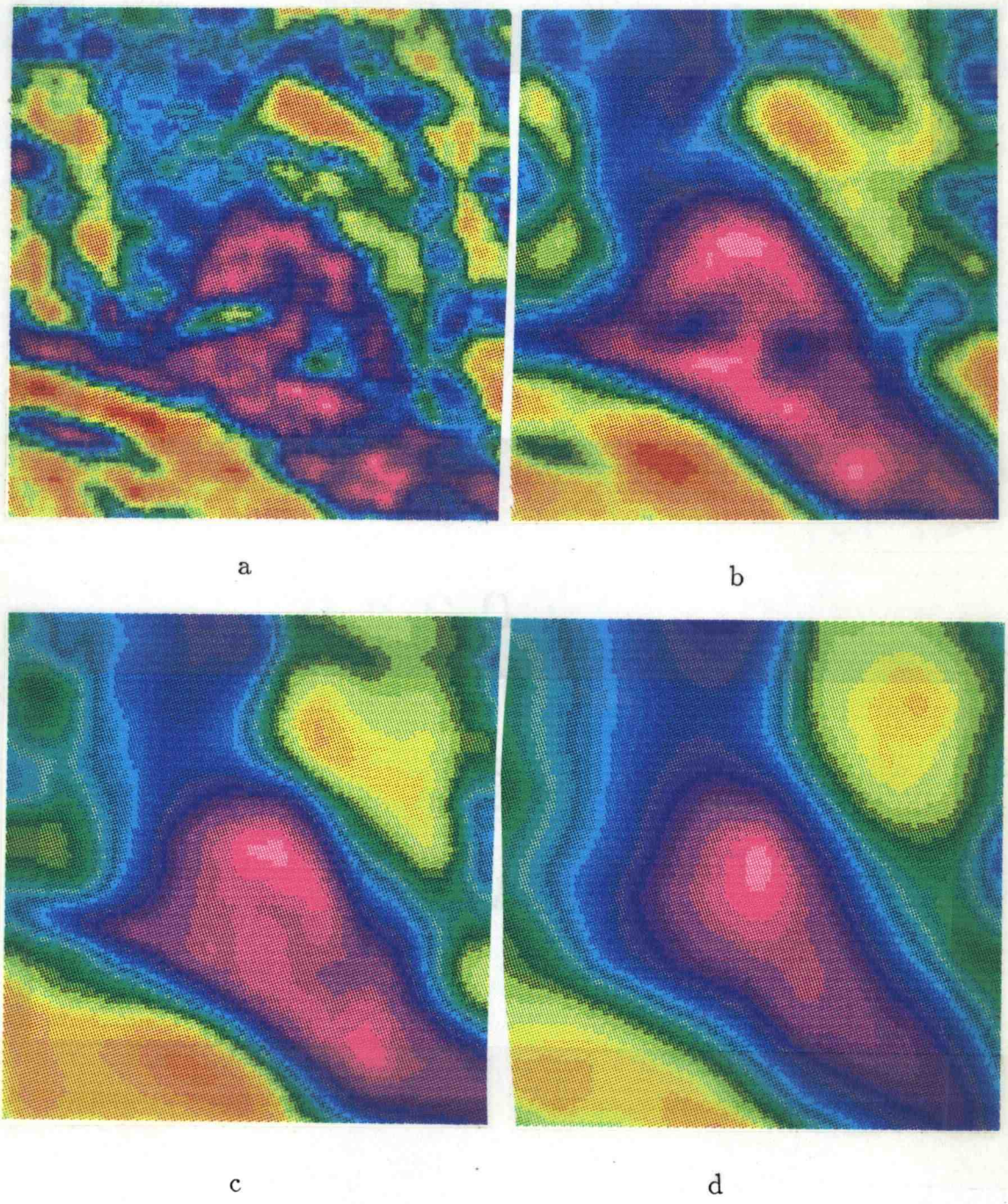

a b

c d

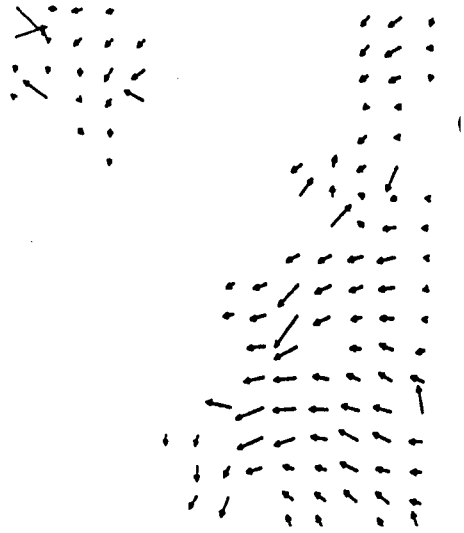

Figure 3.5 Typical Vector field produced by the MCC method

associated velocity greater than the maximum expected velocity of the field in that area is removed. A vector with a velocity greater than the maximum expected velocity can result when the maximum correlation is at an angle other than 0°, 90°, 180°, or 270°. These steps will remove a large portion of the vectors that oppose the general field of displacements.

The next steps smooth the velocity field. One process for smoothing is averaging several fields over a time period in which the circulation is not expected to change significantly. Averaging will reduce the effect of any outliers in the vector fields which are not consistent from day to day. Another way to smooth the field is to apply a vector consistency check (VCC) (*Collins and Emery*, 1988). Each vector is checked to determine if the vector displacement lies within the mean x or y displacement ± 1 standard deviation of its neighbors. If it does not, then another

vector is found which has the maximum correlation in the approximately 20 x 20 km area around the mean displacement of the neighbors. The 20 x 20 km area was chosen after tests involving various size areas located the correct vector in an area of this size.

A final method of resolving coherent vectors is the calculation of complex EOFs. This can only be done if enough image pairs occur in a short period of time, which is seldom the case. When it is possible, it has the advantage, over averaging, of excluding the incoherent outliers from the spatial pattern, rather than including their effects in the average pattern (Appendix D).

3.4 Satellite Data

Two kinds of satellite imagery were used in the attempt to validate the MCC method and to describe the surface circulation pattern off Cape Blanco, the CZCS West Coast Time Series data set from 1979 to 1986 and a set of AVHRR images from July 1981 and covering January 1987 to September 1988. The culling and processing of both data sets are described below.

The atmosphere affects the radiation emitted by the sea surface in many ways through absorption and scattering. The atmosphere itself emits radiation at the same frequency as the sea surface, which is also absorbed and scattered. These processes all depend on wavelength. The equation for the total radiance measured at the satellite L_m^λ is

$$L_m^\lambda = t^\lambda (L_w^\lambda + L_R^\lambda) + L_E^\lambda + L_P^\lambda, \tag{3.6}$$

where $t^\lambda = e^{-\tau(0,H)}$ is the transmittance of the atmosphere and τ is the optical

thickness over the distance from the satellite to the sea surface (H). L_w^λ is the radiance scattered upward from beneath the water and L_R^λ is the reflected fraction of all sources of downward radiation. L_E^λ is the emission of upward radiation integrated over the atmosphere, $\int_0^H K_A(z)L_B^\lambda(T_z)e^{-\tau(z,H)}dz$, where L_B is the black body radiation and K_A is the absorption coefficient of the atmosphere. L_P^λ is the amount of radiance scattered into the path of the satellite sensor equal to $\int_0^H K_S(z)L_S^\lambda(T_z)e^{-\tau(z,H)}dz$, where L_S is the electromagnetic radiation available for scattering and K_S is the scattering coefficient (see figure 3.6).

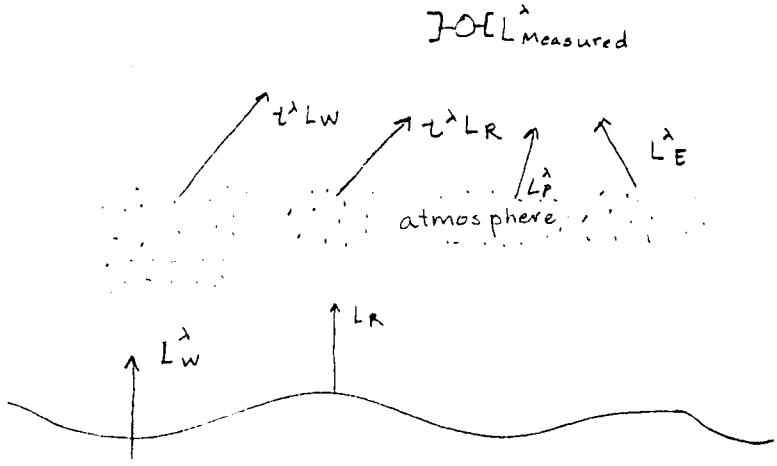

Figure 3.6 Radiation Budget Diagram

3.4.1 The CZCS Data Set

The CZCS, on the Nimbus-7 satellite, measured the light reflected by particles in the sea in the visible frequency band of the spectrum. The CZCS is no longer functional.

For visible wavelengths, the ocean and atmosphere do not emit a significant amount of radiation and the CZCS sensor was oriented to avoid reflected sunlight,

therefore, both L_E^λ and L_R^λ are neglected and the satellite measured the radiance is equation 3.7 at the visible wavelengths.

$$L_m^\lambda = t^\lambda L_w^\lambda + L_P^\lambda, \tag{3.7}$$

L_P^λ is much greater than the water leaving radiance L_w, and must be removed before an image can be used. The atmospheric correction process estimates and removes L_P^λ and τ^λ to arrive at estimates of L_w^λ, the water leaving radiance. Once values of L_w^λ are obtained, in-water algorithms are used to estimate surface pigment concentrations.

The CZCS data used here comes from the set of processed images known as the West Coast Time Series, consisting of 734 usable satellite passes. These have been previously navigated and atmospherically corrected, using a single scattering Rayleigh algorithm (*Gordon et al.*,1983). The data have been converted to surface pigment concentrations using the in-water algorithms of *Clark* (1981). Further details of the processing can be found in *Abbott* (1988) and *Strub, et al.* (1990).

In the first years of the CZCS mission, images were only collected upon request. In addition, the CZCS began to fail in 1984, making the set of images sporadic in time (*Abbott*, 1988, *Strub, et al.*, 1990). The CZCS West Coast Time Series consists of image passes that have been subdivided into smaller sections referred to as "tiles", defined in Figure 3.7. The two tiles that include the Cape Blanco coastal ocean region are tiles J and K. The tiles were combined and a new image was extracted (Figure 3.8). The top left hand corner coordinates are 128.93° W, 45.06° N and the bottom right corner coordinates are 123.81° W, 39.94° N.

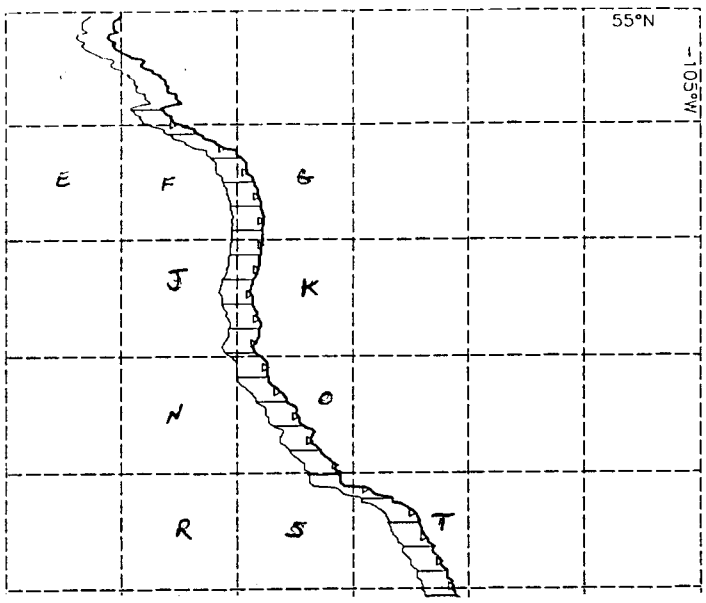

Figure 3.7 Tile definition of the CZCS West Coast Time Series

The resolution of the image is approximately 1.1 km.

3.4.2 The AVHRR Data Set

The AVHRR instrument measures radiation in the infrared frequency band. For infrared wavelengths (3.7 and 11 μm), equation (3.6) can be simplified. L_R^λ is approximately zero because the reflectance ρ is about 0.02 for infrared wavelengths. Also at infrared wavelengths, L_P^λ can be eliminated because scattering is negligible. The equation for infrared radiation is reduced to

$$L_m^\lambda = t^\lambda L_w^\lambda + L_E^\lambda. \tag{3.8}$$

L_m^λ is measured by the satellite. L_E^λ is the contribution from the radiation emitted by the atmosphere. A portion of the water leaving radiance L_w^λ is absorbed by the atmosphere and thus only $t^\lambda L_w^\lambda$ reaches the satellite. The temperature of the sea

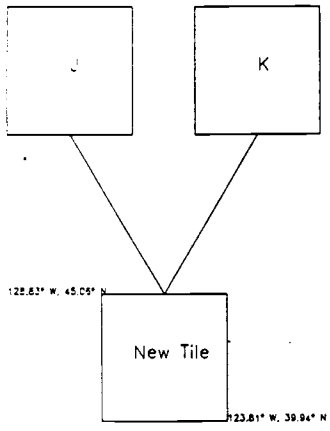

Figure 3.8 Cape Blanco image description, as defined by the CZCS West Coast Time Series tiles.

surface can be computed by using data from two or more channels. Radiation at 10.5μm is more sensitive to water vapor than is radiation at 3.7 μm, the difference in the temperature at the two wavelengths is used as a correction, known as the Multi-Channel Sea Surface Temperature (MCSST) algorithm (*McClain, E. P.*, 1981). For the purposes of this thesis, absolute temperatures were not computed, since the MCC method is only tracking temperature patterns and the correlation computation removes the mean. Thus, the radiance temperature is used with no atmospheric correction.

The two operating NOAA satellites are capable of sampling twice a day. It was hoped that many more cloud free images from the 1987, 1988 data set would produce a larger and more complete set of images. Again, as with the CZCS satellite, satellite passes were not always collected because no request had been made for that pass. Typically, one pass per day was collected.

The set used for the Cape Blanco experiment was reduced to those images that have another image available within a 24 hour time period. This set, centered at 126.0° W, 42.5° N, was extracted from tape. Both channels two ($\approx .9\mu$m) and four (11.5 μm) were retrieved for further examination. Channel three (3.7 μm) was not used because of the large amount of instrument noise it contained. Both channels two and four were examined on the Global Imaging System, a commercially available image processing system running on an Hewlett Packard-9000 computer, to identify those images which contained too many clouds. After extremely cloudy images had been removed from the set, the set was calibrated and converted to temperature fields and navigated using ground points for navigation aids.

The calibration of the satellite data is accomplished by using the calibration data interwoven within the image data. As described above, the data received from the satellite is in counts and has to be converted to temperature values. Calibration information includes the temperature, in degrees, of four platinum resistance thermometers on the satellite itself. The data record contains a gain

and intercept value to use with equation 3.9, to convert counts to radiance.

$$E(\text{ radiance in milliwatts/m}^2 - \text{steradian} - \text{cm}^{-1}) = SC + I, \qquad (3.9)$$

where I is the intercept value, S is the gain and C is the number of counts measured by the satellite. Inverting Planck's equation

$$L^{\lambda} = \frac{2hc^2}{\lambda^5}\left(\frac{1}{exp[hc/kT\lambda] - 1}\right), \qquad (3.10)$$

where h = Planck's constant, k= Boltzman's Constant, and c = speed of light, converts a radiance value to temperature value (*Kiddwell*, 1986).

$$T(E) = \frac{K_1\nu}{ln(1 + \frac{K_2\nu}{E})}, \qquad (3.11)$$

where T is in degrees Kelvin, ν is the central wavenumber of channel filter in cm^{-1} (for channel four, $\nu = 929$), and $K_1 = 1.1910659 \times 10^{-5}$ (milliwatts/m^2-steradian-cm^{-4}) and $K_2 = 1.438833$ (cm - °K) are constants. The cloud identification algorithm (see section 4.3.1), using only channel four, was then applied to flag the areas of the images that contained clouds. As described above, no further atmospheric correction was applied to the channel four radiance temperature.

4. MCC Method Validation

The validation of the MCC method was performed in three steps. First, initial qualitative tests were performed, to understand the basics of the method and to determine if features can be tracked from one image to another producing velocities of the sea surface which seem to be qualitatively correct. The next step quantified the error in the MCC velocity field assuming that the true velocity was known. This was done using a quasi-geostrophic (QG) model's velocity field and synthetic imagery. The last step compared *in situ* data with MCC velocity fields derived from satellite images of the area at the same time. Each step built upon the previous step's results to create an understanding of the conditions under which the MCC method succeeded and failed.

4.1 Data Description

Two sets of satellite images were used in the first and last steps described above. The sets consisted of two sequential, clear CZCS (Figure 4.1a,b) and four sequential, clear AVHRR images (Figure 4.2a,b) which have dates coincident with the Coastal Ocean Dynamics Experiment described below. The navigated and atmospherically corrected imagery (provided by *M. Abbott*) is dated July 7 and 8 of 1981. The CZCS instrument, located on the sun-synchronous Nimbus-7 satellite, provided one image per day at 1900 GMT. A 3 x 3 median filter has been applied to the CZCS images.The AVHRR instruments on the NOAA series of satellites, can provide imagery separated by as short a time period as four hours when two satellites are operating. The four AVHRR images dated July 7 and 8 came from a

single satellite and can be used for comparison at both 12 and 24 hour separation times. The times of the AVHRR images are 0300 GMT and 1500 GMT. The resolution of both sensors is approximately one kilometer. Section 3.4 described the processing of the satellite imagery.

The Coastal Ocean Dynamics Experiment (CODE) was located off Northern California between approximately 37° and 39° N, extending offshore to about 125.5° W, Figure 4.3. The field data used to evaluate the surface velocity field found by the MCC method is from the seventh leg of CODE-1, July 4th through 10th of 1981 (*Olivera, et al.*, 1982). Two data sets are used for the comparison, the hydrographic data set (provided by *A. Huyer*), from which the dynamic heights (relative to 500 decibars) and geostrophic velocities have been computed, and the acoustic doppler current profiler (ADCP) data set (provided by *M. Kosro*).

4.2 Initial Qualitative Tests

The validation of the MCC method began with some simple tests applied to the two sets of images described above, the CZCS image pair and an AVHRR image pair. Features can be tracked in a pair of images visually by manually identifying features in one image and subsequently identifying the same feature in a following image. The MCC method is first tested by using the same points chosen for the subjective method as the center points of the MCC subimages. The resulting MCC velocity field is then compared to the subjective velocity field. Other tests use points located on fronts and in a grid pattern. The last initial test applied the MCC method to image pairs which were gradients of the original

a

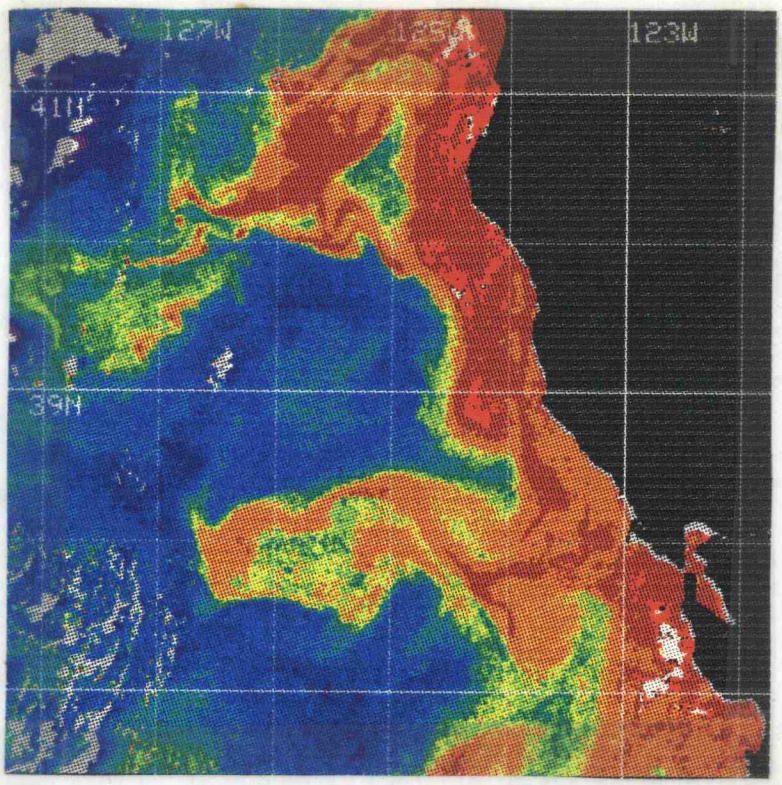

b

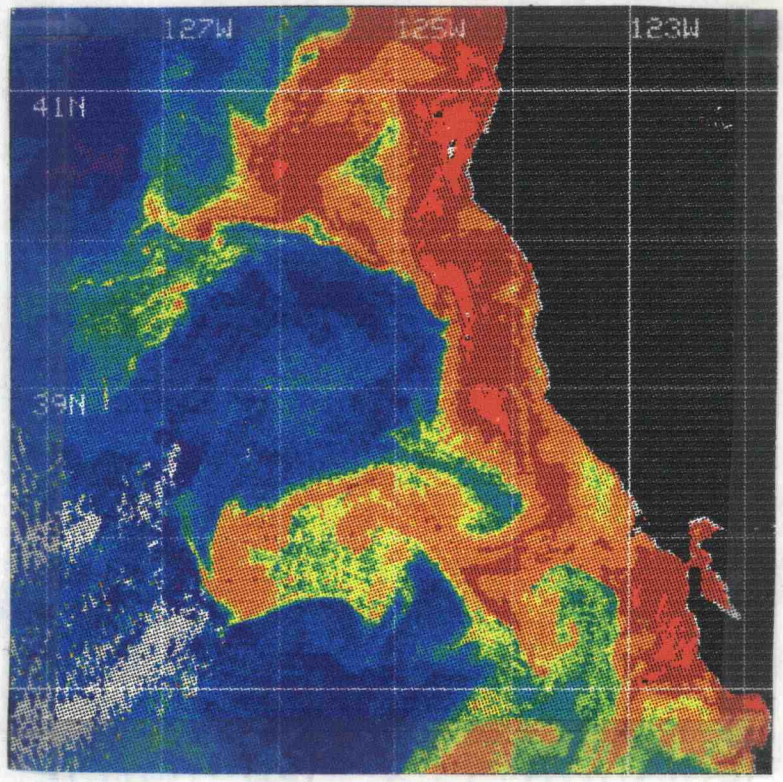

Figure 4.1 a) CZCS field from July 7, 1981 b) CZCS field from July 8, 1981

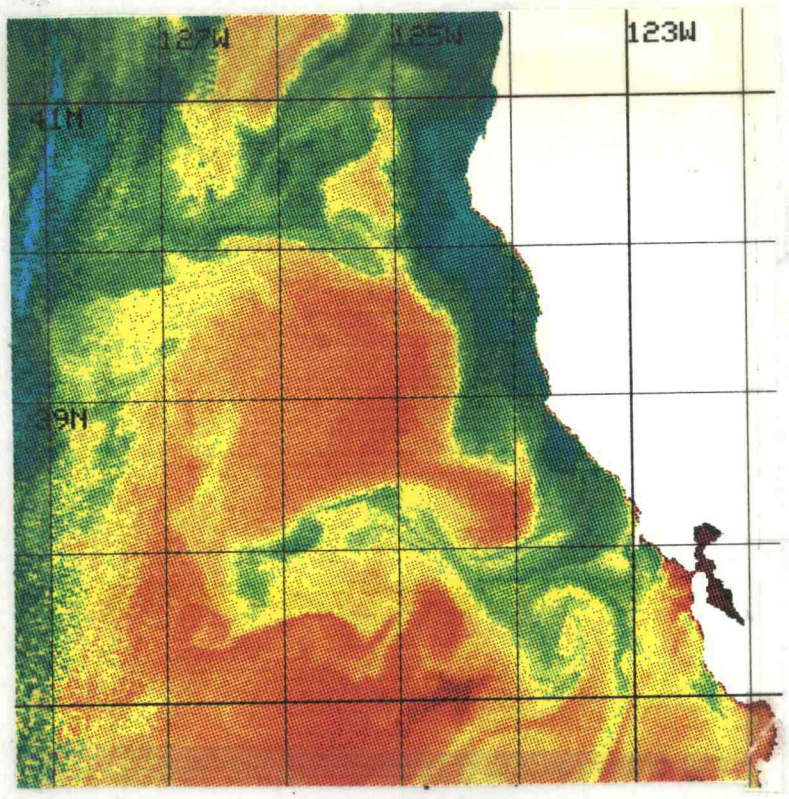

a

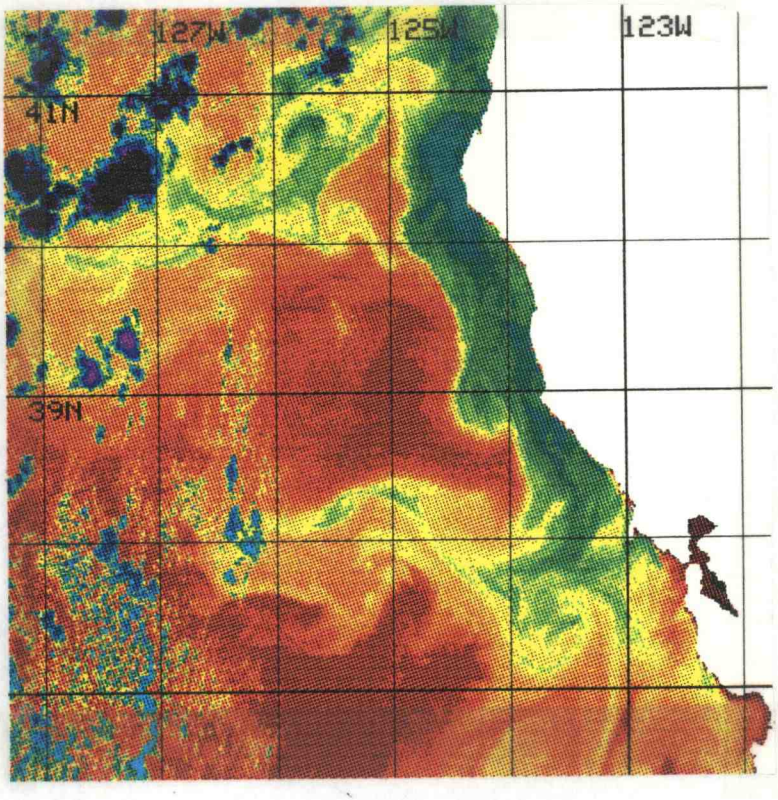

b

Figure 4.2 a) AVHRR field from July 7, 1981 b) AVHRR field from July 8, 1981

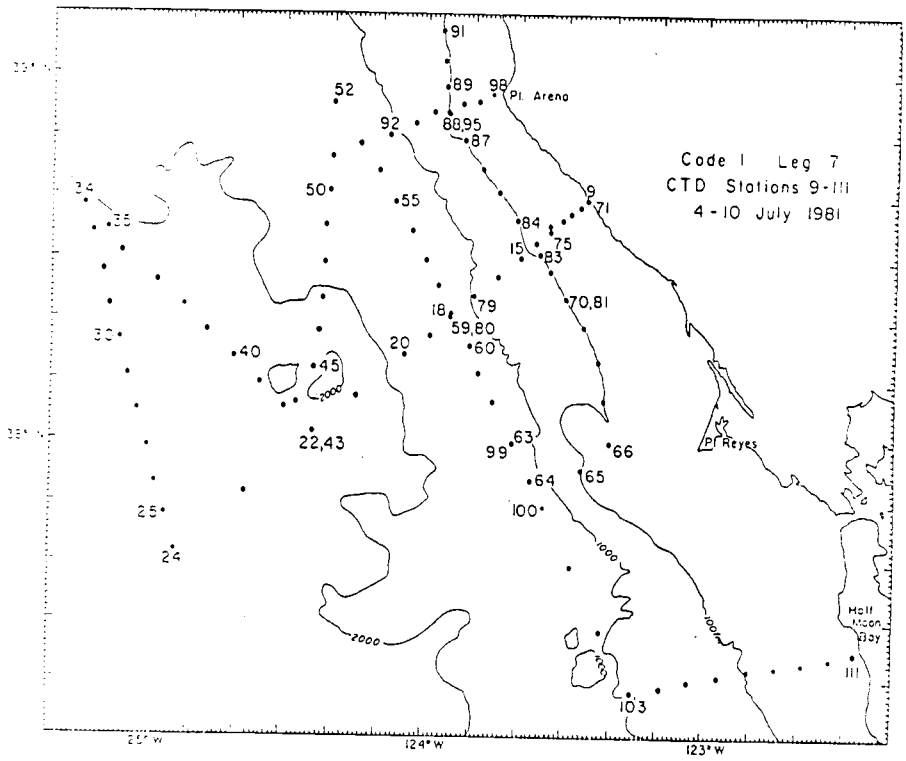

Figure 4.3 Locations of stations CODE July 4-10, 1981 (*Olivera, et al.*, 1982)

images.

The objective MCC method can be successful only if the images exhibit structures and patterns which can be tracked subjectively with the eye. The first image was examined in the CZCS image pair (Figure 4.1a) and points were identified which were located on features unique in the image. Most of the points chosen are on the edges of sharp gradients. Next, an attempt was made to identify that same point (or feature) in the second image of the sequence. The displacement of the feature divided by the time separation between the two images determines

the velocity of the sea surface in that region. The jet in the top of Figure 4.1a has features which are easier to track subjectively than the feature near the bottom of the image. Figure 4.4 shows the resulting velocity field derived from identifying feature movement subjectively. Qualitatively, the image pairs reflect the sea surface velocity flow of the ocean. *Svejkovsky* (1988) used this image pair to derive a subjective velocity field which agreed to within 0.06 $m \cdot s^{-1}$ of a drifter velocity field.

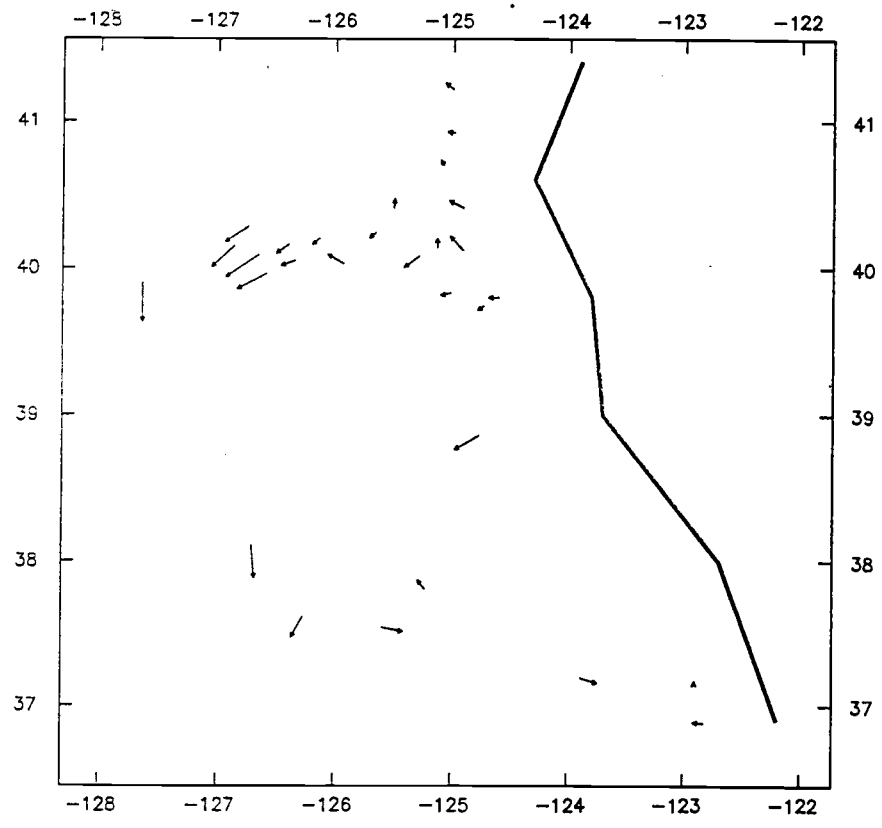

Figure 4.4 Subject velocity field derived from CZCS image pair

The first test of the MCC method used the points from the subjective tests as the center points for the subimage definition for input. Fifty percent of the vectors

in the resulting MCC velocity field are similar to the vectors in the subjective velocity field.

As the next step, points located on fronts were selected. Points on fronts were chosen because horizontal structure is needed for the cross-correlation and it is assumed that at locations where a front (strong gradient) exists, physical processes, such as horizontal diffusion and vertical mixing which are active in the region, will take a longer time to affect the surface structure observed in the imagery. The resulting MCC velocity field is shown in Figure 4.5. It compares well with the field from the subjective method.

To fully automate the process and remove the need for an analyst to identify initial points, points are defined on a grid without reference to where strong gradients may lie. The MCC velocity field with the grid spacing 20 km and 25 km apart are shown, respectively, in Figures 4.6 a and b. Qualitatively, the fields are similar, again, to the subjective velocity field. Velocities with maximum correlations less than 0.6 are not shown.

Ice studies (*Collins*, 1988, *Fily and Rothrock*, 1986) have shown that gradients applied to images allow the edges of ice to be enhanced. This, in turn, makes it easier and more efficient to track ice flows. Ice does not deform rapidly in 24 hours, and tracking the edges gives an MCC velocity field similar to the MCC velocity field derived from the raw image. *Emery, et al.* (1986), applied the MCC method to gradient AVHRR images separated by 4 to 24 hours. The best results were for image pairs separated by four to five hours. The real images for this thesis are

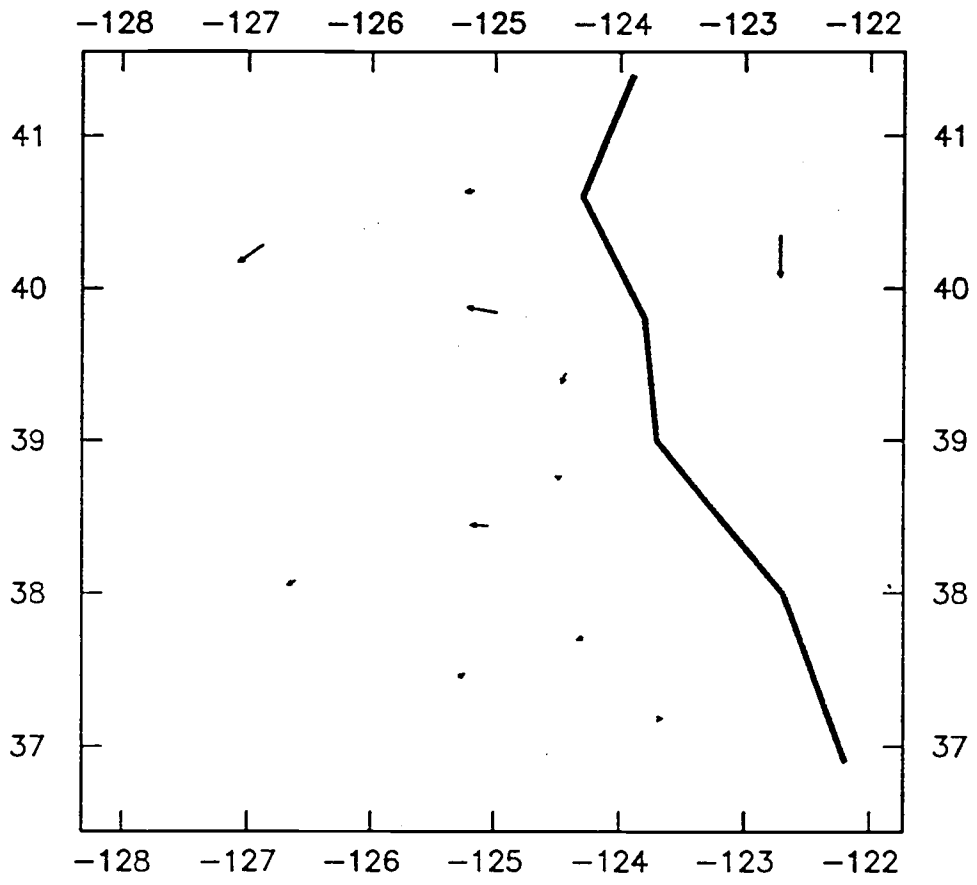

Figure 4.5 MCC velocity field using points located on fronts derived from CZCS image pair.

separated by 12 and 24 hours over which larger deformations are expected. The gradient operator used is a 5 x 5 unweighted central difference scheme such that the value of T' at x,y is determined by equation 4.1.

$$T' = \frac{1}{2d}\left[(T(x-d,y) - T(x+d,y))^2 + (T(x,y-d) - T(x,y+d))^2\right]^{1/2} \quad (4.1)$$

The distance between the center point to the edge is d. In this case, $d = 2$ pixels (2.2 km). The tests of the MCC method applied to the gradients of the CZCS did not produce velocity fields that were coherent. In addition, the correlation coefficients associated with each vector were low (approximately 0.4) and the vector

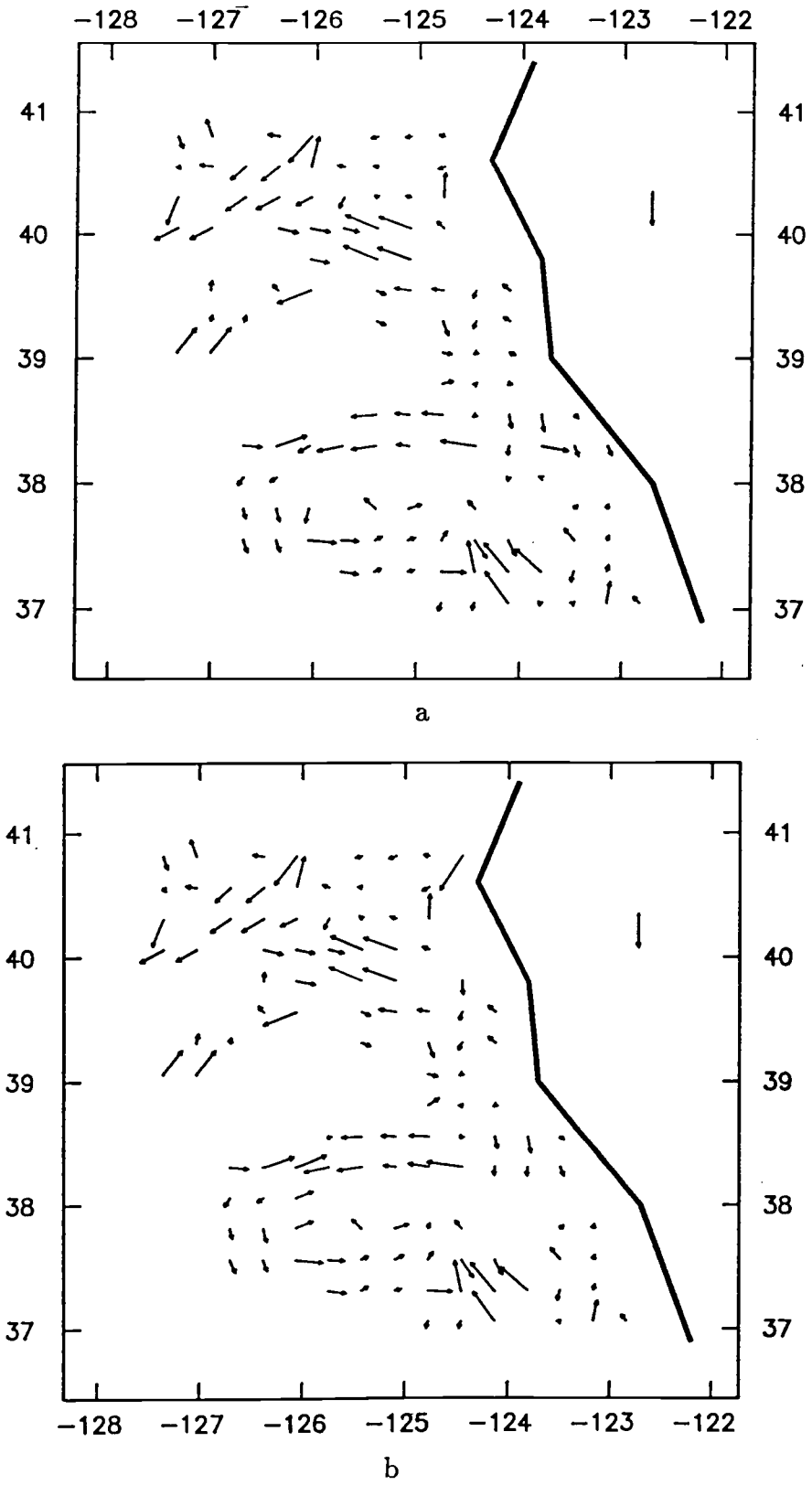

Figure 4.6 a) Gridded MCC velocity field, grid points 20 km apart, derived from CZCS image pair. b) Gridded MCC velocity field, grid points 25 km apart, derived from CZCS image pair.

fields looked random. Similar results were obtained when the gradient operator was applied to AVHRR images. The results are consistent intuitively with the assumption that the thin gradient structures observed in ocean satellite imagery defined by temperature and pigment color will deform much more rapidly than the structure of an ice field. Correlations of these thin gradients also decrease much more rapidly than correlations of the raw SST features as the field deforms.

4.3 Quantitative Tests

Two experiments were done to quantify the sea surface velocity fields produced by the MCC method. An experiment using synthetic images produced from a model velocity field gives a rough estimate of the maximum allowable time that images can be separated. *In situ* data are also used for comparison with MCC velocity fields derived from real imagery.

4.3.1 QG Model and Synthetic Imagery Description

To validate the velocity fields determined by the MCC method a numerical model is used to produce a set of synthetic temperature fields. The model is initialized using CTD (conductivity, temperature, and depth) field data from a survey of the coastal ocean off Northern California. Acting under the assumption that the model velocity fields are realistic, the model velocity fields are used to advect an SST field from an infrared satellite image from the same time period as the initial CTD field, producing synthetic images at regularly spaced times. The MCC method is then applied to the synthetic images. The resulting MCC velocity

fields are compared with the model fields used to create the images, to determine the RMS errors in the MCC method.

The model, the Harvard Open Ocean Model (*Robinson and Walstad*, 1987), was applied to an area off the Northern California Coast between 37° and 40° N. The quasigeostrophic (QG) equations are the basis for the model, as described in Appendix D. The QG approximation is valid for flows in which the vertical scale is much smaller than the horizontal scale and where the flow is primarily horizontal and horizontally nondivergent. The model was run with a flat bottom and no surface forcing. CTD data from May 18 to 27, 1987 during the Coastal Transition Zone (CTZ) experiment were used to initialize the model. The model grid spacing was 3 km.

The clearest AVHRR image available close to the time when the model was initialized, 19 May 1987 1900 local time, provides the initial SST field. Clouds in the image were removed using channels three and four (3.7 and 10.3 μm), assuming that clouds are generally colder than the sea surface and that a subregion (5 x 5 pixels) with high variance is likely to be contaminated with clouds (*Coakley and Bretherton*, 1982). Looking at plots (Figures 4.7 a,b) of the mean values versus their variances for each channel independently, threshold values can be set to eliminate the clouds. If the mean of a subregion for either channel three or four is less than the threshold value selected for the channel, then the region is flagged as cloud. If a subregion passes this test, then the variance of a region is examined based on the theory that small clouds will increase the variance of a subregion

because an area with no clouds will have a small variance. If the variance of either the channel three or channel four subregion exceeds the thresholds selected for the image, then the area is again flagged as cloud. Thus, cloud-free regions are defined by points lying in a rectangular region with $\bar{T} \geq T_{min}$ and $\sigma_T \leq \sigma_{max}$ (Figure 4.7). Any areas flagged as cloud were given interpolated SST values using the nearest cloud-free data points.

After removing the few clouds in the image, the image was rotated 27° counterclockwise to coincide with the grid of the model. A rotated image is created by applying a rotation matrix (*Mostafavi et al.*, 1978) to the image. The matrix is

$$\begin{pmatrix} cos\theta & -sin\theta \\ sin\theta & cos\theta \end{pmatrix}, \theta = \text{ angle of rotation}$$

A value located at x,y is moved to the coordinate $x1,y1$ as described below.

$$\begin{pmatrix} cos\theta & -sin\theta \\ sin\theta & cos\theta \end{pmatrix} \begin{pmatrix} x \\ y \end{pmatrix} = \begin{pmatrix} x1 \\ y1 \end{pmatrix} \tag{4.2}$$

The rotated image section, approximately 150 x 340 km (Figure 4.9d), is advected using the velocity fields produced by the model. The advection equation, equation 4.3, is implemented with the leapfrog numerical method.

$$\frac{\partial T}{\partial t} + u\frac{\partial T}{\partial x} + v\frac{\partial T}{\partial y} = 0 \tag{4.3}$$

where T = temperature and u, v = velocity fields. The leapfrog method requires that there exist two steps in time of initial data. The data for the second time step are created using a single time step (Euler) method. Euler's method uses a centered difference in space and an explicit forward step in time to compute the

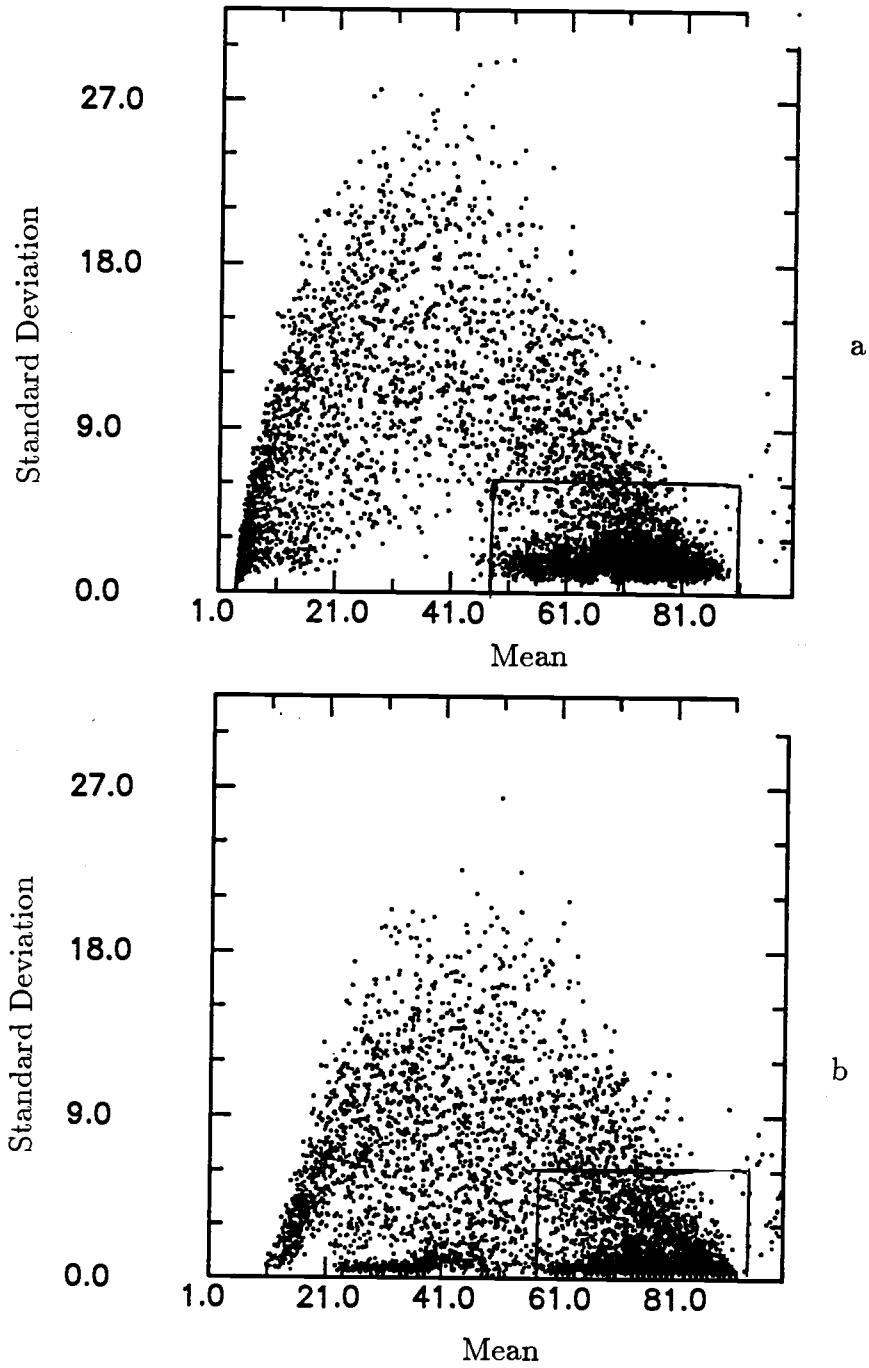

Figure 4.7 Mean vs standard deviation of SST field from channel 3 (a) and channel 4 (b). AVHRR image from Day 139, 1987 3:00 GMT

next time step. At time step n, the next time step is computed as

$$T_{i,j}^{n+1} = T_{i,j}^{n} - \frac{1}{2}\frac{\Delta t}{\Delta x}\left[u_{i,j}^{n}(T_{i+1,j}^{n} - T_{i-1,j}^{n}) + v_{i,j}^{n}(T_{i,j+1}^{n} - T_{i,j-1}^{n})\right] \qquad (4.4)$$

The leapfrog method is applied to determine the temperature fields for the rest of the time steps. The leapfrog method uses data that are centered both in time and space.

$$T_{i,j}^{n+1} = T_{i,j}^{n-1} - \frac{\Delta t}{\Delta x}\left[u_{i,j}^{n}(T_{i+1,j}^{n} - T_{i-1,j}^{n}) + v_{i,j}^{n}(T_{i,j+1}^{n} - T_{i,j-1}^{n})\right] \qquad (4.5)$$

The grid is such that u, v and T are located at the same i, j, and t. Advecting an image in this manner introduces numerical dispersion which results in an artificial decrease in advective velocities (*Mesinger and Arakawa*, 1976). The advective velocity is $c^* = c\frac{sin(k\Delta x)}{k\Delta x}$, where k=wave number, and c = the true velocity. Values of $\frac{sin(k\Delta x)}{k\Delta x}$ as a function of k are shown in Figure 4.8, where $\Delta x = 1$ and λ ranges from 1 to 50 ($k = \frac{2\pi}{\lambda}$). The attenuation increases exponentially as the wavelength decreases, but for wavelengths above 10 pixels (approximately 11 km), attenuation of the true velocity is less than 10%. Since the correlation method uses subimages of length 25 km and greater, the numerical dispersion should not contribute significantly to errors in the displacements of these subimages. It may, however, distort the smaller features within the subimages, reducing the correlations to some degree.

The time step used in the advection was one quarter hour as determined by the spacing of the image data (about 1 kilometer) which satisfies the Curant-Fredrichs-Lewy (CFL) condition for two dimensions: $|v|\sqrt{2}\frac{\Delta t}{\Delta x} \leq 1$. For time steps of 15 minutes, $|v|$ should be less than 0.8 m$\cdot$s^{-1}, which is true for the model velocity fields used. Hourly model velocity fields were subsampled every quarter of an hour and interpolated to the pixel locations to advect the images. Synthetic

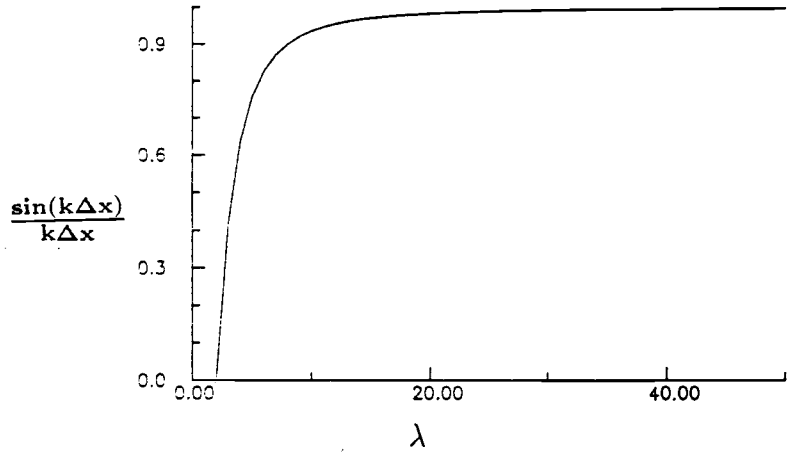

Figure 4.8 Numerical dispersion curve for advection model λ versus $\frac{sin(k\Delta x)}{k\Delta x}$

images were created for the times 6, 12, 18, 24, 30, 36, 42, and 48 hours after the initial image (Figures 4.9 b,c, and d). Figure 4.9a shows the domain of the model.

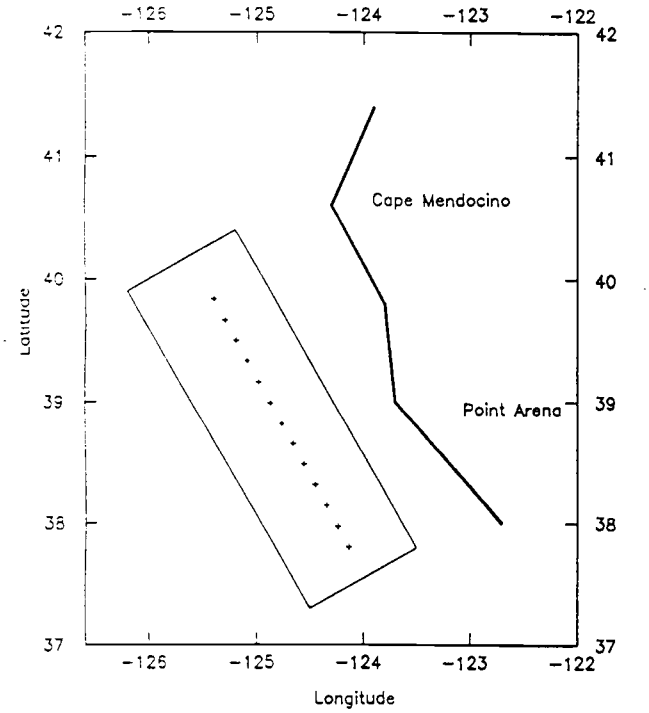

Figure 4.9 a) Domain of QG model and location of centerpoints of subimages used in the MCC method applied to the synthetic images.

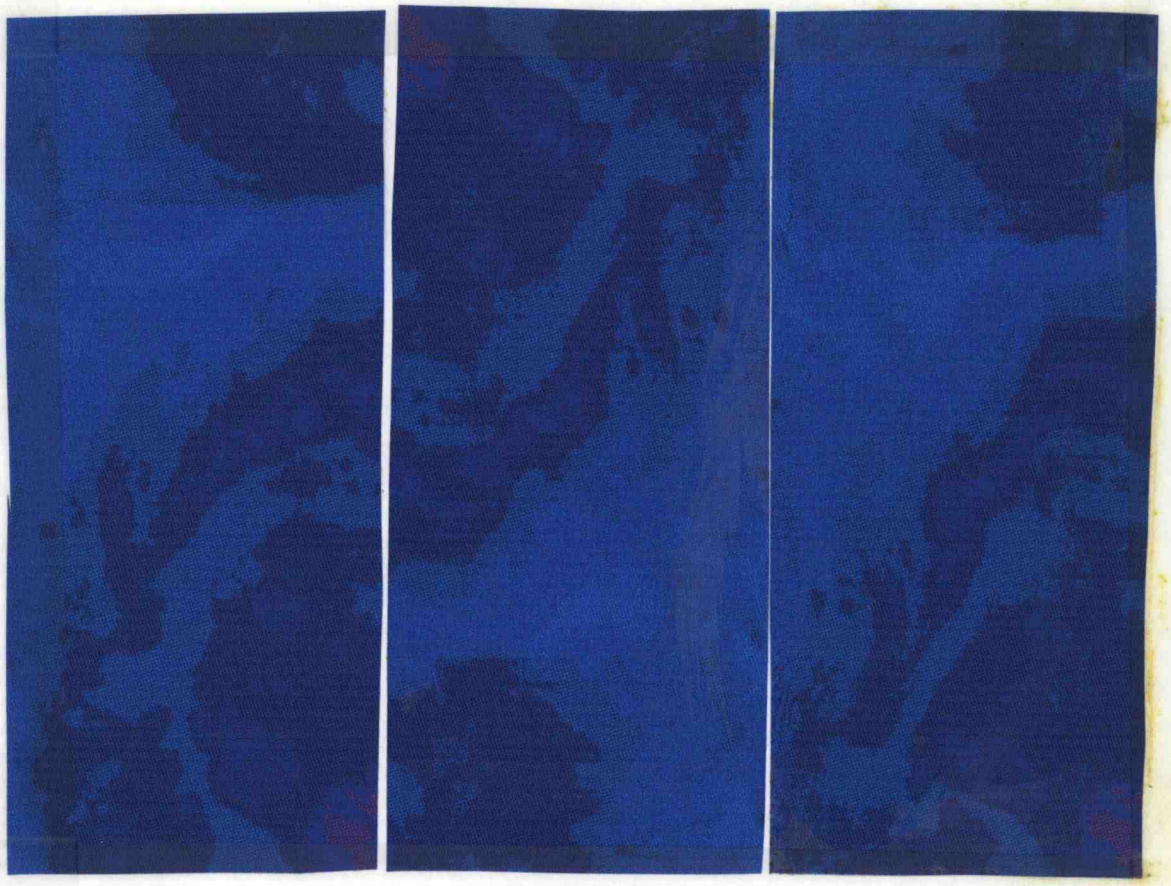

b c d

Figure 4.9 Synthetic imagery b) Original image t=0 hour c) advected image, t=12 hours, d) advected image, t=24 hours

4.3.2 Comparison of Model Velocities to MCC Method

The MCC method was applied to fields of SST from the synthetic images and also to horizontal gradients of those images, using various subimage sizes and search areas. The resulting velocity fields were then compared to the model velocity fields used to produce the synthetic images. The comparisons used all the vectors produced by the MCC method. That is, vectors were not excluded on the basis of low correlation values. The field data used to initialize the model

limited the domain size (150 x 340 km) of the model. Combined with a large search area at 24 hours, the domain size limited the number of vectors to only 13 points per image pair. Figure 4.9d shows the locations of the center of the subimages that were tracked. Search areas in the second image varied depending on the time separation between the images using the assumption that velocities were less than 0.5 $m \cdot s^{-1}$. For 6 hours, the search distance extended out 15 km on every side, increasing to 50 km for periods of 24 hours and longer. Larger search areas could not be used due to the domain of the QG model. This search area is only consistent with the assumption of 0.5 $m \cdot s^{-1}$ velocities for separations 30 hours or less and the results presented here are restricted to separations of 6 to 30 hours.

Initial tests produced the best results using the 50 km x 50 km subimage size and raw SST rather than gradients. When subimages of approximately 25 km x 25 km were used, only the 6 hour separation time, the shortest tested, resulted in vectors consistent with the velocity fields used to advect the images originally. The RMS difference for the 6 hour separation is 0.12 $m \cdot s^{-1}$. The RMS difference is defined as

$$\text{RMS difference} = \left[\left(\sum_i (u_{1i} - u_{2i})^2 + (v_{1i} - v_{2i})^2 \right) / N \right]^{1/2} \tag{4.6}$$

where N = number of vectors used in RMS difference formation and the subscripts 1 and 2 refer to satellite-derived and field velocities, respectively. The rest of the separations have RMS differences of 0.38 $m \cdot s^{-1}$ and greater. When the gradient operator is used on the 25 km x 25 km subimages, the resulting vectors have RMS

differences greater than if no gradient operator is applied, ranging from 0.20 $m \cdot s^{-1}$ for the 6 hour time separation to a the maximum RMS value of 0.59 $m \cdot s^{-1}$. The maximum correlation values associated with each vector average about 0.78 for raw SST, while application of the gradient operator cause the correlations to drop to approximately 0.4.

Better results were obtained with the 50 x 50 km subimage size. Figure 4.10 shows the relation between the separation time and both the RMS difference and the average of the vectors' associated correlations. As the time separation increases, the average correlation coefficient associated with a vector decreases while the RMS difference increases. Therefore, as time increases, a subimage is less likely to be correlated with a subsequent image. The 6 hour, 12 hour and 18 hour separations have RMS differences ranging from 0.14 to 0.22 $m \cdot s^{-1}$. For separation times of 24 hours and greater, the RMS differences are in the 0.4 $m \cdot s^{-1}$ range. If average velocity fields are formed from all pairs of simulated images separated by the same time period, the RMS difference drops from 0.14 to 0.11 $m \cdot s^{-1}$ for 6 hour separation (7 image pairs), from 0.22 to 0.11 $m \cdot s^{-1}$ for 12 hour separation (6 image pairs), and from 0.36 to 0.30 $m \cdot s^{-1}$ for 24 hour separation (4 image pairs). The 18 hour separation average stays about the same (5 image pairs) as the RMS difference from the initial MCC velocity field. Figure 4.11 shows the plot of time separation versus the average correlation values and the RMS differences of the averages when using all pairs of simulated images which have the same separation time to form an average vector field. More pairs were

available for averaging with the shorter time separations. Generally, the more pairs used, the lower the RMS difference.

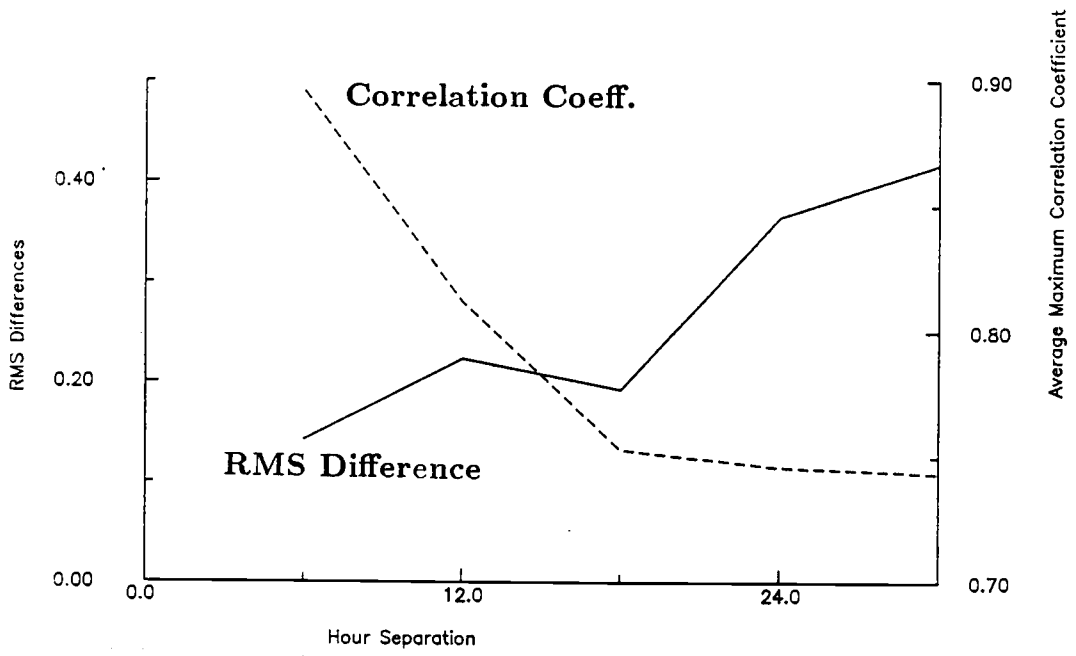

Figure 4.10 RMS differences between the MCC velocity fields derived from the synthetic images and the QG model velocity field versus the separation in time of the synthetic images. The dotted line shows the average maximum correlation coefficient for each field.

Correlating the velocity vector field from the model with those produced by the MCC method provides another measure of the similarity of the two velocity fields. The theory used for complex correlation is described in *Bendat and Piersol* (1986), *Johnson* (1986), and *Kundu* (1976). The complex correlation coefficient can be written in polar coordinates as $\rho = \rho_v e^{i\theta}$. ρ_v is the magnitude of the correlation and lies between 0 and 1. θ is the average angle between the two vector fields and is valid only if the magnitude is significant. For a perfect correlation,

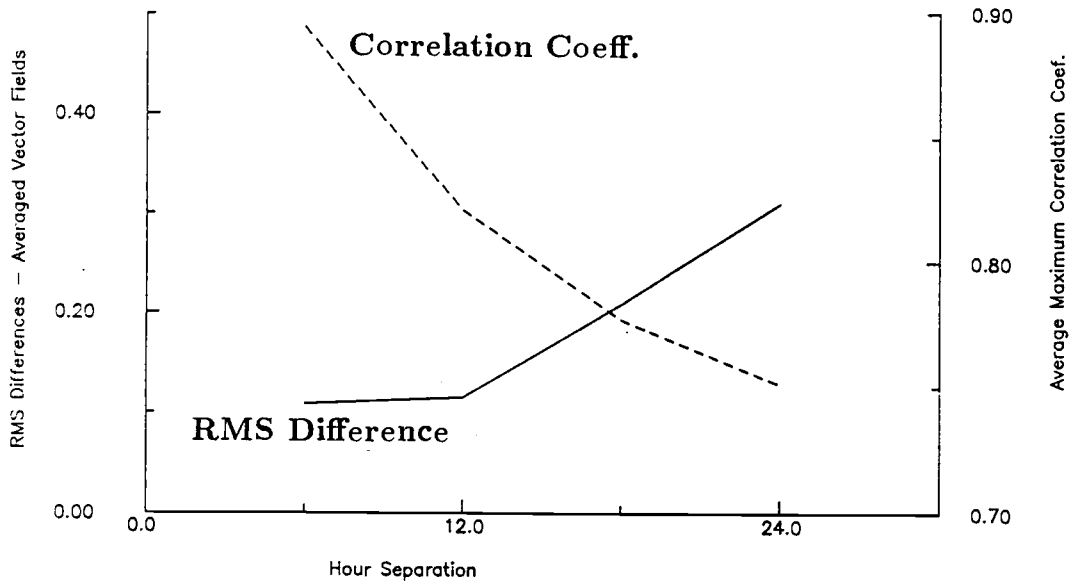

Figure 4.11 RMS differences between averaged MCC velocity fields derived from the synthetic images and the QG model velocity field versus the separation in time of the synthetic images. The dotted line shows the average maximum correlation coefficient for each field.

$\rho_v = 1$ and $\theta = 0$ degrees. The details of the complex correlation calculation are contained in Appendix B. For the purposes of this thesis, the magnitude of the complex correlation will be called the field correlation to distinguish it from the correlation values which are associated with individual vectors computed with the MCC method. Figure 4.12 shows the separation time compared to the field correlation coefficient between the model fields and the MCC method fields. For separation times of less than 24 hours, the coefficients for 6, 12 and 18 hours are high and significant (see Appendix B). The correlations are not significant for temporal separations of 24 hours and greater. The vector correlation values

in Figure 4.12 are consistent with the RMS differences as shown in Figure 4.13. With high vector field correlation values, low RMS values are observed and vice versa.

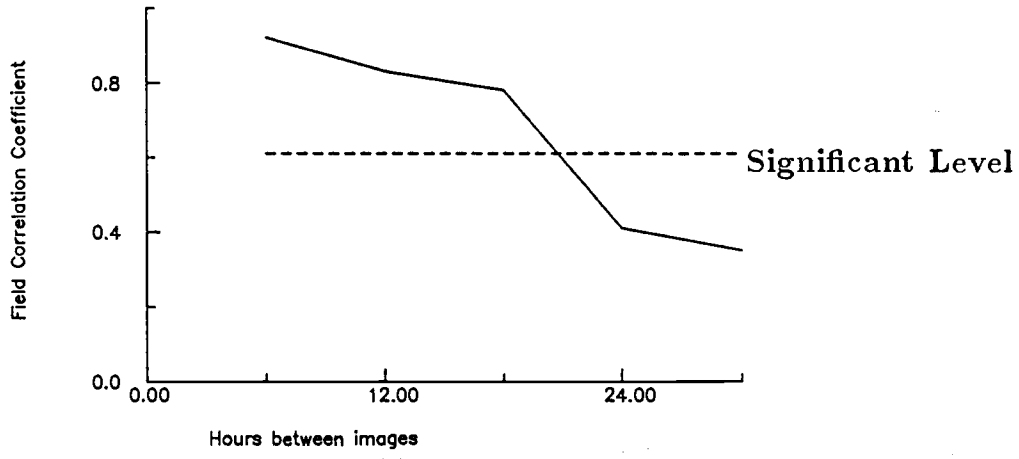

Figure 4.12 Separation in time of image pairs versus the field correlation coefficient ρ_v. The dotted line gives the 95% significance level for 13 points.

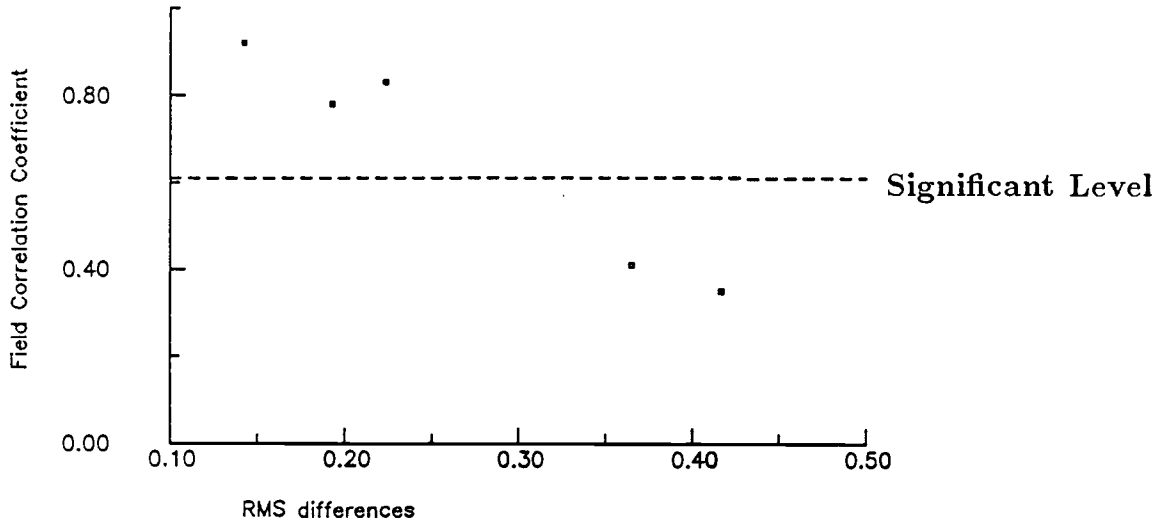

Figure 4.13 RMS differences versus the field correlation coefficient ρ_v. The dotted line gives the 95% significance level of the field correlation coefficient for 13 points.

Once the velocity vector field is produced by the MCC method, a second step can be applied to improve the estimate of the displacements. A vector consistency

check (*Collins and Emery*, 1988) is made of each vector to determine if it lies within the mean x or y displacement ± 1 standard deviation of its neighbors. If it does not, then a vector is found which has the maximum correlation in the approximately 20 x 20 km area around the mean displacement of the neighbors. For the one-dimensional line of points used with the synthetic images, the four nearest neighbors, two above and two below the one in question, contribute to the statistics used in determining the validity of the middle vector. For the two dimensional fields, compared to *in situ* data, below, the eight nearest neighbors (two in each direction) are used. Applying this procedure to the MCC velocity fields decreases the RMS value for the 24 hour separation from 0.36 to 0.23 $m \cdot s^{-1}$. For the 30 hour separation the value decreases from 0.42 to 0.29 $m \cdot s^{-1}$. The consistency check does not change the results for the image pairs separated by the shorter time periods (6, 12, and 18 hours).

4.3.3 Comparison of CODE field data to the Objective Method

To compare an MCC velocity field with *in situ* data, vectors are computed by the MCC method at the latitude and longitude positions of the ADCP measurements and at the grid points associated with the gridded geostrophic velocities computed from the dynamic height data. A direct comparison can be made to the ADCP data set without having to interpolate the data. Since the image points are approximately one kilometer apart, the comparison can be made to within half a kilometer. Each vector produced by the MCC method has an associated maximum cross-correlation coefficient. The level of significance is used to eliminate

vectors deemed to be insignificant when the correlation coefficient is below the significant value. Section 3.1 discusses the determination of the significance level. Based on tests of both CZCS and AVHRR images, a value of 0.8 is used for all image pairs. The gridded geostrophic velocity field computed from hydrography is shown in Figure 4.14a. Using only MCC vectors from the CZCS image pair with associated correlation coefficients of 0.8 and greater, the RMS differences are 0.24 $m \cdot s^{-1}$ between the hydrographic data and the MCC velocity fields. After a vector consistency check, the RMS difference decreases for this field from 0.24 $m \cdot s^{-1}$ to 0.22 $m \cdot s^{-1}$ and the field correlation, ρ_v, increases from 0.52 to 0.58 (Table 4.1). Figure 4.14b shows the MCC velocity field from the CZCS image pair after the vector consistency check is applied. Table 4.1 presents similar results for the MCC vector fields from the individual AVHRR image pairs as well as from average velocity fields formed from pairs with the same time separation. The RMS difference decreases for three of the five AVHRR fields when the vector consistency check is applied and ρ_v increases for four of the five fields. When the two 24 hour AVHRR fields are averaged (Figure 4.14c), the RMS difference increases rather than decreases and the value of ρ_v is between the two 24 hour values. The best AVHRR field is produced by averaging the three 12 hour vector fields. The resulting vector field is shown in Figure 4.14d and has an RMS difference of 0.18 $m \cdot s^{-1}$ and a field correlation value of 0.64.

From the formation of the field correlation, the average phase difference of the fields can be determined. Table 4.1 shows that the AVHRR vector fields have

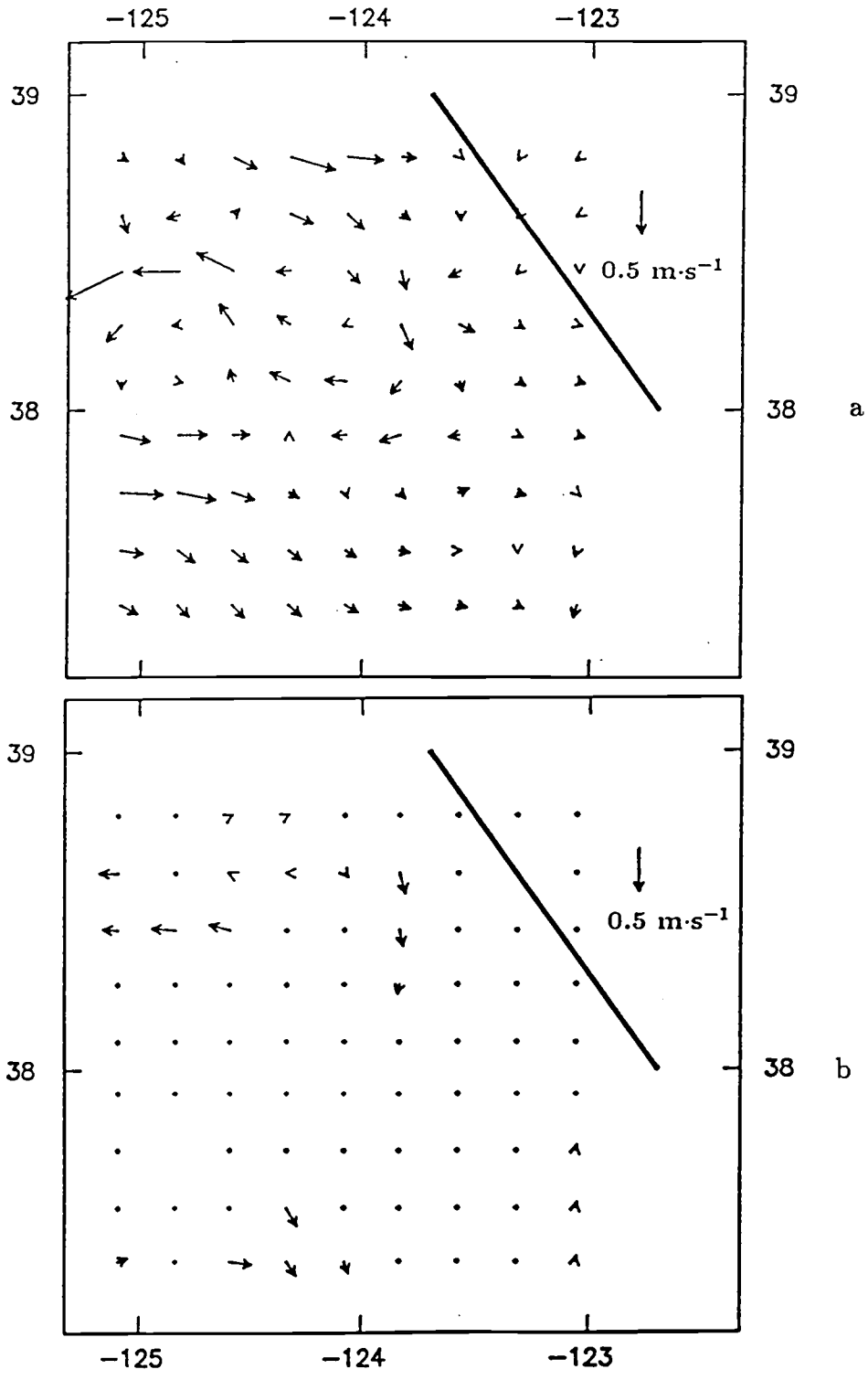

Figure 4.14 Comparison to CODE dynamic height field a) Gridded geostrophic velocities from CODE dynamic height field relative to 500 dbar b) MCC velocity field derived from CZCS images in CODE region with VCC applied.

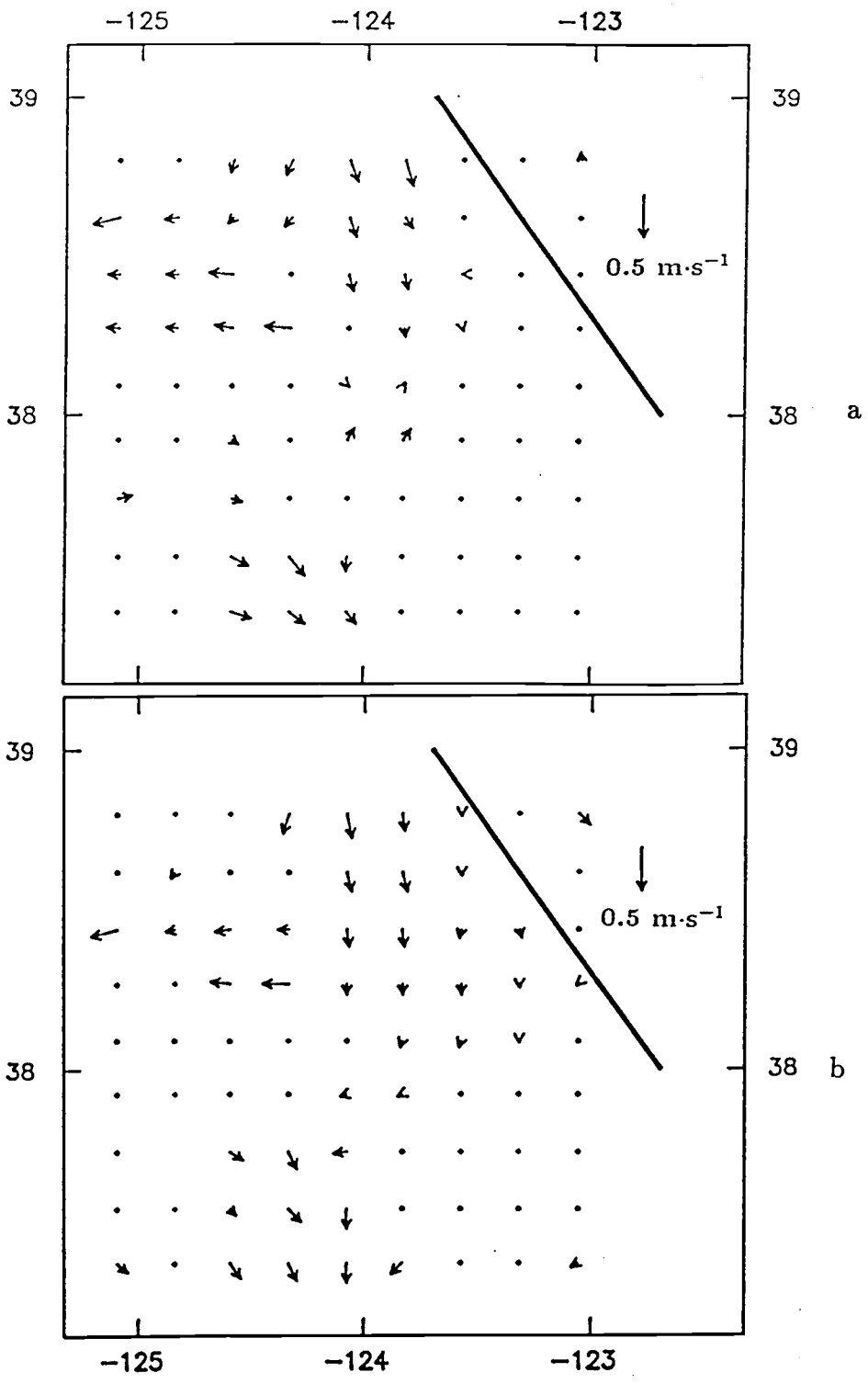

Figure 4.14 c) MCC velocity field derived from AVHRR image pair July 7,8 1500 GMT in CODE region. VCC applied. d) Averaged 12 hour AVHRR derived MCC velocity fields with VCC applied.

consistently greater differences in direction (19° to 47°) than the CZCS pair. The MCC vectors are mostly clockwise (left) of the dynamic height velocity vectors. Given the small number of images used, it can not be determined if this reflects the ability of the CZCS to see deeper into the water or is an accidental characteristic of this one CZCS image pair.

TABLE 4.1 - Comparison to Dynamic Heights

Correlation Pair	t	RMS	ρ_v	θ
Day 188/189 CZCS - 19 hr	24	0.24	*0.52	-10.7
Day 188/189 CZCS - VCC	24	0.22	0.58	-10.9
Day 188/189 AVHRR - 15 hr	24	0.22	0.48	-26.1
Day 188/189 AVHRR - VCC	24	0.22	0.56	-27.3
Day 188/189 AVHRR - 03 hr	24	0.25	*0.39	-47.5
Day 188/189 AVHRR - VCC	24	0.23	0.44	-43.3
Day 188 AVHRR - 03,15 hr	12	0.26	0.55	-39.6
Day 188 AVHRR - VCC	12	0.23	0.59	-40.7
Day 188/189 AVHRR - 15,03 hr	12	0.20	0.49	-19.0
Day 188/189 AVHRR - VCC	12	0.21	0.33	-10.7
Day 189 AVHRR - 03,15 hr	12	0.23	0.51	-21.0
Day 189 AVHRR - VCC	12	0.21	0.55	-22.0
Ave. AVHRR - 24hr VCC fields	24	0.24	0.47	-29.5
Ave. AVHRR - 12hr VCC fields	12	0.18	0.64	-23.1

* not significant, VCC = vector consistency check

A qualitative examination of Figures 4.14b and d, shows that the MCC method resolves the westward flow at approximately 38.5° N. The averaged 12 hour AVHRR velocity field (Figure 4.14d) resolves the southeastward flow at 37.5° N better than the velocity field from the CZCS image pair does (Figure 4.14b). The southward flow from 38.5° down to 38° N is also resolved by the averaged field. The CZCS imagery (Figures 4.1a,b) shows this westward flow at 38.5° N,

125° W as a region of high pigment which is being carried offshore.

Figure 4.15a shows the velocity field from the ADCP data set. Figure 5.15b shows all the vectors derived from the CZCS image pair and Figures 4.15c and d show the vectors derived from CZCS and AVHRR pairs of July 7,8 (24 hour separation) after application of the consistency check and the correlation cutoff. Table 4.2 presents statistics comparing the ADCP velocities to the MCC velocities computed at the ADCP locations. Generally, RMS differences are approximately 0.3 $m \cdot s^{-1}$, larger than those comparing geostrophic and MCC velocities (Table 4.1). Applying the consistency check reduces the RMS difference and increases the field correlation of the individual fields, but averaging the AVHRR fields does not improve the statistics (see last two lines in Table 4.2). Field correlations are slightly higher for the CZCS derived vectors in comparison to ADCP velocities than they were in comparison to geostrophic velocities. Field correlations are generally lower for the AVHRR derived velocities, although the maximum value for one pair (ρ_v = 0.61) is high. These statistics do not account for the decorrelation scale of the velocities which would reduce the number of degrees of freedom in the closely spaced ADCP set. Even if the number of degrees of freedom is not correct, the relation of the correlation coefficients within each set (either ADCP or dynamic height) will remain the same to each other.

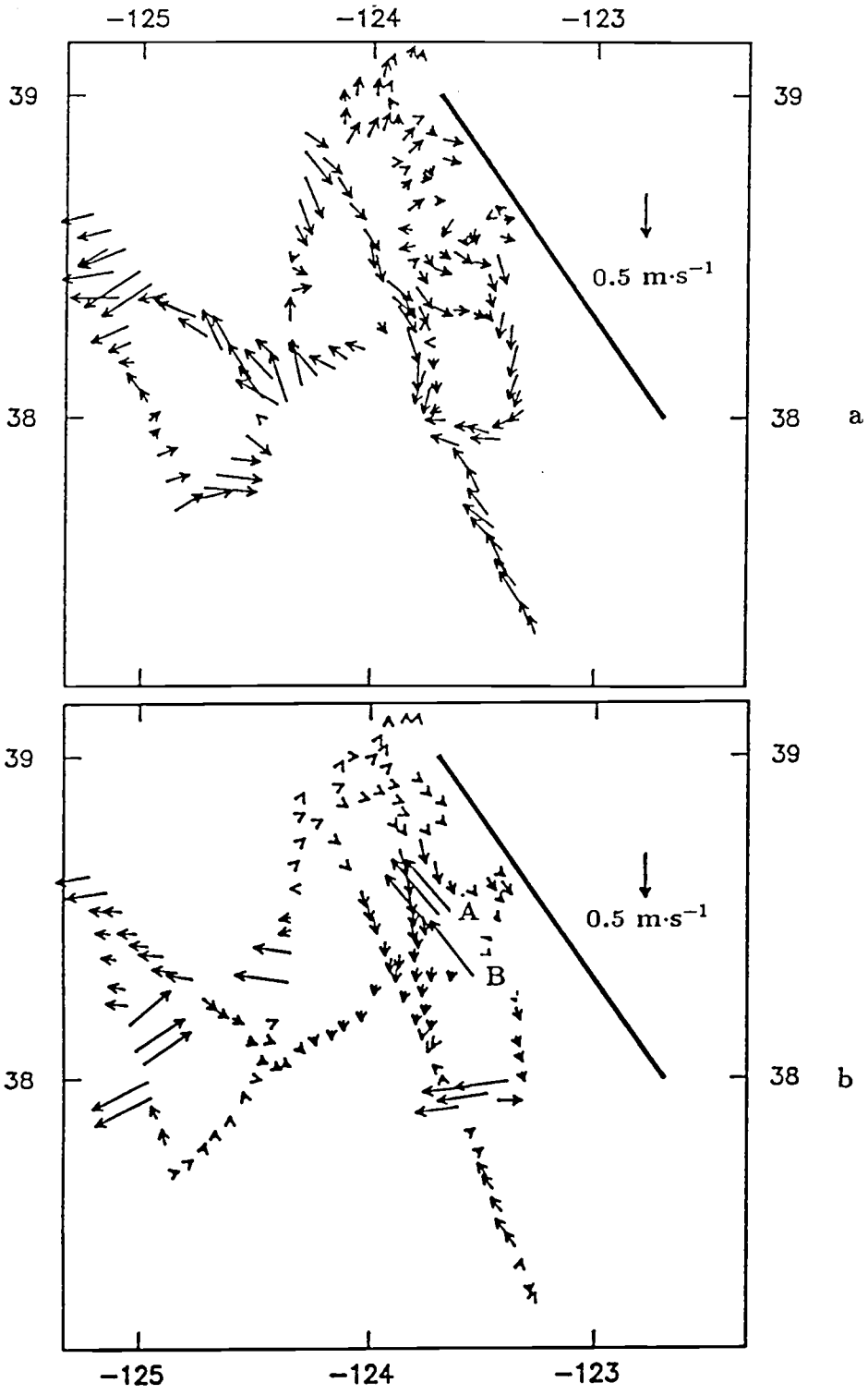

Figure 4.15 ADCP velocity fields a) ADCP velocity field - CODE Leg 7 July 4-10 1987 b) MCC velocity field derived from CZCS image pair at the ADCP locations

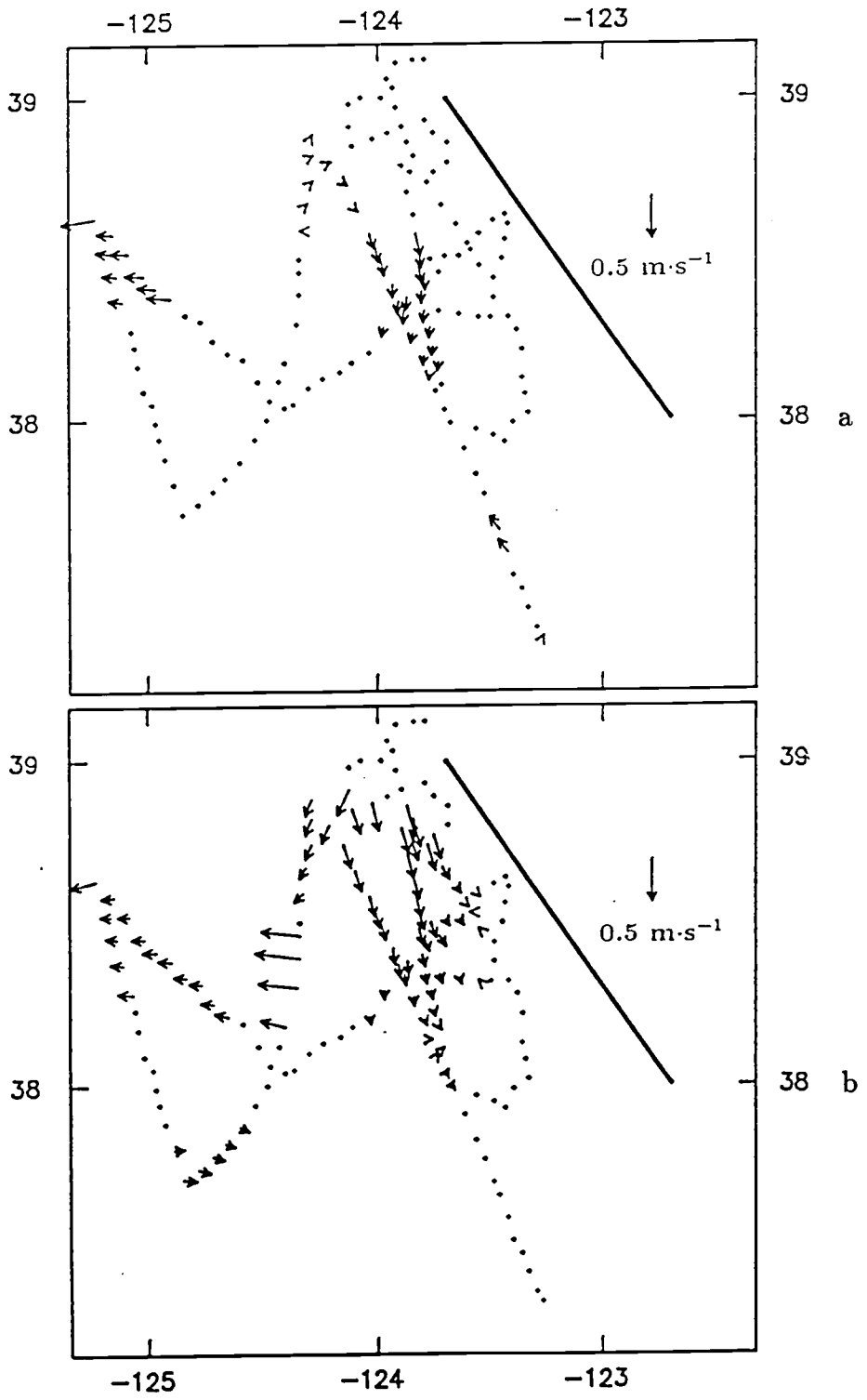

Figure 4.15 (continued) ADCP velocity fields: c) MCC velocity field derived from CZCS images with VCC applied d) MCC velocity field derived from AVHRR images 24 hours apart at 1500 GMT July 7,8 1981 with VCC applied

TABLE 4.2 - Comparison to ADCP

Correlation Pair	t	RMS	ρ_v	θ
Day 188/189 CZCS - 19hr	24	0.27	0.64	-18.5
Day 188/189 CZCS - VCC	24	0.27	0.65	-19.7
Day 188/189 AVHRR - 15hr	24	0.32	*0.18	-43.3
Day 188/189 AVHRR - VCC	24	0.28	0.38	-29.4
Day 188/189 AVHRR - 03hr	24	0.31	*0.30	84.0
Day 188/189 AVHRR - VCC	24	0.24	*0.30	81.5
Day 188 AVHRR - 03,15hr	12	0.31	0.37	-42.2
Day 188 AVHRR - VCC	12	0.27	0.42	-42.8
Day 188/189 AVHRR - 15,03hr	12	0.27	0.49	-16.3
Day 188/189 AVHRR - VCC	12	0.23	0.61	-15.1
Day 189 AVHRR - 03,15hr	12	0.34	*0.29	-23.3
Day 189 AVHRR - VCC	12	0.29	0.37	-18.4
Ave AVHRR - 24hr VCC fields	24	0.28	*0.30	-67.7
Ave AVHRR - 12hr VCC fields	12	0.23	0.46	-29.7

* not significant, VCC = vector consistency check

Qualitative examination of the CZCS and AVHRR velocity fields (Figures 4.15b, c, and d) show that the magnitude of the vectors are less than the ADCP velocity magnitudes. The westward flow is again resolved by the MCC method between 38.5° and 39° N at 125° W. In the southern portion between 37° and 38° N, the method applied to both the CZCS and AVHRR images determine the direction correctly. The southward flow at about 124° W, north of 38° N, is also resolved by the MCC method.

4.4 Discussion

To understand how the MCC method works, several aspects of the method are examined. The MCC vector fields sometimes contain clearly invalid vectors. Reasons for these vectors are explored. The RMS differences caused by differences

in both magnitude and direction are looked at separately. The reasons for the relatively high RMS difference compared to the value of *Svejkovsky's*, (1988) are also discussed.

Examination of the field correlations, ρ_v, resulting from the comparison of the CZCS MCC vectors and *in situ* ADCP data from July 7 and 8 (dates closest to the satellite images), shows these correlations to be relatively low and insignificant. An examination of two of the data points helps to explain where the MCC method fails. The points are located approximately at 123.5° W and 38.3° N in an area that does not contain sharp fronts in the CZCS images and contain vectors different from the neighboring points (Figure 4.15b - marked A and B). Looking at the CZCS images themselves (Figures 4.16a,b), the highest correlations correspond to displacements which are clearly incorrect, although the pattern of the area in the second image is similar to that in the first image. The two inconsistent vectors have corresponding MCC method correlation plots shown in Figures 4.17a,b. Both show that there exists two distinctly different areas with high correlation values, a more distant region to the northwest (blue arrows - Figure 4.16) and a closer region to the southeast (black arrows - Figure 4.16). The correlation with the distant region is slightly higher, but the velocity field in Figure 4.15a suggests that the secondary closer peak to the south is really the correct location of the displacement of the parcel of water.

One reason for the slightly lower correlation of the closer points may be due to rotation of the feature. A preliminary test on one of the points was performed

a

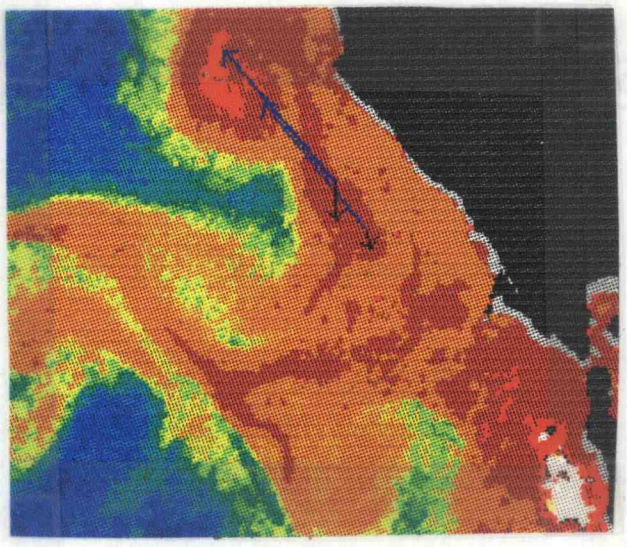

b

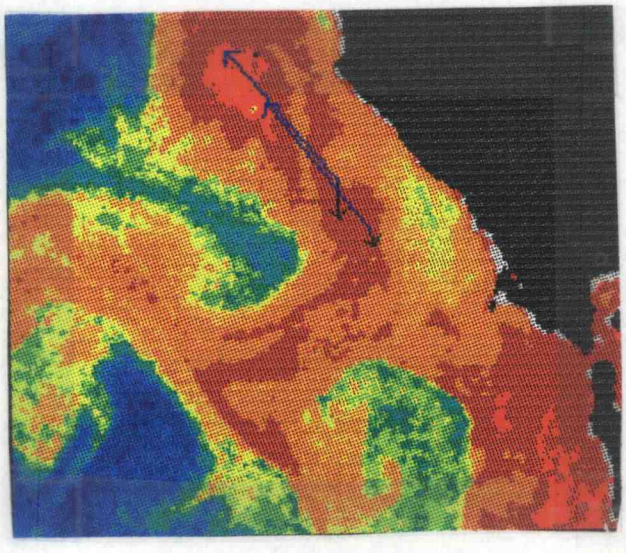

Figure 4.16 CZCS images showing displacement vectors. The black vector is the correct vector and blue, the initial, incorrect vector. a) July 7, 1981 image b) July 8, 1981 image

a

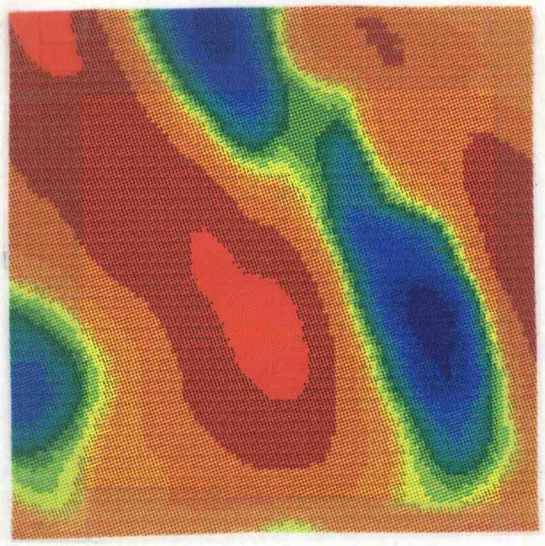

b

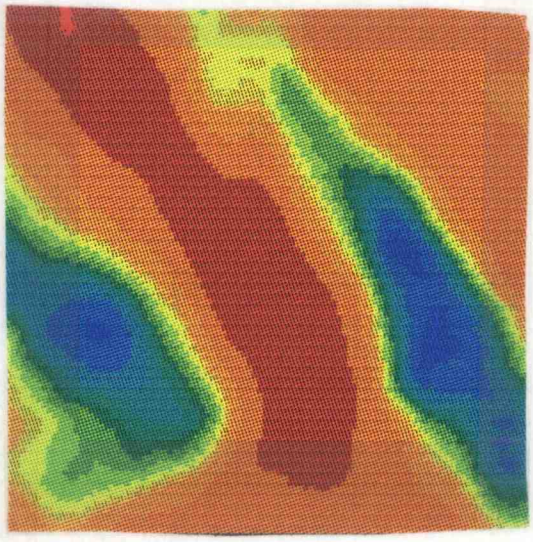

Figure 4.17 Correlation coefficient contours for all the coefficients computed by the MCC method at each lag location. Red refers to high correlation values and blue to low correlations coefficients. a) Contours with A as center point b) Contours with B as center point

by rotating the subimage by $\pm 20°$ in increments of 5°. At $-20°$ the maximum correlation was in the secondary maximum of the contour plot in the south. This test provides support for the conclusions of *Vesecky, et al.* (1987) who state that feature rotation greater than 15° reduces the ability of the MCC method to track features between images. It also suggests that efficient methods of including rotation in the MCC search might improve the results in agreement with *Kamachi* (1989) and *Emery* (personal communication).

To examine whether the RMS differences in velocity discussed above are caused equally by errors in magnitude and direction, RMS differences were formed separately for direction and magnitude of the velocities from the model generated synthetic fields and the measured ADCP and geostrophic velocities. Figure 4.18b shows the RMS difference in direction as a function of time separation for the synthetic images. This difference increases slowly with time (dotted line) for separations of 6 to 18 hours and more rapidly for longer separations. The RMS differences in direction of the vectors between the *in situ* data and the MCC vector fields are much higher, shown by the crosses on the plot. The RMS differences in magnitude are shown similarly in Figure 4.18a. There is not a consistent pattern in the distribution of the RMS differences in magnitude, although the lowest values occur for separations of 6 hours and the highest occur for 24 hours. Results from the synthetic images suggest that distortion and rotation of the features causes errors in direction of less than 30° for separations of 6 to 18 hours, increasing to 60° at 24 hours. Since the vector error is a function of the cosine of the angle, RMS

errors of 13% and 50% or more are associated with angels of 30° and 60°. Comparison to *in situ* data suggests that by time separations of 12 hours, errors of 50% are caused by errors in angle, corresponding to RMS errors of 0.15 $m \cdot s^{-1}$ or more for typical velocities of 0.3 $m \cdot s^{-1}$. Errors in the magnitude of the velocities range from 0.1 to 0.2 $m \cdot s^{-1}$. Thus, both types of errors contribute approximately equally for separations of 12 hours and the results suggest that both can be reduced by using shorter time separations.

The RMS differences found here are much higher than the value of 0.06 $m \cdot s^{-1}$ obtained by *Svejkovsky* (1988) by restricting the *in situ* velocities for comparison to be within five hours or less of the satellite image and further restricting the points to those that could be tracked easily by eye. Subjectively selecting features to track from one image to the next results in only the most distinctive features being chosen, eliminating regions with low gradients, such as points A and B in Figure 4.17. Since a person can see the whole image and can get an overall feeling of the change in the image pairs, the search is restricted to reasonable areas and grossly incorrect displacements are reduced. Rotation in features can also be tracked more easily by the eye. Automating the process with the MCC method, 1) removes the guarantee that the feature being tracked is unique and easily identified; 2) allows searches of unreasonable areas which, at times, produce random high correlations; and 3) reduces the ability to track rotating features. These sources of error could probably be improved by modification of the MCC method to include rotation, elimination of starting locations in regions of low

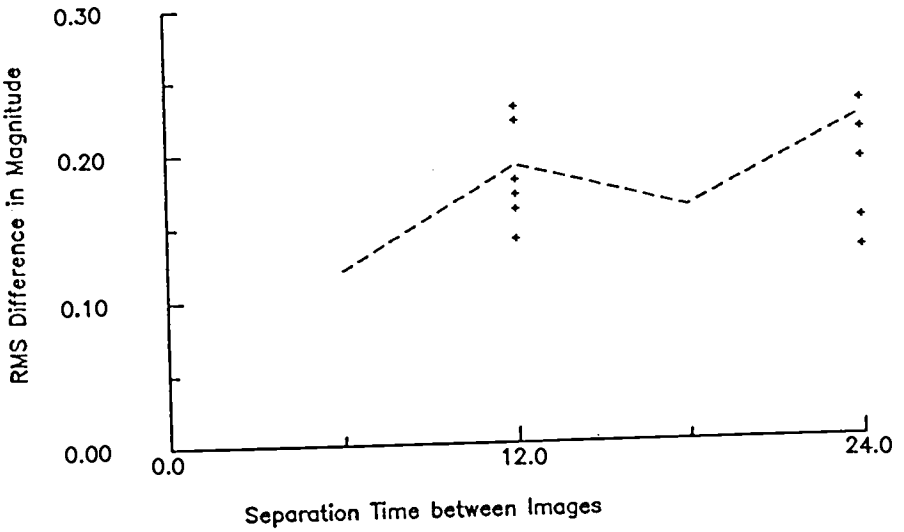

a

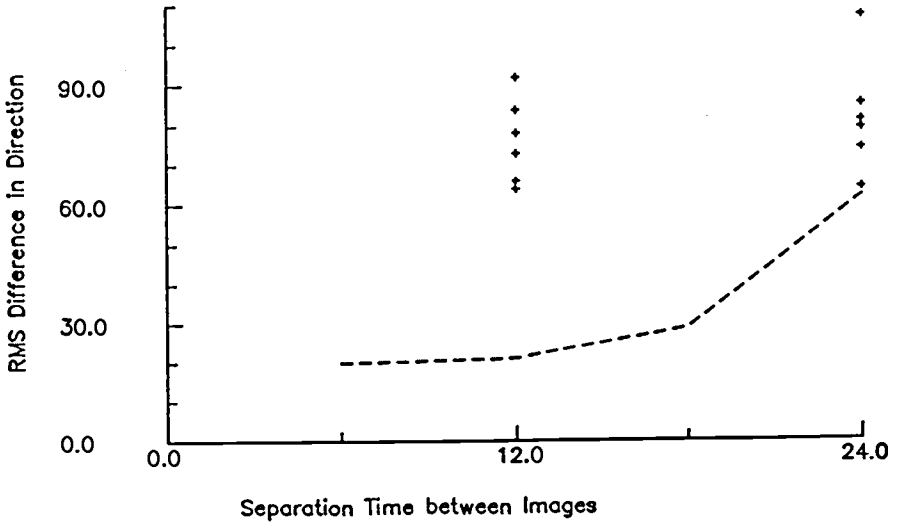

b

Figure 4.18 a) Separation in time versus the RMS difference in magnitude. b) Separation in time versus the RMS difference in direction. The dotted line on both plots indicate the RMS values computed using the synthetic images and the plus points from the real CZCS and AVHRR images.

gradients and searching the correlation matrix more intelligently. The lowest RMS errors produced by the MCC method applied to real images were obtained by averaging the three AVHRR fields with 12 hour separation and were 0.18 to 0.23 $m \cdot s^{-1}$, three to four times the value found by *Svejkovsky*. Tests with the synthetic images suggest that this could be reduced to around 0.10 to 0.15 $m \cdot s^{-1}$ if images separated by six hours are available.

Some of the difference between satellite derived and field velocities is due to the non-synoptic nature of the field data and the gridding process used to form the geostrophic velocities. An estimate of the uncertainties in the field velocities can be found by comparing the ADCP velocities to the geostrophic velocities computed at the ADCP locations. The RMS difference and field correlation values calculated between the two sets of *in situ* data (hydrography and ADCP) are 0.25 $m \cdot s^{-1}$ and 0.65, respectively. The RMS value is of the same order as the RMS differences found between the MCC velocity fields and either the *in situ* data or the model velocity field. However, the field correlation value is higher than most of the field correlation values between the MCC fields and the *in situ* data and the average angle difference is small (-1.96°). The field correlation values are more similar to the MCC fields derived from the synthetic images and the model velocities at 6 - 18 hour separation, with field correlations above 0.77 and average angles between the fields less than ten degrees. This suggests that the AVHRR image pairs should not be separated by more than 18 hours.

Physical and biological processes not accounted for by the MCC method are the main source of error between the MCC fields and either the model velocity fields or the *in situ* data. A conservation of chlorophyll equation can be written as

$$\frac{\partial p}{\partial t} + \mathbf{V_h} \cdot \nabla_h p = G + K_h \nabla_h^2 p + K_z \frac{\partial^2 p}{\partial z^2} - w \frac{\partial p}{\partial z}, \tag{4.7}$$

where p is the pigment concentration, K_h and K_z are the horizontal and vertical eddy diffusivities, G is growth/decay in chlorophyll. The MCC method assumes every thing on the right is zero and the velocity $\mathbf{V}$ is uniform over the whole subimage. Specifically, it is assumed that there is no growth or decay, no horizontal diffusivity, no vertical motion, no rotation or distortion by horizontal shears. An equivalent argument can be made for the temperature field, replacing biological sources and sinks by heating sources and sinks. Since the MCC method assumes only horizontal translation of a feature, the tests with synthetic images quantifies the error due to rotation and distortion by large scale geostrophic currents. Other physical factors contributing to changes of the features include vertical mixing and advection, horizontal diffusion, surface heating for AVHRR and biological growth and grazing of the pigment for CZCS images. RMS differences in direction from the synthetic tests compared to the RMS differences of the real images' vector fields, suggest that these additional processes have a major effect on the surface satellite-derived circulation over time periods of 12 hours and more.

4.5 Summary of the Method Validation

The tests with the synthetic images suggest that the maximum time separation between AVHRR images should be about 18 hours. The RMS differences and

field correlations improve when a vector consistency check is applied or several vector fields are averaged. The direction RMS differences at 6-18 hours are lower for the synthetic images than the RMS magnitude differences, but this is not true for real images separated by 12 and 24 hours. Tests with both real and synthetic images suggest that the best results are obtained with separation of six hours, with a lower limit for RMS errors of order 0.1 $m \cdot s^{-1}$.

The statistics of the real AVHRR and CZCS images, for this particular set of images, indicate that CZCS images at the 24 hour time separation produce MCC velocity fields as successfully as the AVHRR images do at the 12 hour time separation. The patterns of the pigment concentrations in the CZCS images used here exhibit stronger gradients which seem to persist longer than the corresponding AVHRR SST fields. Although these tests furnish evidence that the MCC method can be applied to CZCS imagery with as much success as AVHRR images, an attempt to apply the method to CZCS imagery off Cape Blanco, where strong fronts are not as evident, was not as successful. The conclusion is that strong fronts are needed to track a unique feature from one image to the next.

Much of the RMS differences at larger time separations come from the distortion and rotation of a feature, as demonstrated by tests with both the synthetic and the real images. A preliminary test suggests that inclusion of rotation in the MCC method will improve the results, although it will also increase the chance of high random correlations (by simply increasing greatly the number of correlations). Inclusion of rotation will also cause the computational requirements (already large)

to rise. The results suggest that other improvements in the MCC method may include: 1) an automated scheme to adjust starting locations in the initial image to include regions with strong gradients in the subimage; and 2) improved search strategies that are more efficient and less easily fooled by distant regions with random high correlations, perhaps by following gradients in the correlation field.

The results of the tests performed in this section show that the MCC method successfully determines the surface velocity field in some instances and fails in others. It will often show the general pattern of the circulation in regions of strong gradients, but absolute values of the velocity field contain RMS errors of 0.10–0.25 $m \cdot s^{-1}$. To put this in perspective, however, note that RMS differences between the ADCP and geostrophic velocities derived from data taken on the same cruise are also of order 0.25 $m \cdot s^{-1}$, placing the MCC results in a more positive light. Since the satellite-derived velocities are best for separations of 6 hours, operational centers which collect high-resolution AVHRR data directly from the satellites should attempt to collect pairs of images with short time separations, rather than a single image on each day. This will preserve as much of the information about surface motion as possible in the archived satellite data.

5. Sea Surface Velocities off Cape Blanco, Oregon

The second goal of this thesis is to examine a coastal ocean region and define its circulation patterns using satellite imagery. Under the right conditions, estimates of sea surface velocity fields can be made with the MCC method. An attempt to use CZCS and AVHRR imagery to describe the surface circulation pattern off Cape Blanco shows some of the problems than can be encountered in preparing a valid set of images and then interpreting the resulting velocity fields.

The California Current System has been intensively studied recently off Northern California. Only limited data are available for the area near Cape Blanco. Two studies, mentioned earlier in this thesis, the CODE and CTZ experiments, have contributed much to our understanding of this current system near coastline features such as capes. The climatological picture of the California Current is a broad (200-500 km) southward flowing, eastern boundary current, with an average velocity of 10 $cm \cdot s^{-1}$ (*Hickey*, 1989). The strongest flow is in the summer, with a velocity maximum over the continental shelf off central Oregon and seaward of the continental shelf off California. During the winter, the current either moves offshore or is replaced by the poleward-flowing Davidson current.

The instantaneous circulation pattern off Northern California is more complicated, as can be seen in the satellite images shown in section four. Complex current patterns occur near capes, including strong offshore jets and poleward flow next to the coast (*Killworth*, 1978). *Hickey* (1979) states that separations of the current from the coast at the capes may be responsible for the northward currents

observed next to the coast. Alternately, the countercurrents may be due to the changes in the curl of the wind stress from an irregular wind field near the capes.

The circulation patterns exhibit themselves in satellite images especially in the summer when upwelling occurs over the continental shelf. Winds, blowing from the north, cause the surface water to be advected westward (Ekman transport), resulting in cold bottom water being transported vertically up to replace the surface water. The onset of upwelling occurs during the March/April time period (referred to as the spring transition), when the winter winds switch to winds blowing from the north off the western coast of North America. For the Cape Blanco region, upwelling is strongest in July (*Huyer*, 1983). *Kelly* (1985) found that stronger upwelling occurs at and downstream of the capes. The upwelled water is important in the success of the MCC method, since the water is colder and usually contains higher pigment concentrations than surrounding non-upwelled water. These strong gradients produce trackable features that contribute to the success of the MCC method. Thus, it is reasonable to use the MCC method to define the surface circulation pattern during the summer/fall season near Cape Blanco.

5.1 Data Preparation

The first step in defining a usable set of images is to identify those images that have another image within 24 hours, since section four showed that this is the maximum time separation allowed. The set of images can be reduced further by identifying the images that are available off Cape Blanco. The next step in the process is time consuming. It requires that the set produced above be examined

visually to determine if the images contain enough cloud-free sea surface to track unique, identifiable features.

Analysis of the CZCS data set proved unproductive. From a total number of 734 images, only 102 contributed to an image pair in the Cape Blanco region, and of those, only 35 were clear enough to use. Table 5.1 lists the final CZCS data set.

TABLE 5.1 - CZCS Images 1978-1986 - clear

J. Day	Yr	Date	No. in seq.
181	80	June 29 - 30	2
231	80	Aug 18-19	2
275	80	Oct 1-2	2
183	81	July 2-3	2
194	81	July 13-14	2
265	81	Sept 22-23	2
147	82	May 27-29	3
242	82	Aug 30-31	2
283	82	Oct 10-11	2
105	83	Apr 15-16	2
138	83	May 18-20	3
196	83	July 15-16	2
257	83	Sept 14-15	2
263	83	Sept 20-21	2
296	83	Oct 23-24	2

The final set of AVHRR images is listed in Appendix A in Tables A.1,2. The total number of available images is 147. From that, 46 images were clear enough to be used to describe the sea surface circulation pattern. Most of these (39) are of the summer periods (May-August), making it difficult to describe an annual circulation pattern.

The original intent was to use the CZCS imagery set to describe the circulation patterns in the coastal ocean. The final set of images extracted from the complete

set is very small and does not provide enough information to describe the flow, although some of the velocity fields do contain qualitative information that can be used. Only in two instances are there two pairs available for averaging, the rest of the fields are separated by more than 48 hours. Thus, all the fields were treated independently.

Most of the images contain more clouds than would be ideal. Few vectors are left to describe the surface flow after eliminating the ones which are not significant (vectors with the associated maximum correlation value below 0.7), thus making it difficult to determine the coastal surface circulation patterns. The significance level of 0.7 was chosen instead of 0.8, because very few vectors were left after the removal of vectors below 0.8. The spring/summer velocity fields derived from the CZCS images do not define any distinct circulation patterns. The fields provide evidence that unless images are virtually cloud-free and have distinctive patterns that can be tracked with the eye, the MCC method is useless. All the images are separated by 24 hours which may make feature tracking difficult. Additionally, the images were mostly featureless.

5.2 Results and Discussion

The AVHRR data set proved to be much more successful in producing reasonable velocity fields. From the images available, velocity fields were computed by the MCC method, using a grid to identify center points, in the cloud-free regions of each image pair. The process resulted in 45 velocity fields covering January 1987 through July of 1988.

The individual fields, when examined qualitatively, exhibit flows which are consistent with the present understanding of the California Current system. The velocity field derived from the clearest winter image pair, January 19,20 1987, shows the flow to be weak and disorganized. The most coherent strong flows are flowing to the southeast at 128° W, 43.5° N (Figure 5.1) and to the west at 127° W, 40.5° N.

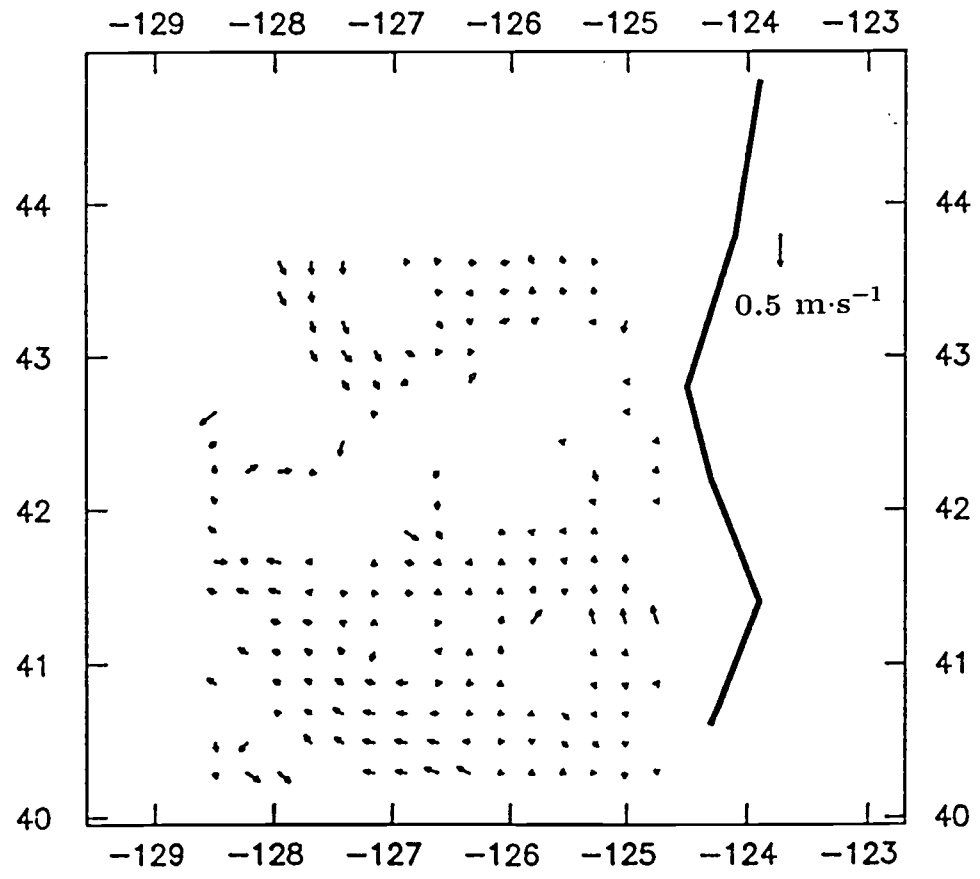

Figure 5.1 MCC velocity field derived from Cape Blanco AVHRR images of January 19,20 1987 23:00 GMT. The correlation coefficient cutoff used was 0.7

Stronger and more coherent flow patterns are seen in the summer. The best set of velocity fields are from the 1988 July sequence. After applying the vector consistency check, discussed in section 4.3.2, to the velocity field from the July 16 16:00/July 16 24:00 pair, strong offshore and southward flow can be observed north of Cape Mendocino between 125° and 127 ° W at 40.5° N (Figure 5.2). Weaker southward and offshore flow can be seen north of Cape Blanco (125° W, 43° N).

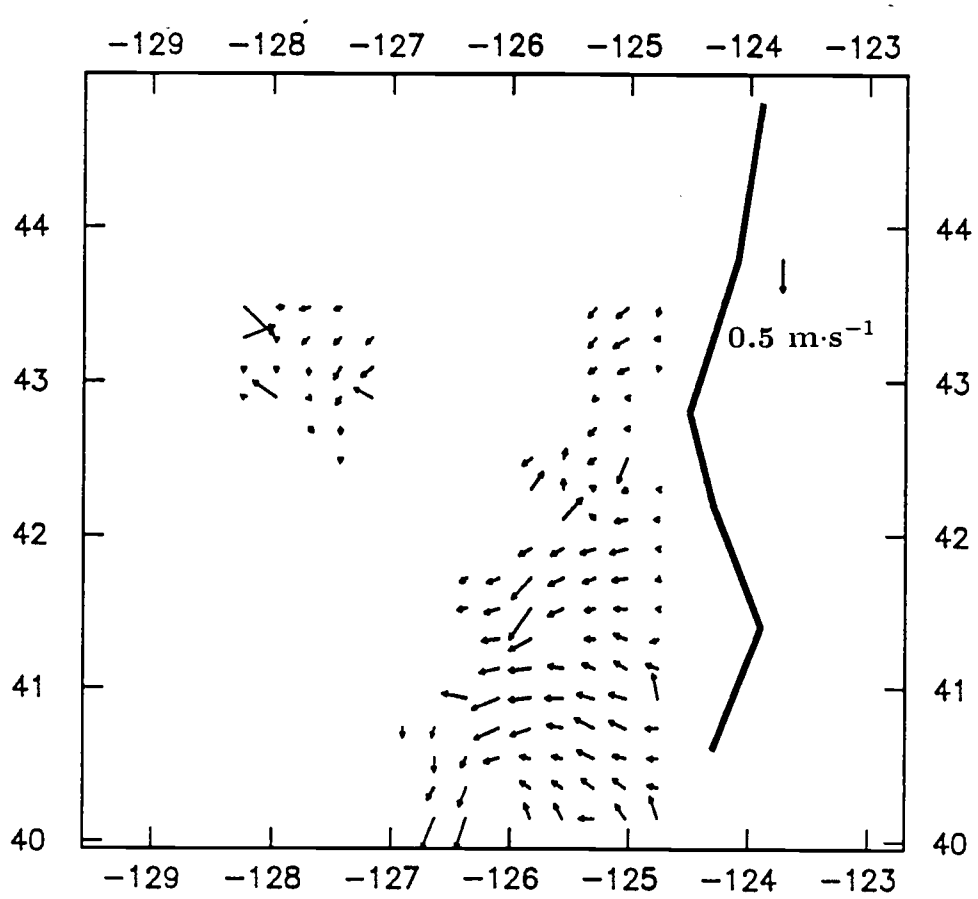

Figure 5.2 MCC velocity field derived from AVHRR images of July 16,16 1987 at 16:00 and 24:00 GMT. The correlation coefficient cutoff used was 0.7.

Further information about the velocity fields can be gained if empirical orthogonal functions (EOFs) are formed from the set. EOF analysis decomposes a time/space data set into different temporal modes to examine a set's variance (see Appendix D for further detail). The most important modes contain the largest fraction of variance in the fields (*Davis*, 1976, *Lagerloef and Bernstein*, 1987). In this thesis, only the mean product EOFs will be examined because the interest is in the general circulation pattern and not the variability of the flow over short temporal periods.

Table 5.2 shows the velocity fields used in forming the EOFs for a sequence available from the June 1,2 1987 time period. Figure 5.3 is the first EOF mean product. There is strong offshore flow north of Cape Mendocino for the first, second, and fourth velocity fields (determined by the zero phase at these locations). The third and fifth fields are not consistent with this offshore flow. The third flows more to the south while the fifth flows to the north.

TABLE 5.2 - Image Pairs for June 1,2 Sequence EOFs

Image 1	Image 2	Hr. Separation
June 1 1987 04:00	June 1 1987 16:00	12
June 1 1987 16:00	June 1 1987 22:00	6
June 1 1987 22:00	June 2 1987 04:00	6
June 2 1987 03:00	June 2 1987 12:00	9
June 2 1987 12:00	June 2 1987 16:00	4

Another sequence of five images occurs from May 18 - 20 of 1987. The velocity fields contributing to this EOF are shown in Table 5.3. The first EOF (figure 5.4)

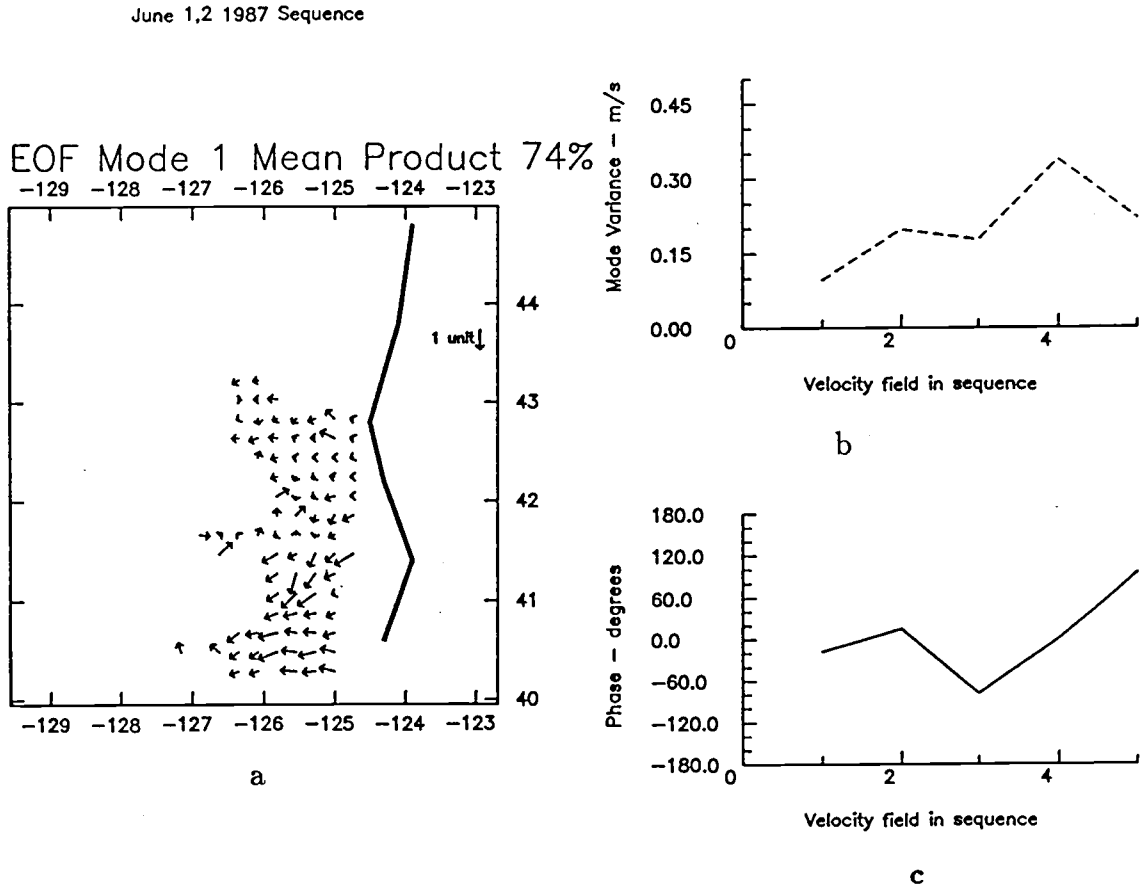

Figure 5.3 a) EOF 1 vector field decomposed from June 1,2 MCC velocity fields - mean product. EOF 1 explains 74% of the variance. b) associated amplitude time series c) associated phase time series. The horizontal axis for b and c corresponds to the position of the velocity field in the list given in Table 5.2.

shows southward flow. The phase varies between ±60°, making the flow consistently in the southerly direction. There were fewer vectors in this period because cloud cover reduced the visible area of the ocean. time period.

TABLE 5.3 - Image Pairs for May 18-20 Sequence EOFs

Image 1	Image 2	Hr. Separation
May 18 1987 13:00	May 19 1987 03:00	14
May 19 1987 3:00	May 19 1987 23:00	20
May 19 1987 23:00	May 20 1987 03:00	4
May 20 1987 03:00	May 20 1987 11:00	8
May 20 1987 11:00	May 20 1987 23:00	12

The July 1988 sequence comes from a period when conditions are ideal for the MCC method. There are five image pairs available in a short time period of 60 hours, allowing for velocity field averaging to remove incorrect vectors. Complex EOFs can also be calculated to look at the most coherent motion. The time separation between the images is less than 18 hours. Persistent winds from before and during this time period reduce effects of surface heating and differential mixing and cause strong features to exhibit themselves in the satellite imagery.

Table 5.4 lists the velocity fields used in describing the flow in July of 1988. The velocity fields were first examined visually to determine if a vector consistency check (VCC) needed to be applied. If many vectors looked incorrect, then the VCC procedure was applied to the field (see section 4.3.2). An average field, figure 5.5, was computed first to examine the flow. A strong offshore flow can be seen between

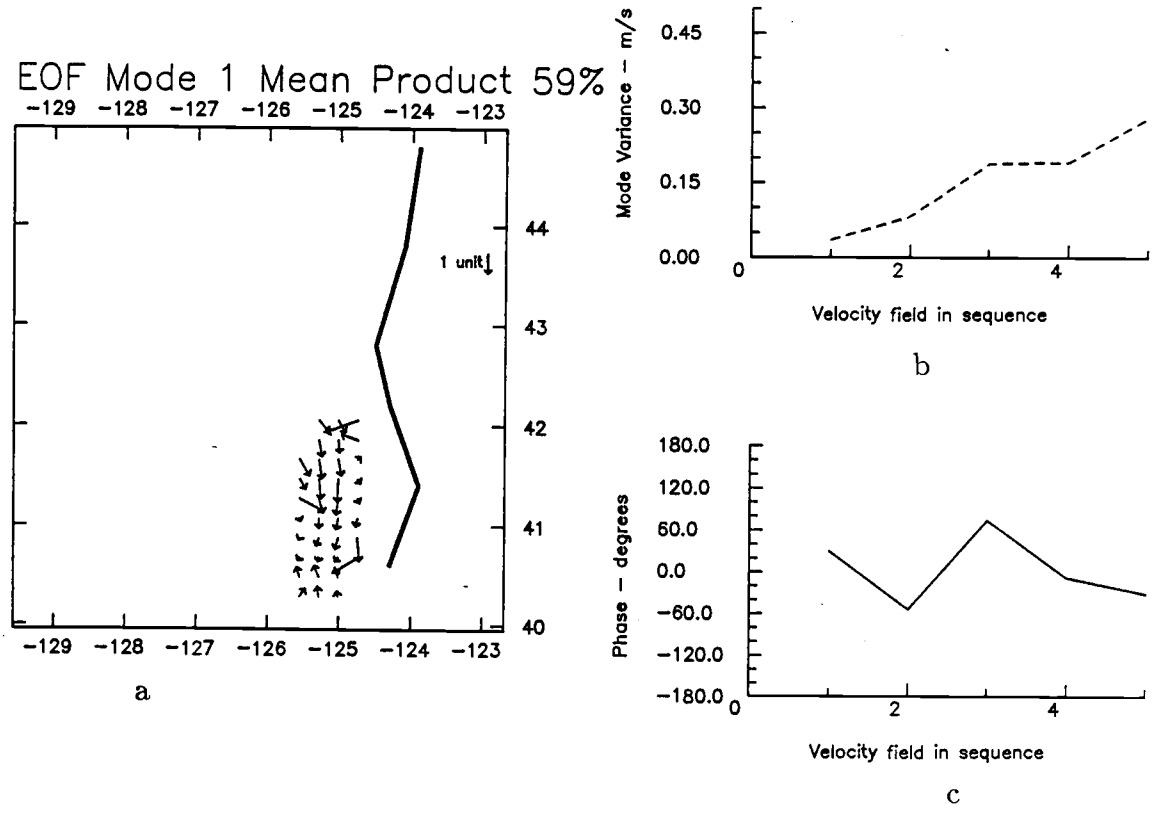

Figure 5.4a) EOF 1 vector field decomposed from May 18-20, 1987 MCC velocity fields - mean product. EOF 1 explains 59% of the variance. b) associated amplitude time series c) associated phase time series. The horizontal axis for b and c corresponds to the position of the velocity field in the list given in Table 5.3.

126° and 127° W and 41° N. There is also offshore flow north of Cape Blanco at

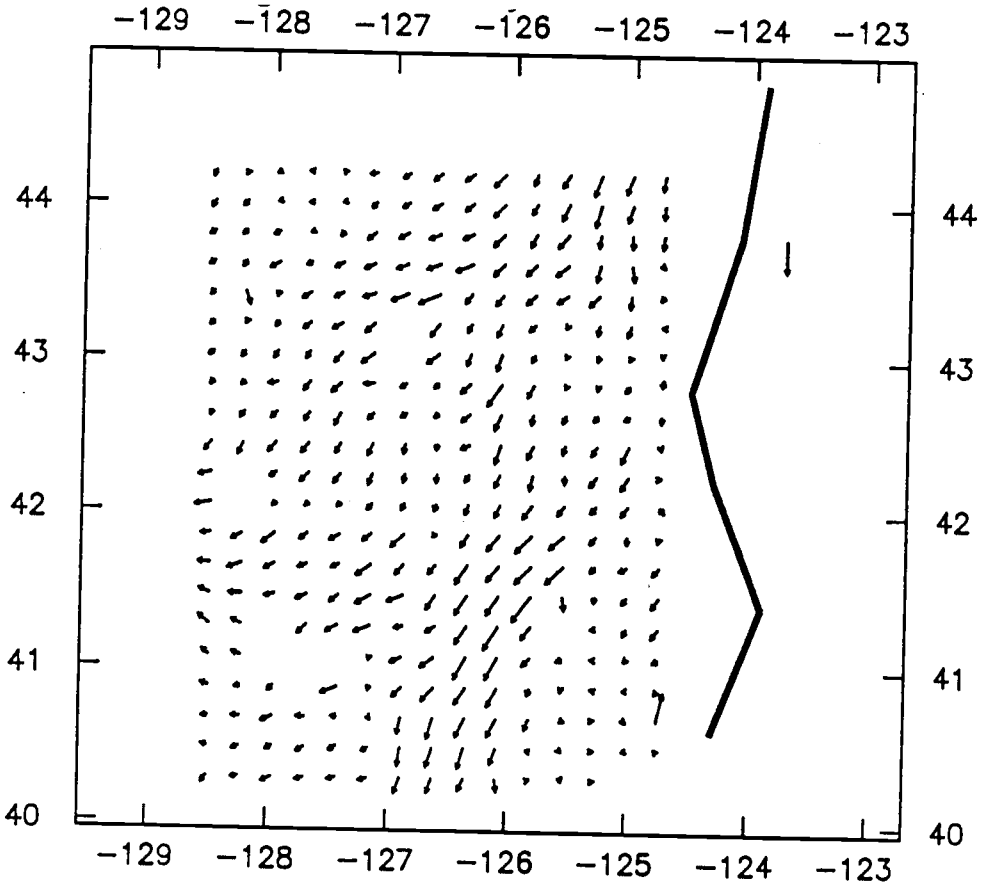

Figure 5.5 Average of July 16-18, 1988 MCC velocity fields

44° N.

TABLE 5.4 - Image Pairs for July Sequence EOFs

Image 1	Image 2	Hr. Separation
July 16 1988 16:00	July 16 1988 24:00	8
July 16 1988 24:00	July 17 1988 03:00	4
July 17 1988 03:00	July 17 1988 12:00	9
July 18 1988 17:00	July 18 1988 23:00	6
July 18 1988 23:00	July 19 1988 16:00	17

The first EOF mode explains 74% of the mean product (Figure 5.6a). The plot of the phase in Figure 5.6c shows that the field is not rotating throughout the

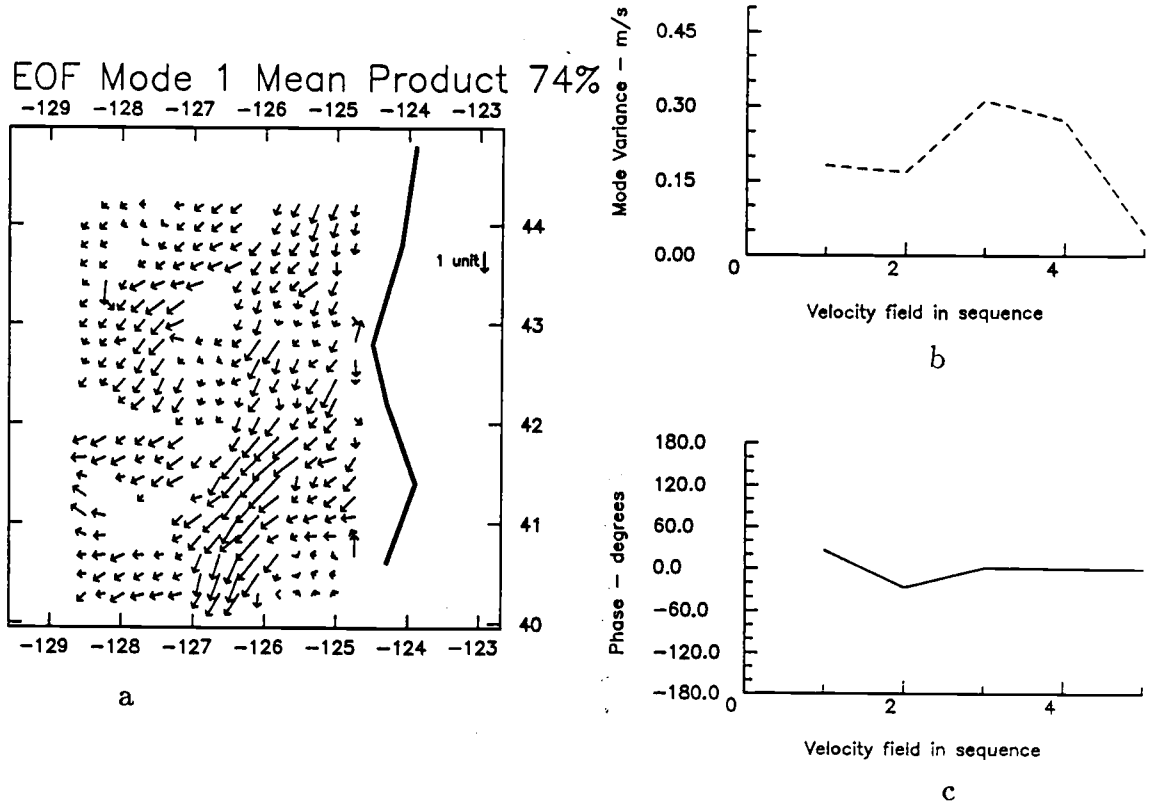

Figure 5.6 a) EOF 1 vector field decomposed from July 16-18, 1988 MCC velocity fields - mean product. EOF 1 explains 74% of the variance. b) associated amplitude time series c) associated phase time series. The horizontal axis corresponds to the position of the velocity field in the list given in Table 5.4.

sequence. Thus, the flow in this sequence of images is a southwesterly flow. An AVHRR image from the time period dated, July 16, 1988 , shown in Figure 5.7, exhibits the southward transport via the tongue of cold water in the southeastern part of the image. The first EOF resolves the strong southward flow as did the average, but the EOF gives more information than the average field, since it shows that the flow pattern does not change temporally and the dominant flow is in the southward direction. The magnitude of the southwestward flow between 125°-127°

W,. 40°-42° N is two to three units, which, when multiplied by the amplitudes in Figure 5.6b, result in maximum velocities of 0.6 to 0.9 $m \cdot s^{-1}$, similar to velocities observed farther to the south at 37° N at the time of this image sequence. Note that the amplitude is nearly zero for the fifth image pair, the only one in the sequence with a time separation greater than 12 hours. This confirms the need for pairs to have a time separation of 12 hours or less.

Examination of the divergence of the EOF 1 mean product field, Figure 5.8, shows that an area of convergence exists at 43° N, 126.5° W. Inshore and to the north is an area of divergence. This agrees with what one might expect, that inshore is an upwelling area (divergence) and farther offshore is and area of downwelling (convergence). The rms value of the divergence is $9.1 \times 10^{-6} s^1$. This is higher than the value found from the CODE drifter data (*Davis*, 1985, $3 \times 10^{-6} s^1$) and by an inverse method applied to the CODE region (*Kelly*, 1989, $4.3 \times 10^{-6} s^1$). The inverse method used by *Kelly* attempts to minimize the divergence while the MCC method does not. Additionally, the lower values found by *Kelly* include data points that are sampled at shorter spatial scales than the data points used for the MCC method.

Another way to examine the consistency of the vector fields of the July sequence is compute the standard deviation in angle and magnitude for each location over the five velocity fields. Figure 5.9 shows the average of the July 1988 velocity fields. Overlayed on the velocity field, represented by the hatched areas, are the regions where the standard deviation of the angle at each location was greater than

50°. The coherent, strong flow offshore and southward is preserved when these regions are removed. It is assumed that the high standard deviation in the angle at these points reflects the difficulty in tracking features at these locations, resulting in random velocities over the five image pairs. Use of the standard deviations in the magnitude of the velocities was less successful since the values are greatest in the regions of the strongest flow.

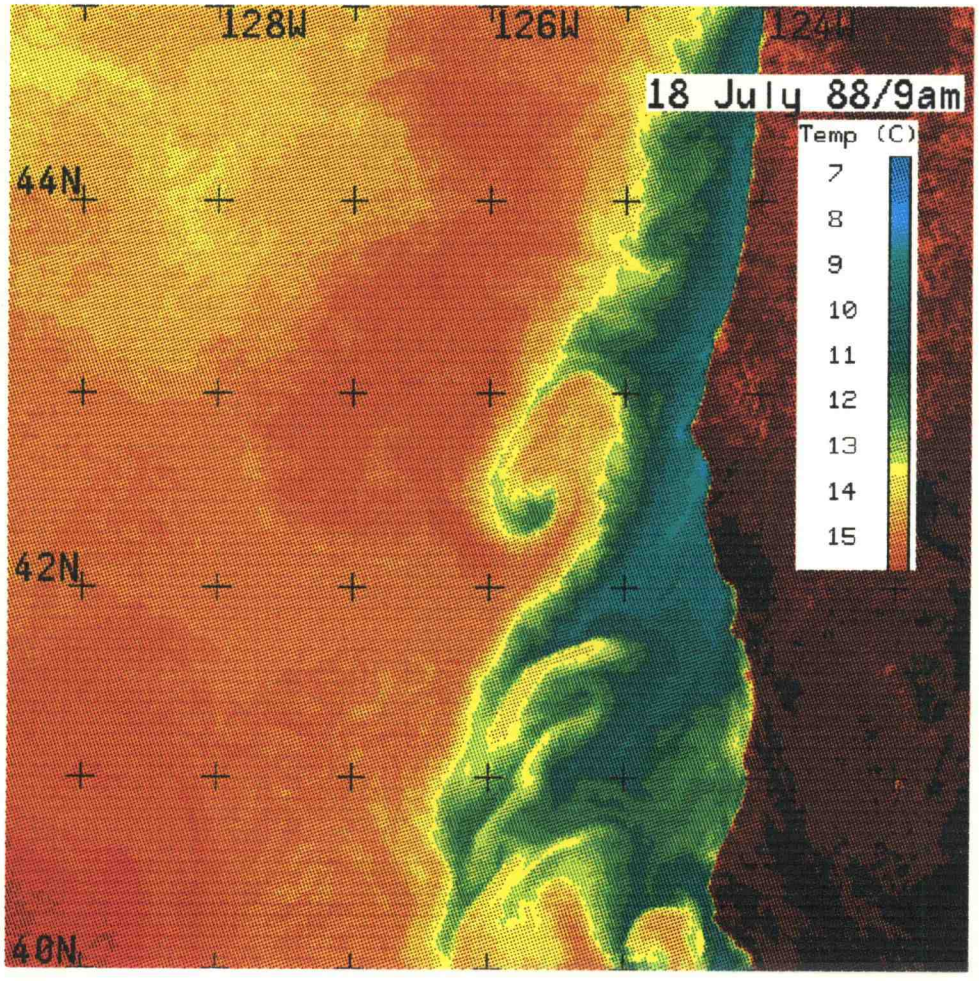

Figure 5.7 AVHRR image from July 18, 1988 16:00 GMT

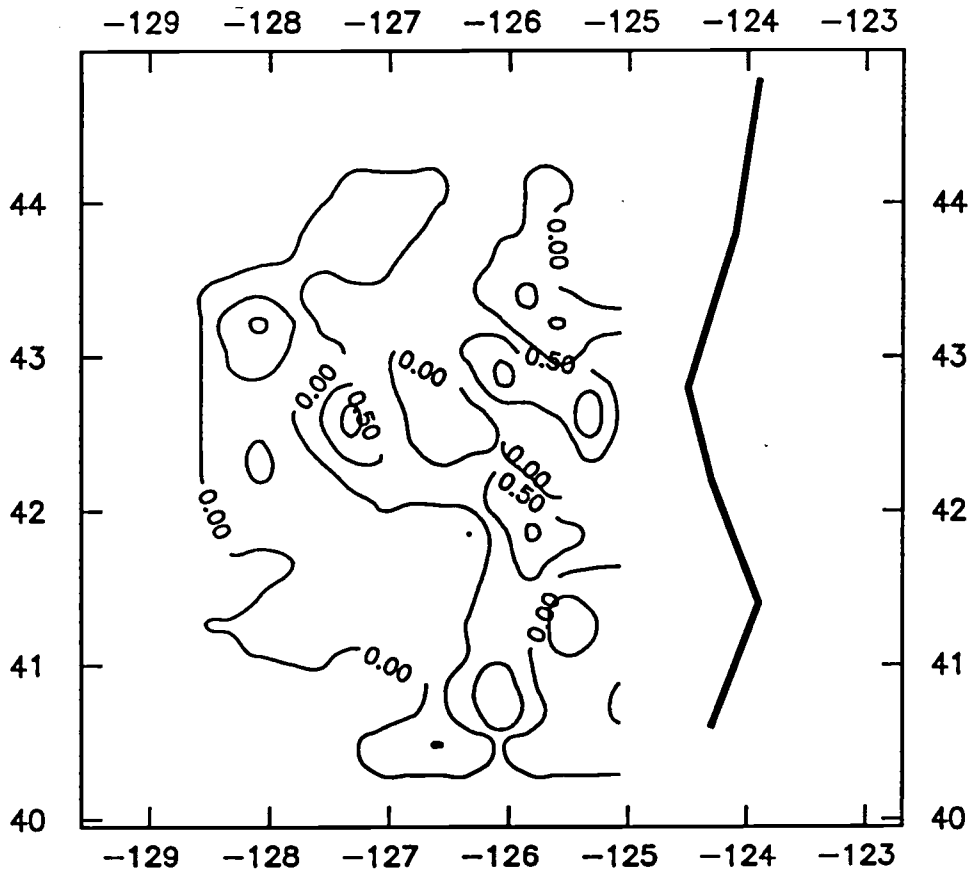

Figure 5.8 Divergence of first EOF - July sequence, units are $10^{-4}s^{-1}$.

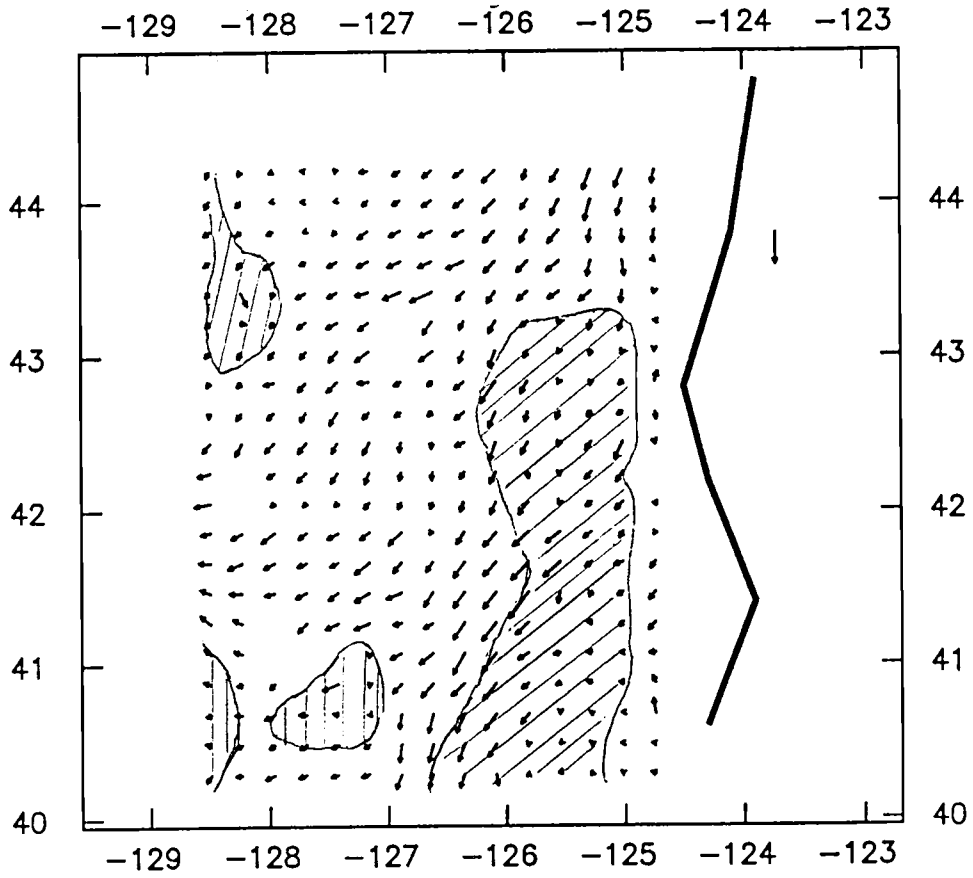

Figure 5.9 Average of July fields, overlayed with hatched area representing regions with the standard deviation in angle greater than 50°.

The same complex EOF decomposition method can be used to examine the change in the velocity fields over the whole sequence of fields, from January to September of 1987 and July 1988. Groups of velocity fields from the same time period were averaged to form a composite of the velocity field at that time. Table

5.5 lists the fields used in the EOF decomposition.

TABLE 5.5 - Image Pairs for Jan - September 1987, July 1988

Image 1	Image 2	Averaged into
Jan 19 1987 23:00	Jan 20 1987 23:00	Jan19,20
May 5 1987 22:00	May 6 1987 16:00	
May 6 1987 16:00	May 6 1987 22:00	May5,6
May 6 1987 22:00	May 7 1987 12:00	
May 18 1987 13:30	May 19 1987 03:30	
May 19 1987 3:30	May 19 1987 23:30	
May 19 1987 23:00	May 20 1987 03:00	May18,20
May 20 1987 3:00	May 20 1987 11:00	
May 20 1987 11:00	May 20 1987 23:00	
June 1 1987 4:00	June 1 1987 16:00	
June 1 1987 16:30	June 1 1987 22:30	
June 1 1987 22:30	June 2 1987 03:30	June1,2
June 2 1987 3:30	June 2 1987 12:30	
June 2 1987 12:30	June 2 1987 15:30	
July 14 1987 23:00	June 15 1987 23:00	July14,15
Aug 30 1987 23:00	Aug 31 1987 23:00	Aug30,31
Sept 26 1987 23:00	Sept 27 1987 23:00	
Sept 27 1987 23:00	Sept 28 1987 23:00	Sep26,28
July 6 1988 16:00	July 6 1988 24:00	
July 6 1988 24:00	July 7 1988 04:00	July6,7
July 9 1988 17:00	July 9 1988 23:00	July9
July 16 1988 16:00	July 17 1988 24:00	
July 16 1988 24:00	July 17 1988 03:00	
July 17 1988 03:00	July 17 1988 12:00	July16,19
July 18 1988 17:00	July 18 1988 23:00	
July 18 1988 23:00	July 19 1988 16:00	

Before computing the complex EOFs, the average velocity field was computed for each closely spaced group of fields, as listed in Table 5.5. Ten average velocity fields were used for the EOF decomposition (figure 5.10). EOF mode 1 explains 54% of the variance distribution. Mode 1 shows the southward flow of the California Current at approximately 125° to 126° W and 41° N. At Cape Blanco, an offshore flow can be seen, turning back southward at approximately 42° N. The general pattern is that of a meandering southward current, intensified to the north and offshore of the two capes. The return flow is less intense. Figure 5.10b shows that this pattern is observed to be strong during periods in May, June and July 1987, and July 1988 and less evident during other periods in January, May, August and September 1987. Little rotation of the field is seen in the first EOF ($< \pm 60°$), except for the January pair when flow was reversed in direction (to the north).

If the velocity fields are not averaged and an EOF decomposition is done, the strong southerly flow is not resolved quite as well (figure 5.11). Therefore, it seems advantageous to average nearby fields to remove extraneous vectors before computing EOFs over this long time period. This is consistent with the reduction of RMS errors found by averaging several fields in section four.

Figure 5.12 represents the divergence of the first EOF of the January through September sequence of velocity fields. North of Cape Blanco at 43.5° N is an area of convergence, representative of downwelling water. This could mean that the colder, denser upwelled water is being subducted as the flow turns onshore. Again, north of Cape Mendocino at 41° N, 125.5° W, there is an area of divergent flow

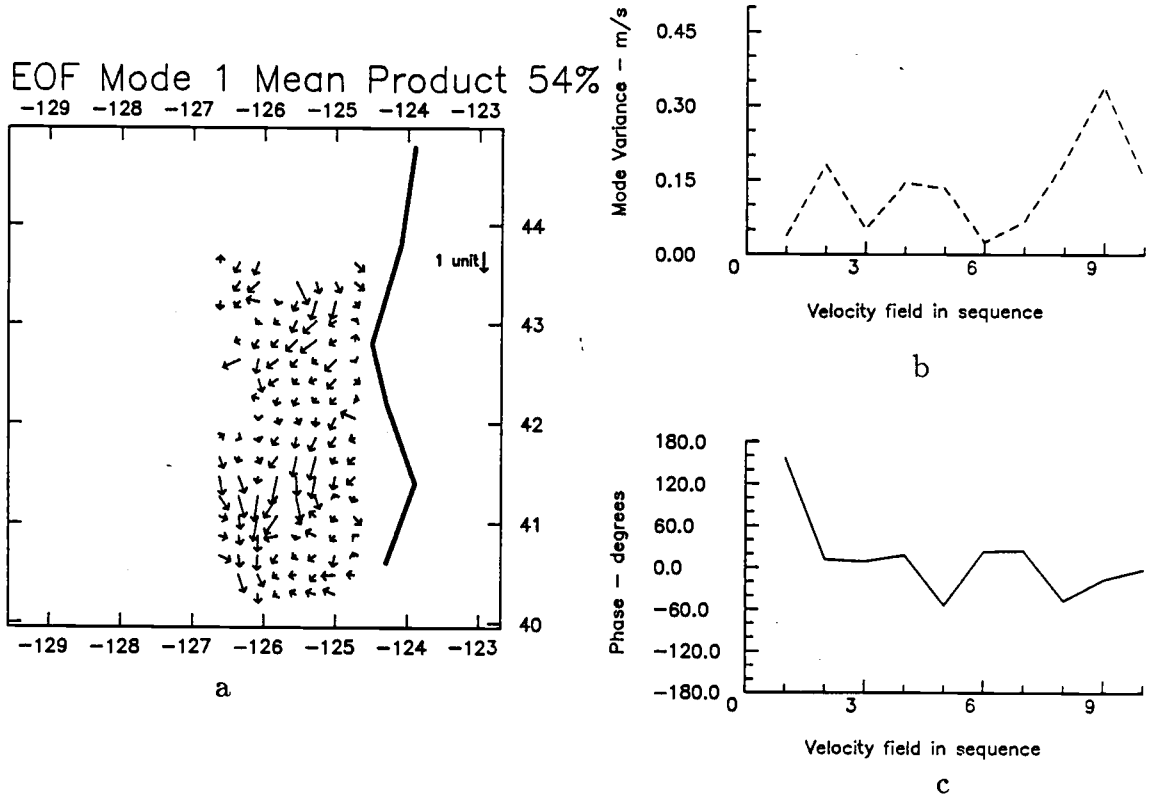

Figure 5.10 a) EOF 1 vector field decomposed from Jan. - Sept. 1987, and July 1988 MCC averaged velocity fields - mean product. EOF 1 explains 54% of the variance. b) associated amplitude time series c) associated phase time series. The horizontal axis corresponds to the position of the velocity field in the list given in Table 5.5.

above the cape and an area of convergent flow at the cape, which may represent the process of upwelled water being advected offshore by Ekman transport, followed by the surface water being subducted some distance offshore as it turns south. The rms value of the divergence is $1.3 \times 10^{-5} s^{1}$.

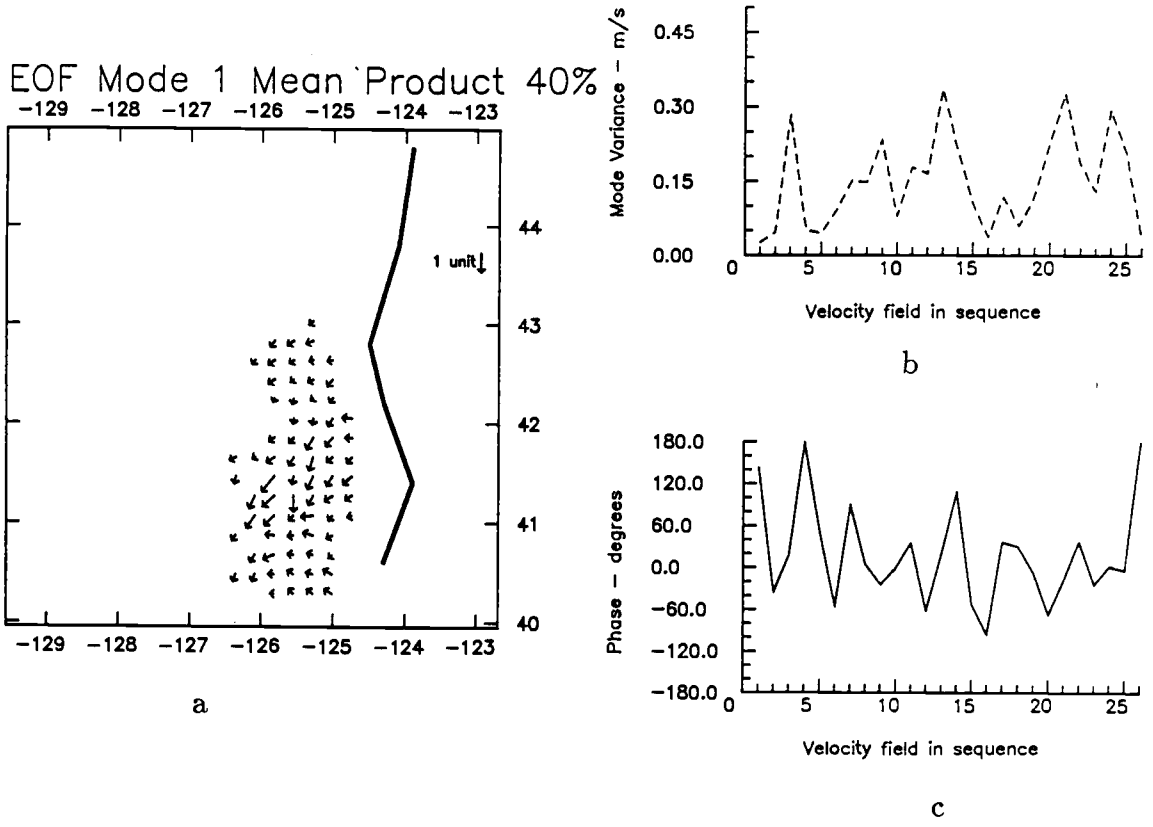

Figure 5.11 a) EOF 1 vector field decomposed from Jan. - Sept. 1987, and July 1988 MCC individual velocity fields - mean product. EOF 1 explains 40% of the variance. b) associated amplitude time series c) associated phase time series. The horizontal axis corresponds to the position of the velocity field in the list given in Table 5.5.

5.3 Summary

The above analysis provides several insights in attempting to create an understanding of the coastal ocean circulation field off Cape Blanco. Even if the MCC method is assumed to produce accurate pictures of the surface circulation fields, a major problem is that satellite imagery is difficult to obtain at the required time separation unless direct requests are made to the collection facility in advance. In

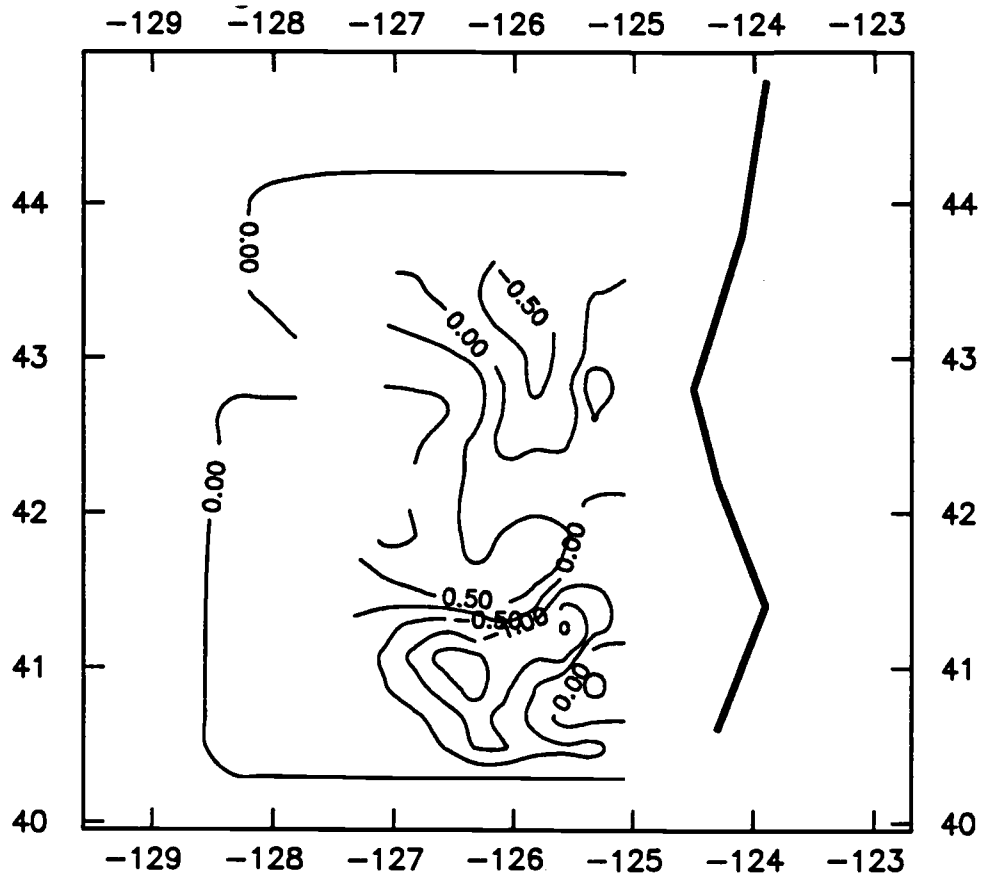

Figure 5.12 Divergence of first EOF - Jan-Sept sequence, units are $10^{-4}s^{-1}$.

the area off Northern California and Oregon, the presence of clouds much of the year further diminishes the number of useful images. The imagery available from the CZCS proves to be inadequate for the task attempted in this section. However, if future satellites provide visible wavelength imagery similar to the CZCS images and are collected on a daily basis, the tests performed in section four suggest that such imagery could be used with the MCC method in a useful manner in regions where strong features exist.

The sequence of five images from July 16-18 of 1988 illustrate the success of the MCC method under ideal conditions, consisting of 1) persistent strong winds, 2) clear skies and well-defined SST features, and 3) several image pairs with separations of less than 12 hours in a one to two day period. A complex EOF analysis of the mean product matrix provides the clearest picture of a strong southward jet moving offshore north of Cape Mendocino. Similar sequences occur at other times of the year. The most coherent results are obtained when each group of velocity fields from a short period (one to three days) is used to form an average field and these averages are used in a complex EOF calculation. The results show a southward meandering current, intensified in the offshore meander north of Capes Blanco and Mendocino.

6. Conclusions

The first goal of this thesis was to validate the MCC method by 1) finding RMS differences between MCC velocity fields derived from synthetic images and a model velocity field and between MCC velocity fields derived from real imagery and *in situ* data and 2) determining the maximum time separations between images of a pair in which the MCC method can produce a velocity field. The tests show that AVHRR imagery yields the best results when images are separated by as short a period as possible. RMS errors at six hour separation are on the order of 0.14 $m \cdot s^{-1}$, growing to 0.25 $m \cdot s^{-1}$ or more at separations of more than 18 hours. The CZCS images used in section four, separated by 24 hours, contained well-defined features that resulted in RMS differences less than the AVHRR images which were separated by 12 and 24 hours. The RMS difference is of the same order as when the two *in situ* fields are compared. It seems advantageous to apply averaging and the VCC procedure to eliminate incorrect vectors and determine a more correct displacement location.

The second goal of this thesis was to apply the MCC method to images of the coastal ocean off Cape Blanco, Oregon. The lack of strong features and the almost constant presence of cloud cover in the CZCS images did not allow the CZCS image set to be used to derive a coastal circulation pattern. The AVHRR image set resulted in two main conclusions. First, the mid-July sequence shows a strong jet that is clearly visible in the images from that time period. This sequence of images is an ideal sequence which has 1) a persistent wind associated with it;

2) strong, visible features, 3) images which are separated by less than 18 hours; and 4) several pairs that allow averaging or a complex EOF to be calculated. The procedure that was conducted to produce the well-defined flow seen in the first complex EOF was to remove the vectors with a maximum correlation coefficient less than 0.7 and then to apply the VCC. The second conclusion, is that the summer/spring view of the coastal circulation pattern off Cape Blanco, Oregon is of a meandering jet, flowing strongly offshore north of the cape with a weaker, onshore flow south of Cape Blanco.

The results of this thesis suggest that satellite imagery can be used under ideal conditions to produce reasonable circulation patterns of the coastal oceans using the MCC method. Incorporation of improvements mentioned in section 4.5 will give the method even more flexibility. It should be noted that AVHRR images should be collected consistently 12 hours or less apart. Operational procedures should be established for future color sensors to collect data every day, creating a data set that can be used for the purpose of determining ocean circulation patterns. Thus, the MCC technique is a method for examining spatially coherent velocity fields over areas larger than a ship can survey, if pairs of clear SST and color images are collected over as short a period as possible.

Bibliography

Abbott, M., West Coast Time Series Release Notes, unpublished manuscript,1988

Arnone, R. A., and P. E. La Violette, Satellite Definition of the bio-optical and thermal variation of coastal eddies associated with the African Current, *J. Geophys. Res.*, **91**, (C2), 2351-2364, 1986

Bendat, J. S., and A. G. Peirsol, **Random data, Analysis and measurement procedures**, John Wiley and Sons, NY, 566 pp., 1986

Clark, D. K., Phytoplankton algorithms for the Nimbus-7 CZCS, **Oceanography from Space**, J.F.R. Gower (ed.), Plenum, 227-238, 1981

Coakley, J.A. Jr., and F.P. Bretherton, Cloud cover from high-resolution scanner data detecting and allowing for partially filled fields of view, *J. Geophys. Res.*, **87**, (C7), 4917-4932, 1982

Collins, M. J., and W. J. Emery, A computational method for estimating sea ice motion in sequential Seasat synthetic aperture radar imagery by matched filtering, *J. Geophys. Res.*, **93**, (C8), 9241-9251, 1988

Davis, R. E., Predictability of sea surface Temperature and sea level pressure anomalies over the north Pacific Ocean, *J. Phys. Ocean.*, **6**, (3), 249-266, 1976

Davis, R. E., Drifter observations of coastal surface currents during CODE: The statistical and dynamical views, *J. Geophys. Res.*, **90**, 4756-477 2, 1985

Emery, W.J., A.C. Thomas, M.J. Collins, W.R. Crawford, and D.L. Mackas, An objective method for computing advective surface velocities from sequential infrared satellite images, *J. Geophys. Res.*, **91**, 12,865-12,878, 1986

Fily, M. and D. A. Rothrock, Extracting sea ice data from satellite imagery, *IEEE Transactions on Geoscience and Remote Sensing*, **GE-24**, (6), 1986

Fily, M. and D. A. Rothrock, Sea ice tracking by nested correlations, *IEEE Transactions on Geoscience and Remote Sensing*, **GE-25**, (5), 1987

Garcia, C. A. E. and I. S. Robinson, Sea surface velocities in shallow seas extracted from sequential Coastal Zone Color Scanner satellite data, *J. Geophys. Res.*, **94**, (12),681-12,691, 1989

Gordon, H. R., D. K. Clark, J. W. Brown, R. H. Evans, and W. W. Broenkow, Phytoplankton pigment concentrations in the middle Atlantic bight: Comparisons between ship determination and coastal zone color scanner estimates. *Appl. Optics*, **22**, 22-36, 1983

Hickey, B. M., Patterns and processes of circulation over the Washington continental shelf and slope, **Coastal Oceanography of Washington and Oregon**, ed. M. R. Landry and B. M. Hickey, Elsevier, N.Y., pp 607, 1989

Hickey, B., The California current system, hypotheses and fact, *Prog. Oceangr.*, **8**, 191-279, 1979

Huyer, A., Coastal upwelling in the California current system, *Prog. Oceangr.*, **12**, 121-279, 1983

Johnson, J. R., Analysis of Seasat-A satellite scatterometer wind observations with emphasis over the Antarctic circumpolar current., MS Thesis, Oregon State University, 1986

Kamachi, M., Advective surface velocities derived from sequential images for rotational flow field: limitations and applications of maximum cross correlation method with rotational registration, *J. Geophys. Res.*, in press, 1989

Kelly, K., The influence of winds and topography on the sea surface temperature patterns over the northern California slope, *J. Geophys. Res.*, **90**, (11),783-11,798, 1985

Kelly, K., An inverse model for near-surface velocity from infrared images, *J. Phys. Ocean.*, **19**, 1845-1864, 1989

Kidwell, K. B., NOAA Polar Orbiter Data (Tiros-N, NOAA-6, NOAA-7, NOAA-8, NOAA-9, and NOAA-10) User's Guide, Dec. 1986

Killworth, P. D., Coastal upwelling and Kelvin waves with small longshore topography, *J. Phys. Ocean.*, **8**, 188-205, 1978

Kundu, P. K., Ekman veering observed near the ocean bottom, *J. Phys. Ocean.*, **6**, 238-242, 1976

Lagerloef, G. S. E., and R. L. Bernstein, Empirical orthogonal function analysis of advanced very high resolution radiometer surface temperature patterns in Santa Barbara Channel, *J. Geophys. Res.*, **93**,6863-6873, 1988

La Violette, P. E., The advection of the mesoscale thermal features in the Alboran Sea gyre, *J. Phys. Ocean.*, **14**, (3), 1984

Leese, J.A., C.S. Novak, and B.B. Clarke, An automated technique for obtaining cloud motion from geosynchronous satellite data using cross-correlation, *J. Appl. Meter.*, **10**, 110-132, 1971

McClain, E. P. , Multiple atmospheric-window techniques for satellite-derived sea surface temperatures, **Oceanography from Space**, J.F.R. Gower (ed.), Plenum, 78-85, 1981

Mesinger, F. and A. Arakawa, **Numerical Methods Used in Atmospheric Models Vol. 1**, Garp (Global Atmospheric Research Programme) Publications Series No. 17, pp. 66, 1976

Mostafavi, H., and F.W. Smith, Image correlation with geometric distortion, Part 1: acquisition performance, *IEEE Trans. Aero. and Elect. Systems*, **AES-14**, (3), 487-493, 1978

Olivera, M, W.E. Gilbert, J. Fleishbein, A. Huyer, and R. Schramm, Hydrographic data from the first Coastal Ocean Dynamics experiment: *R/V Wecoma, Leg 7, 1-14 July 1981, CODE Tech. Rep. 7, Data Rep. 95, Ref. 82-8*, 163 pp., School of Oceanography, Oregon State Univ., Corvallis, 1982

Press, W.H., B.P. Flannery, S.A. Teukolsky, and W.T. Vetterling, **Numerical Recipes**, Cambridge University Press, N.Y. , 818 pp., 1986

Robinson, A.R., and L.J. Walstad, The Harvard open ocean model: calibration and applications to dynamical process, forecasting, and data assimilation studies, *Applied Numerical Mathematics*, **3**, 89-131, 1987

Strub, P.T., C. James, A. Thomas, and M. Abbott, Seasonal and non-seasonal variability of satellite-derived surface pigment concentration in the California Current, *J. Geophys. Res. in press*, 1990

Svejkovsky, S., Sea surface flow estimation from Advanced Very High Resolution Radiometer and Coastal Zone Color Scanner Satellite Imagery: A verification study, *J. Geophys. Res.*, **93**, (C6), 6735-6743, 1988

Vastano, A. C., and R. Bernstein, Mesoscale features along the first Oyashio Intrusion, *J. Geophys. Res.*, **89**, 587-596, 1984

Vastano, A. C. and S. Borders, Sea surface motion over an anticyclonic eddy on the Oyashio Front, *Remote Sensing Environment*, **16**, 87-90, 1984

Vastano, A. C., and R. Reid, Sea surface topography estimation with infrared satellite imagery, *J. Atmos. Technol.*, **2**, 393-400, 1985

Vesecky, J.F., R. Samadani, J.M. Daida, M.P. Smith, and R.N. Bracewell, Observing rotation and deformation of sea ice with synthetic aperture radar, *Proceedings of the International Geoscience and Remote Sensing, Sensing Symposium*, 1137-1145,1987

Wahl, D. D., and J.J. Simpson, Physical processes affecting the objective determination of near-surface velocity from satellite data, *J. Geophys. Res. in press*, 1989

Appendices

Appendix A: AVHRR Data

Below is a summary of the images reviewed for examining the annual description of the sea surface circulation off the coast of Cape Blanco. A total number of 147 images from November of 1986 to September of 1988 were reviewed. Figure A.1 shows the distribution of the images over the two years. Figure A.2 is the distribution of the images actually used to describe the coastal circulation. An image qualified for inclusion in the review if it was fairly cloud free near the coast and another usable image existed within 24 hours. Tables A1 and A2 list the AVHRR images used for the annual coastal circulation description (section 5).

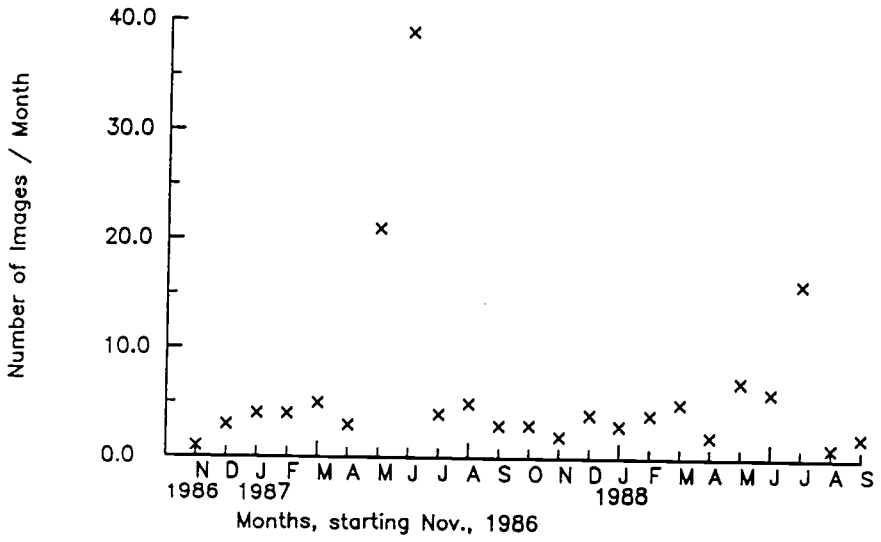

Figure A.1 Months versus the total number of AVHRR images in that month

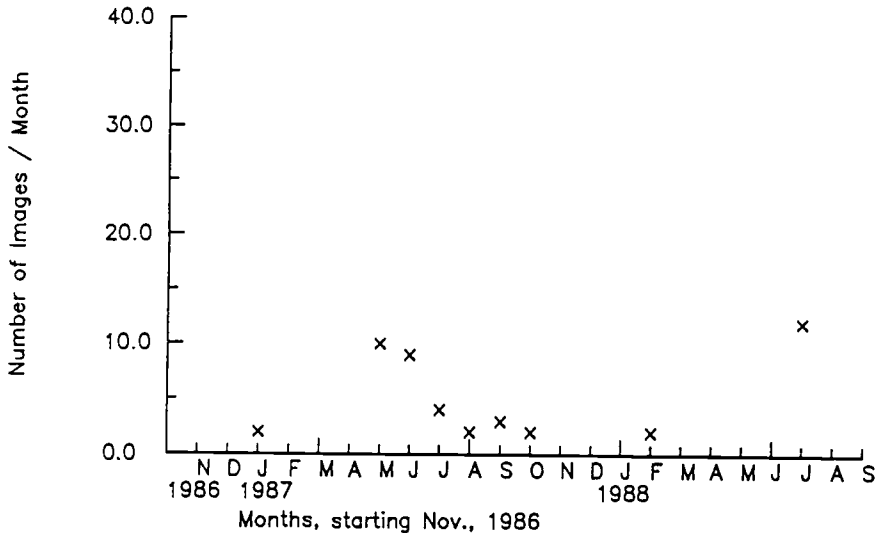

Figure A.2 Months versus the number of AVHRR images which where clear of clouds

TABLE A.1 - AVHRR Cape Blanco Images - 1987

Image	NOAA No.	Date	Time	x lim.	y lim.
AR5703	09	19Jan87	22:43	001-362	145-512
AR5704	09	20Jan87	22:36	001-362	001-512
AR5909	09	05May87	22:13	001-362	001-512
AR6274	10	06May87	14:44	001-362	001-512
AR5910	09	06May87	22:02	039-362	001-512
AR6274	09	07May87	12:11	001-253	001-512
AR5922	09	18May87	13:23	271-362	265-512
AR6408	10	19May87	03:40	253-362	295-512
AR5923	09	19May87	23:03	271-362	265-512
AR6412	10	20May87	03:18	301-362	224-512
AR6414	09	20May87	11:31	302-362	296-512
AR5924	09	20May87	22:53	244-362	301-512
AR6426	10	01Jun87	03:58	298-362	312-512
AR6429	10	01Jun87	16:22	282-362	254-512
AR5936	09	01Jun87	22:23	186-362	194-512
AR5937	10	02Jun87	03:37	141-362	186-512
AR5959	09	02Jun87	12:33	075-362	184-512
AR5938	10	02Jun87	15:58	107-362	001-394
AR5991	10	17Jun87	03:11	209-362	255-411
AR5993	10	17Jun87	17:13	209-362	255-411
AR5998	09	18Jun87	22:41	217-362	076-512
AR6111	09	14Jul87	23:03	001-362	001-512
AR6114	09	15Jul87	22:52	249-362	214-512
AR6165	09	31Jul87	12:00	272-380	315-512
AR6166	09	31Jul87	23:21	272-380	315-512
AR6202	09	30Aug87	22:59	102-362	001-512
AR6203	09	31Aug87	22:48	001-362	001-512
AR6238	09	26Sep87	23:09	206-371	231-512
AR6239	09	27Sep87	22:58	165-362	001-512
AR6241	09	28Sep87	22:47	001-362	001-512
AR6280	09	18Oct87	22:33	170-362	198-512
AR6285	09	19Oct87	22:23	222-370	001-123

TABLE A.2 - AVHRR Cape Blanco Images - 1988

Image	NOAA No.	Date	Time	x lim.	y lim.
AR6402	09	04Feb88	23:11	249-370	212-512
AR6403	09	05Feb88	23:00	249-370	212-512
AR6665	10	06Jul88	16:05	259-362	176-512
AR6666	09	06Jul88	23:49	217-362	144-512
AR6667	10	07Jul88	03:23	205-362	149-512
AR6676	10	09Jul88	16:41	188-362	240-512
AR6678	09	09Jul88	23:17	226-370	348-512
AR6703	10	16Jul88	15:48	099-362	154-512
AR6705	09	16Jul88	23:42	001-362	001-512
AR6706	10	17Jul88	03:00	001-362	188-512
AR6708	09	17Jul88	12:09	001-362	198-512
AR6711	10	18Jul88	16:45	001-362	001-512
AR6713	09	18Jul88	23:20	001-362	001-512
AR6715	10	19Jul88	16:22	001-362	001-512

Appendix B: Complex Correlations

A field of vectors can be correlated by finding the correlation of the two fields in complex space. The complex correlation determines the similarity of the two fields by computing a coefficient from zero to one and an average angle between the two fields.

A vector can be written in terms of a complex number as $w(x) = u(x) + iv(x)$, where x is the spatial location. The cross-covariance of the two fields can be written as

$$r =< w_1^* \cdot w_2 >= [\overline{(u_1 u_2 + v_1 v_2)} + i\overline{(v_2 u_1 - v_1 u_2)}], \qquad (B1)$$

where $< \cdot >$ is the inner product and an overbar is the average.

The correlation is the normalized covariance, equation B2.

$$\rho = \frac{r}{\overline{(u_1^2 + v_1^2)}^{1/2}\overline{(u_2^2 + v_2^2)}^{1/2}} \qquad (B2)$$

In vector format, equation B2 is:

$$\rho = \frac{< w_1^* \cdot w_2 >}{< w_1^* \cdot w_1 >^{1/2} < w_2^* \cdot w_2 >^{1/2}}, \qquad (B3)$$

where * refers to the vector conjugate. The average angle between the two fields is

$$\Theta = tan^{-1}\frac{\overline{(v_2 u_1 - v_1 u_2)}}{\overline{(u_1 u_2 + v_1 v_2)}} \qquad (B4)$$

and the magnitude, ρ_v (referred to the field correlation value in the text), is defined as

$$\rho_v = (\rho\rho^*)^{1/2} \qquad (B5)$$

The level of significance was found by first determining approximately what a decorrelation value would be for a specific field. Using the vector field produced from the dynamic heights from CODE, the field was autocorrelated for lags in all directions. The decorrelation value was chosen as the first point away from the zero lag which fell below 0.2. For the y direction, the point corresponded to approximately 60 km and for the x direction, the decorrelation point corresponded to 40 km.

The decorrelation value was then used to subsample the dynamic height vector field to create a random field of vectors. This field was then randomized in space and correlated with another randomized field. Figure B1 shows the 95% significant values for vector fields with increasing larger number of vectors. The curve was used in the main text to determine if a field correlation coefficient calculated was significant.

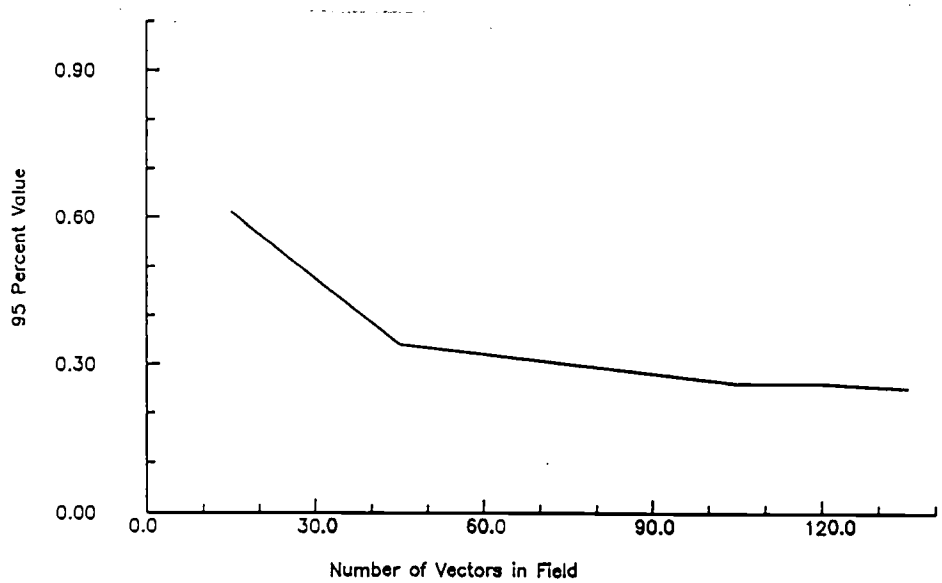

Figure B.1 Number of random vectors in a field vs. their 95 percent correlation coefficient

Appendix C: QG Model Description

The quasi-geostrophic (QG) model is defined by the shallow water equations C1-5.

$$\frac{\partial u}{\partial t} + u\frac{\partial u}{\partial x} + v\frac{\partial u}{\partial y} - fv = \frac{-1}{\rho_\circ}\frac{\partial P}{\partial x} \tag{C1}$$

$$\frac{\partial v}{\partial t} + u\frac{\partial v}{\partial x} + v\frac{\partial v}{\partial y} + fu = \frac{-1}{\rho_\circ}\frac{\partial P}{\partial y} \tag{C2}$$

$$\frac{\partial P}{\partial z} = -\rho g \tag{C3}$$

$$\frac{\partial u}{\partial x} + \frac{\partial v}{\partial y} + \frac{\partial w}{\partial z} = 0 \tag{C4}$$

$$\frac{\partial \rho}{\partial t} + u\frac{\partial \rho}{\partial x} + v\frac{\partial \rho}{\partial y} + w\frac{\partial \rho}{\partial z} = Forcing \tag{C5}$$

The non-dimensional shallow water equations on a beta plane with no forcing are shown in equations C6-10. Nondimensionalizing the equations with the following (*Robinson and Walstad*, 1987):

$$x = Dx', y = Dy', z = Hz', t = t_\circ t'$$

$$u = Uu', v = Uv', w = U(H/D)w'$$

$$\rho = \rho_\circ\left(1 + S(z) - \frac{f_\circ UD}{Hg}\delta(x,y,z,t)\right) \text{ where } S(z) = \rho_\circ^{-1}(\tilde{\rho}(z) - \rho_\circ)$$

$$P = -\rho_\circ g\int_0^Z (1+S)dz + \rho_\circ f_\circ UDp'$$

and given the non-dimensional parameters:

$$\alpha = \frac{Ut_\circ}{D}, \beta = \beta_\circ Dt_\circ$$

$$\Gamma_2 = \frac{f_\circ^2 D^2}{N_\circ^2 H^2}, \varepsilon = \frac{1}{f_\circ t_\circ}$$

$$\sigma = \frac{N_\circ^2}{N^2}, \text{ where } N^2 \approx \frac{g}{H}\frac{\partial S}{\partial z}$$

$$f = f_\circ + \beta_\circ y$$

results in the model equations.

$$\varepsilon\left(\frac{\partial u}{\partial t} + \alpha\left(u\frac{\partial u}{\partial x} + v\frac{\partial u}{\partial y} + w\frac{\partial u}{\partial z}\right)\right) - (1+\varepsilon\beta y)v + \frac{\partial p}{\partial x} = 0 \qquad (C6)$$

$$\varepsilon\left(\frac{\partial v}{\partial t} + \alpha\left(u\frac{\partial v}{\partial x} + v\frac{\partial v}{\partial y} + w\frac{\partial v}{\partial z}\right)\right) + (1+\varepsilon\beta y)u + \frac{\partial p}{\partial y} = 0 \qquad (C7)$$

$$\delta - \frac{\partial p}{\partial z} = 0 \qquad (C8)$$

$$\frac{\partial u}{\partial x} + \frac{\partial v}{\partial y} + \frac{\partial w}{\partial z} = 0 \qquad (C9)$$

$$\varepsilon\left(\frac{\partial \delta}{\partial t} + \alpha\left(u\frac{\partial \delta}{\partial x} + v\frac{\partial \delta}{\partial y} + w\frac{\partial \delta}{\partial z}\right)\right) + \frac{w}{\Gamma^2\sigma} = 0 \qquad (C10)$$

The model was implemented using a finite element scheme in the horizontal and a finite difference scheme in the vertical. The spatial grid was 3 kilometers.

Appendix D: Empirical Orthogonal Functions

Empirical orthogonal functions (EOF) have been used in oceanography and meteorology to decompose a time series' variance. EOFs partition a time series' mean square value into a spatial pattern and an amplitude time series for several modes. The number of modes can be no larger than the smaller of the number of grid points or the number of time points. The spatial patterns can be interpreted as uncorrelated fields of information. Each mode explains a fraction of the series' mean square value. When summed over all the modes, the total variance is reproduced. The highest mode (mode number 1) explains the greatest amount of a series' variance.

Complex EOF's are computed for vector time series. Each variable in a vector time series can be defined as $x(m,t) = u(m,t) + iv(m,t)$, where m is the spatial location of the vector and t, the time value. $x(m,t)$ can be decomposed by an orthonormal expansion shown in equation D1.

$$x(m,t) = \sum_{k=1}^{N} a(k,t)F(k,m) \qquad (D1),$$

where k is the mode number, a is the amplitude time series and F represents the spatial pattern. Both a and F are complex.

To compute the EOFs, the inner product matrix, $C = X \cdot X^*$ is formed. The eigenvalues,λ(k), and eigenvectors, F(k,m) are computed for the matrix C. The values are the solution to $\lambda(k)F(k,m) = F(k,m)C$. The amplitudes are obtained by $a(k,t) = \sum_{m=1}^{M} x(m,t)F^*(k,m)$ where * denotes the transpose of the matrix.

It is convenient to display the amplitude time series in its polar coordinates, A, the magnitude, and Θ, the phase of the series, such that $a(k,t) = A(k,t)e^{i\Theta(k,t)}$. The magnitude states how the length of the spatial pattern vectors change with time and the phase states how the spatial pattern vectors rotate with time.

Appendix E: Acronyms

ADCP	Acoustic Doppler Current Profiler
ATS	Applications Technology Satellite
AVHRR	Advanced Very High Resolution Radiometer
CFL	Curant-Fredrichs-Lewy
CODE	Coastal Ocean Dynamics Experiment
CTD	Conductivity, Temperature and Density
CTZ	Coastal Transition Zone
CZCS	Coastal Zone Color Scanner
EOF	Empirical Orthogonal Function
FFT	Fast Fourier Transform
MCC	Maximum Cross-Correlation
MCSST	Multi-Channel Sea Surface Temperature
NOAA	National Oceanic and Atmospheric Administration
OPUS	Organization of Persistent Upwelling Structures
QG	Quasigeostrophic
RMS	Root Mean Square
SST	Sea Surface Temperature
VCC	Vector Consistency Check
VHRR	Very High Resolution Radiometer